Microfluidic Analysis of Vertebrate Red Blood Cell Characteristics

by

Kathryn Diane Fink

A dissertation submitted in partial satisfaction of the
requirements for the degree of

Joint Doctor of Philosophy
with University of California, San Francisco

in

Bioengineering

in the Graduate Division

of the

University of California, Berkeley

Committee in charge:

Professor Dorian Liepmann, Chair
Professor Luke P. Lee
Professor Joe DeRisi
Professor Susan Muller

Fall 2016

Abstract

Microfluidic Analysis of Vertebrate Red Blood Cell Characteristics

by

Kathryn Diane Fink

Joint Doctor of Philosophy in Bioengineering

University of California, Berkeley and University of California, San Francisco

Professor Dorian Liepmann, Chair

Continuous multidisciplinary advancements in medicine, science and engineering have led to the rise of biomedical microfluidic devices for clinical diagnoses, laboratory research for modeling and screening of drugs or disease states, and implantable organs such as artificial kidneys. Blood is often the biological fluid of choice for these purposes. However, unique hemodynamic properties observed only in microscale channels complicate experimental repeatability and reliability.

For vessels with 10-300µm diameters, red blood cell properties such as deformability have a significant impact on hemorheology, and the blood can no longer be considered as a homogeneous fluid. The flowing blood segregates into a red blood cell rich core bounded by a cell-free layer composed almost entirely of plasma. Viscous forces dominate flow behavior, and shear rates at the wall are much higher than in arteries and veins. The overall viscosity becomes dependent on vessel diameter. These unique characteristics are interesting from a biophysics perspective, but the value of biomedical microfluidic technologies makes research in this regime even more critical. Accordingly, this work focuses on experimental comparison of the microfluidic flow properties of red blood cells with varying physical characteristics.

Blood viscosity in microscale tubes was investigated experimentally for 6 blood types (goat, sheep, pig, llama, chicken and turkey) at a range of hematocrits (0-50%). The selected blood types represented a small sample of the wide-ranging red blood cell characteristics found in mammals, birds, reptiles, amphibians and fish. These red blood cells vary in size over an order of magnitude, represent shapes ranging from biconcave to ellipsoidal, and include both nucleated cell types found in birds, amphibians and reptiles and denucleated mammalian cells. Pressure drop experiments at physiologically relevant flow rates were carried out for rigid tubing diameters ranging from 73µm - 161µm. The resulting viscosities were normalized relative to the measurements made of the homologous plasma for each species. The viscosity of blood in this regime is much different than in larger vessels (>500µm) or in small capillaries (<10µm), but existing studies in this size range focus only on human blood.

The results analyzed in the context of four primary variables: hematocrit, red blood cell size, red blood cell shape, and red blood cell deformability. The aggregation of the porcine blood complicated the data collection process, resulting in only a few usable data points.

Examination of the role of hematocrit yielded results which aligned well with existing

hemorheology research: viscosity increases with hematocrit. After applying an existing fitting equation the collected data, three primary trends were observed. First, the chicken blood had the highest viscosity at every hematocrit regardless of tubing diameter. Secondly, the viscosities of the goat and sheep blood were very similar at all hematocrits, and ultimately had the lowest viscosity of all samples at the highest measured hematocrit values. Finally, the turkey and llama blood generally had the lowest viscosity at low hematocrit, with a deflection point around 30% hematocrit where viscosity began to increase much more sharply.

The role of cell size was considered in the context of both mean cell volume and major cell axis relative to vessel diameter, to account for the elongated shape of the llama, chicken and turkey red blood cells. The results indicated that cell major axis is better correlated with viscosity than cell volume, suggesting the potential importance of cell shape. The red blood cells were then characterized as either oblate or prolate to further investigate the importance of shape. The results further supported the idea that overall blood viscosity in small vessels depends on both cell size and shape. However, as with the hematocrit analysis, the chicken blood was an outlier. The chicken red blood cells are quite similar to turkey red blood cells in both size and shape, yet the chicken blood was consistently far more viscous than turkey blood. A comparison with theoretical rigid particles suggested that the chicken red blood cells may be the least deformable of the sampled blood types.

Two additional experiments were performed to assess the potential importance of deformability. Additional pressure drop measurements with chemically-hardened red blood cells demonstrated that the measurement system is quite sensitive to changes in cell deformability. Flow visualization in a microfluidic contraction indicated that the high viscosity of the chicken blood relative to the turkey blood could be attributed to differences in deformability.

Blood viscosity is influenced by multiple cell characteristics, including size, shape and deformability. The role of these parameters is worthy of further investigation alongside ongoing research in the rheology of human blood. The impact of red blood cell deformability on viscosity in small vessels is particularly interesting. The described experimental apparatus is easily replicable and highly customizable, and may serve as a helpful tool to analyze blood parameters in biomedical microfluidic device research and development. The collected data sets are available to interested researchers, and can currently be obtained by direct request. Ultimately, an online database will be made available via the Liepmann lab website.

Dedicated to the one who:

Never complained about the late nights

Or early mornings

And never commented on the late mornings, either.

Who never judged me for a 2nd glass of wine

And patiently listened to the thirtieth quals rehearsal.

Who didn't count the years of school

Or the hours of work

Or the number of moves

Who endured my weekends away, for conferences or for fun

And who was always there with comfort and companionship

Absolutely every time I needed it most.

For your support and love that I could always rely on

Thank you

Table of Contents

Acknowledgments

I am deeply thankful to have had the opportunity to work with Dorian Liepmann. I cannot imagine how I would have made it to this point with any other mentor.

I was told by numerous sources that selecting a Ph.D. advisor is one of the most important choices you can make. A Ph.D. advisor is someone who, at best, can be a major part of your academic and professional world for the rest of your life. At worst, they will use you for their own gain, spend you because your own future means nothing to them, and throw you away when you have been wrung dry. My BEAST friends and I, the wiser for our years, have repeated this advice to entering first-years: choose wisely. Like those who first passed this information on to us, we have found that very few listen. Choosing to work with Dorian (or convincing him to work with me) was the best decision of my grad school career.

Thank you, Dorian, for always strongly supporting me as a researcher, a student, and as a person. Thank you for repeatedly demonstrating how your own brand of leadership – empathetic, kind, personable – triumphs over those who lead to get ahead. And, I have seen how well that technique works. I believe that if all faculty members throughout the world followed your lead, we would all be so much more advanced and so much better off. You are the leader that the academic community needs. There are no words to express the extent of my gratitude for your guidance. I look forward to many more years of consulting you for advice, be it skiing or microfluidics. I feel bad for all these poor saps joining the BioE program who do not work with you. Thank you.

Next, my eternal thanks to Dr. Jacobo Paredes: my very first lab coworker and, as I may once have said, "My" postdoc. Thank you for everything that you did for Dorian's lab, and for me. We miss you, but wish you the very best in your role as Professor. I hope that when you acquire lab equipment from a donation, you will help your students with packing up the moving truck (taking care to lift the lighter end of heavy equipment, as is your right as a professor), and that you will remain your always joyous, positive self throughout the extent of your career. And please, be careful with the fumes.

 To Karthik Prasad: "my" first undergrad – holy cow, you're awesome. When Dorian and I first met you as a freshman, we thought you were a grad student based on your level of insight. I fully expect to see the day when you are at the top of the top in whichever field you choose – politics, medicine, research, etc. Let me put it in official writing: if you ever need a recommendation letter, be it tomorrow or ten years from now, I am happy to provide such a letter.

To Marc Chooljian: I am so sorry that both Jacob and I left you prematurely. However, as having been the senior grad student in a small lab, I am wholly convinced that you will carry out that duty far more successfully than I did. Your dedication to BEAST, your interest in the scientific world, and your experience in bioengineering will serve you well as The Senior Grad Student and in all your future pursuits.

Thank you to my committee members: Susan Muller, Luke Lee and Joe DeRisi.

Susan: Thank you for your support over the years. I have greatly benefited from your guidance, and sincerely appreciate your feedback on this document. I also appreciate the help of your graduate students, Kari Storslett and Margaret Hwang.

Luke: You were the first to tell me how valuable a mentor Dorian can be, and as with so many other things, you were definitely right about that.

Joe: A special thank you for your guidance in the area of red blood cells. The experiments which I was able to carry out with Jenai Quan in your lab were instrumental in helping me understand the potential future of this research.

I also wish to express my gratitude to Paul Lum. Your management of the Biomolecular Nanotechnology Center and your support of BIOE 121L are invaluable. My research, as well as that of my colleagues, would not have been possible without you. You are someone whose own excellence translates to elevate the work of those around you.

I also would like to acknowledge the three funding sources which made my grad school career possible:

First, the Northern California Chapter of ARCS: I likely could not have joined Dorian's lab without your support. The ARCS meetings have exposed me to a realm of strong, powerful women who believe in the scientific future of this country. I am so grateful for their support, and hope one day to join the ranks of ARCS donors.

Next, thank you to the National Science Foundation. It has been an immense honor to be an NSF Graduate Research Fellow. The government support of academic research is crucial to the future of this country.

Finally, thank you to the Siebel Scholars Foundation. Although my research may not fit the typical bill for Siebel Scholars, I am so honored to belong to this esteemed group of individuals. I am unbelievably excited for the years to come, beginning with 2017's conference and continuing from there.

On a more local front, I wish to gratefully acknowledge the work of the bioengineering office, and particularly that of Kristin Olsen and Jennifer Teverbaugh. I realize that I have profoundly benefitted from the goodwill of being Dorian's student, and I hope that all staff members will accept my very deepest thanks.

Next up is family. My own family has always believed in me, even when it meant leaving school and moving to California. I appreciate their continuing emotional support of my progress. Every day I hope that I make them proud.

I also deeply appreciate the support of the Rose & French families, who presented a united front to celebrate my academic achievements. I have loved the cookie bouquets, the magazines, and most of all your willingness to uplift me in times of academic crisis.

I joined this program because of BEAST, and I felt comfortable staying here due to LesBEAST. The outreach of supremely talented individuals is what makes the UC Berkeley – UCSF Graduate Program in Bioengineering such a successful place. I especially appreciate Cohort 2010 for making me feel welcome in a new home, and for LesBEAST (Jo, Connnie & Paul) for all the great memories.

I sincerely hope that the core professors of this great department understand how incredible the students who join our program are. Without the outreach of BEAST, we would be another highly competitive wallflower of a program. BEAST is what makes the best of the best come here, to the Bay Area. These are the same students who will always reminisce, publicly and fondly, of the value of BEAST. That word of mouth is so critical to recruiting the top students, now and in the future. Please remember that as a solo researcher, any given professor is unlikely to succeed. The quality of your graduate students is closely related to the depth and breadth of BEAST.

I have lost many close role models during the course of this Ph.D. My maternal grandmother, Mary Stiles, was truly an inspiration for what women can accomplish in a world built to empower men. I believe that she would have been so proud of me; what I truly wish is that she could know how proud I am of her. Likewise, I extend deep gratitude and recognition for my grandmothers Dorothy Piper Fink and June Hamilton. There are also two non-humans who passed away during this thesis. Thank you, Stallion: the fluffy white cat who was my copilot as I drove west, 12 years ago, to start a new chapter of my life in California. I am also glad that I had the opportunity to meet Jackson, our lab mascot. The halls of Hearst Memorial Mining Building will always be a little quieter and a little less joyous without his presence.

The penultimate thanks is to Cisco & Perrin. The former has already had this dissertation dedicated to him, so what else does he need? For Perrin, I hope we are an adequate replacement for your former family, and that you will someday learn to meow in a less obnoxious way.

Finally, to Phil. You have borne this process nearly as much, or perhaps even more, than I have. Your support is the most valuable gift I have ever received. I cannot begin to express how fortunate I feel to come home to you every day. Thank you so much for your love and your belief. If it takes the rest of my life, I hope I can repay what you have done for me over the course of this degree.

Chapter 1
Introduction

1.1 Motivation

More than 200 million years ago, our mammalian ancestors emerged and evolved; the environmental demands of their time resulted in the denucleated, flexible red blood cells shown in countless science textbooks and TV show. Meanwhile, the egg-laying vertebrates such as birds, reptiles and amphibians, retain the nucleated, ovoid shapes of their past. These differences in our blood cells, even among mammalian species (Figure 1), have fascinated biologists for 200 years. Yet the study of how these varying characteristics affect blood flow has been quite limited compared to the scale of research on human blood flow. This dissertation project seeks to shed light on how these significant differences in cell size, shape, deformability and aggregation affect blood flow at the microscale. While this research is intrinsically interesting on a scientific level, the ramifications extend to the design of lab-on-a-chip diagnostic devices that use blood.

As BioMEMS techniques continue to develop, the breadth and depth of microfluidic research utilizing blood grows as well. Diagnoses which previously required skilled technicians and access to large, expensive lab equipment are being miniaturized for rapid testing at home, in medical clinics, and in isolated or less developed areas of the world. In addition, there is a new body of research in developing "organ-on-a-chip" devices as a separate research tool. Finally, mechanical replacements for failing organs are already a reality and becoming more complex and useful every year; these often require complicated microchannels to replicate filtration, oxygenation, and other similar biological functions. All of these research areas involve blood flow through channels 10s to 100s of microns in diameter. This is a size range in which blood develops unique and complex flow behaviors, which will be further addressed in Chapter 2. For many researchers developing these microfluidic devices, there are incentives to use animal blood rather than human blood in early or even late stages of device development and characterization. There are two primary ways in which animal blood is used instead of human blood: in the requisite animal testing phase of implantable device development, and as an *in vitro* substitute in benchtop device development and characterization. The successful extrapolation of these animal-based results to future application with human blood relies on an understanding of how the blood flow properties compare to human blood. These differences can affect flow rates, shear rates and cell damage. However, even a well-prepared researcher will find a dearth of information in this area, particularly for flow in microscale channels.

Even in the early 1900s, the substitution of animal blood data for human blood without accounting for their differences was an issue. Robin Fåhraeus touched on this in 1929 while comparing existing literature to his studies with human blood. At the time, it was accepted that, *in vivo*, white blood cells flow along the margins of the centralized red blood cell core; this was attributed to white blood cells having a lower specific gravity than red blood cells. Fåhraeus notes that "In the frog, generally used in such studies, the white cells do predominate in the peripheral zone but in mammals the opposite is the case as has been demonstrated by experiments with capillary tubes, as described above. The relative difference in the size of the white and red cells in frog and mammalian blood gives the key to the true explanation of the phenomenon. In the frog the huge red cells claim the axial, fast-moving zone and thrust the small white cells into the peripheral stream; in mammalian blood in which the factor of size is reversed the leucocytes predominate in the axial zone. Differences in specific gravity of the cells have no

1
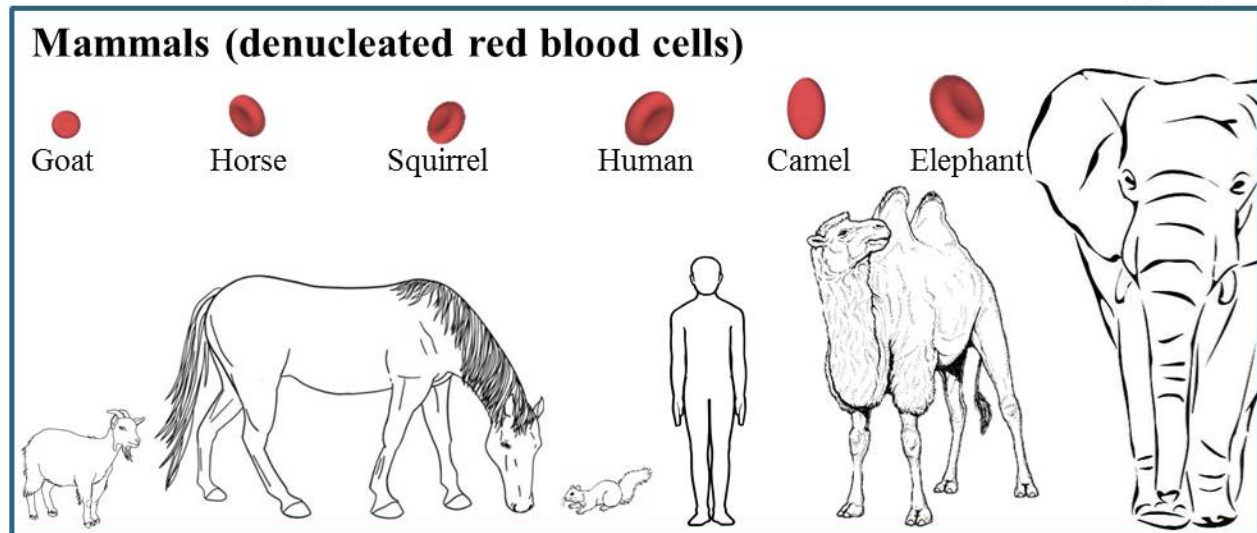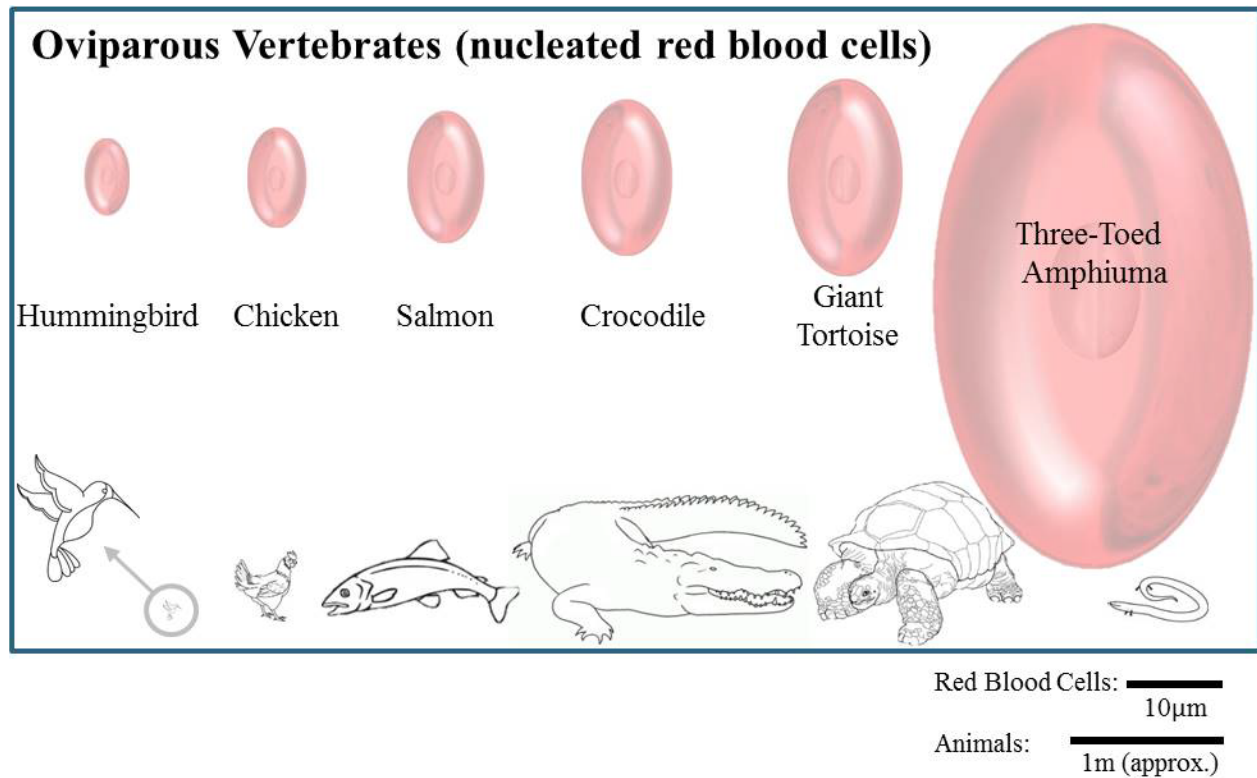
Figure 1. Comparison of red blood cell sizes for oviparous (top) and viviparous (bottom) vertebrates, scaled by cell size [1] and approximate body size.

influence upon their position in the stream." [2] At the time, this extrapolation of animal blood observations to human blood flow resulted in incorrect conclusions. Today, erroneous assumptions may result in costly redesigns, delay of experiments, or complete device failure. This experiment establishes a baseline of how cell characteristics will affect flow in these microdevices. All data will be made available online for analysis and comparison to future experiments in the field.

www.manaraa.com

1.2 Experiment

The complete experimental protocol is presented in Chapter 3. Briefly, whole blood was acquired from six vertebrate species – four mammals and two birds – and six suspensions of varying volume fraction (hematocrit) were prepared. Pressure drop was measured in tubes with diameters on the order of microfluidic device dimensions (10s to 100s of microns). A range of flow rates was selected based on both *in vivo* and *in vitro* parameters. The results were compared and analyzed in the context of cell size, shape and deformability.

1.3 Characteristics of Blood

Vertebrate blood is composed of three major elements: blood cells, suspended particles and the aqueous solution known as plasma. Red blood cells, or erythrocytes, comprise about 98% of the total circulating cells. The other 2% consist of white blood cells (leukocytes) and platelets (thrombocytes). Overall, the cells occupy 25-45% of the total volume of blood, depending on the species. In humans the typical volume fraction of red blood cells, or hematocrit, is around 45%. The large percentage of whole blood occupied by erythrocytes means that their presence and characteristics have a significant impact on the overall behavior of blood in the circulatory system. The second component of blood is chylomicrons. These are nanoscale lipoprotein droplets which facilitate lipid transport throughout the body, and are present in such low amounts that their presence can be considered negligible in hemorheological studies [3]. Finally, blood plasma is water (90-92% v/v) containing dissolved proteins (7% v/v) and inorganic compounds (~1% v/v) such as electrolytes. Plasma behaves as a Newtonian fluid for the experimental parameters in the present study.

Vertebrate blood cell characteristics vary significantly, sometimes even among individuals of a single species [4] or for an individual at different stages of development [5]. As a matter of interest, a general background of mammalian, avian, reptilian and amphibian red blood cells is provided in the subsequent sections. Overall, mammals have the smallest erythrocytes; cell sizes increase in birds and then reptiles, with amphibians and fish generally having the largest erythrocytes. More extensive literature on the subject is available elsewhere [4, 6].

1.3.1 Mammalian red blood cells

Human red blood cells are denucleated biconcave discocytes (Figure 2). They are composed of 65% m/m water, 32% m/m hemoglobin, and some inorganic components such as potassium and sodium [3]. The presence of hemoglobin increases the internal viscosity of the red blood cell to ~6 cP, approximately 5-6 times larger than plasma and water. The membrane contains a phospholipid bilayer and an elastic spectrin network that enables "shape memory" – the membrane elements will return to the same position on the relaxed erythrocyte (rim, biconcave center, etc.) following a shape deformation [7]. The biconcave shape is primarily a result of the expulsion of the nucleus during erythropoiesis [8]; because of this, the erythrocyte is quite deformable and able to maintain a constant
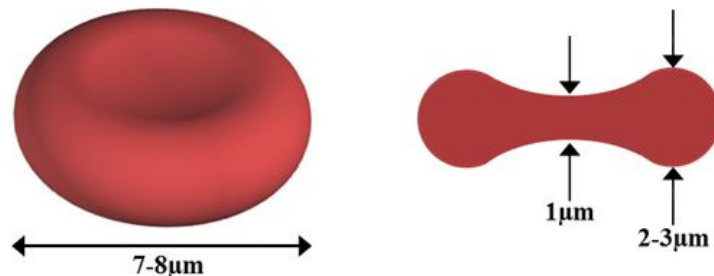
Figure 2. Dimensions of typical human erythrocyte. Left: major diameter. Right: Thickness of cell cross-section

3

volume and surface area when changing shape [9].

In popular science, the biconcave shape of the human erythrocyte is often described as ideal for flow in vessels ranging from a few microns to centimeters in diameter [10] and optimized for maximum oxygen exchange [11]. However, vertebrate red blood cell sizes span a full order of magnitude and vary in shape and deformability, so there is clearly not just one "correct" optimized set of red blood cell characteristics.

1.3.2 Exceptions to typical morphology of mammalian red blood cells

Some Artiodactyls (even-toed ungulates such as hippopotamuses, camels, and pigs) have erythrocytes which do not conform to typical mammalian red blood cell characteristics, raising the possibility of a separate branch of erythrocyte evolution [12]. Family Cervidae (deer and elk) have distinctly shaped, differentiated erythrocytes spanning a range from tapering and spindle-shaped to irregularly polygonal, in some cases resembling the crescent shapes referred to as sickle cells when present in humans [13, 14]. Family

Figure 3. Optical micrograph of llama erythrocytes in homologous plasma and PBS

Tragulidae (mouse deer) have small, nearly spherical erythrocytes [12]. Family Camelidae, representing camels, llamas and alpacas, have small, highly ellipsoidal red blood cells [14] as shown in Figure 3.

This unique shape (Figure 4a) has been considered an adaptation conducive to prolonged dehydration and rapid rehydration. When dehydrated, the camel red blood cells shrink but retain a regular shape. The cells have been observed to withstand 20% saline solutions (roughly five times as salty as the sea) (Figure 4b), whereas human cells become completely crenated in 1.5% saline. The cells become large and spherical after sudden and drastic rehydration (Figure 4c), but little to no hemolysis occurs even after consuming large amounts of water (50 liters in 1 minute). [15]
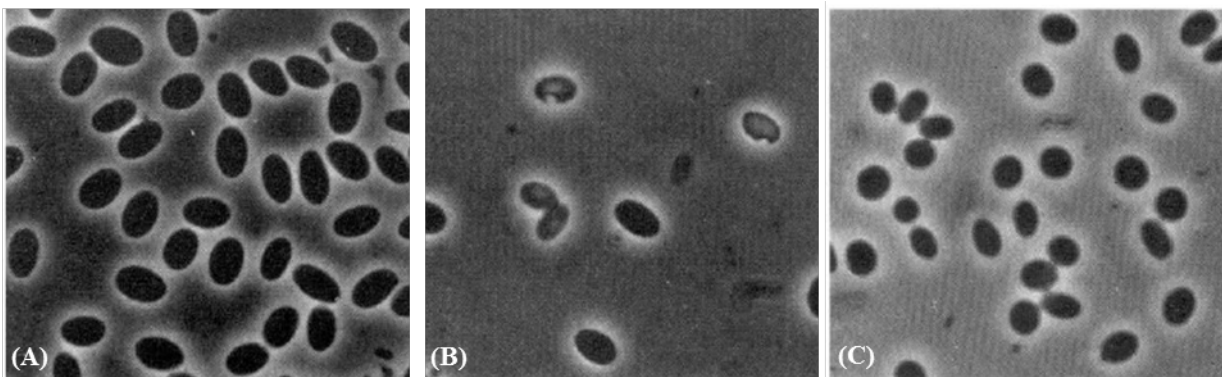
Figure 4. From [15]. (A) Normal camel red blood cells (B) Camel red blood cells in 20% saline, with both normal cells and slightly crenelated cells (C) Camel red blood cells 4 hours after rehydration. All images x434 magnification

In addition, there are blood cell irregularities which can be common among species which otherwise have biconcave discocytes. Some of these changes are a reflection of illness, exposure to toxins, or the effects of treatment and storage of whole blood post-venipuncture. However, others are considered pathologically normal deviations found in healthy animals. For example, echinocytes (Figure 5a), which are red blood cells covered with uniformly spaced and sized

4

spicules, are common in pigs. Abnormally shaped erythrocytes without a specific descriptive term are considered poikilocytes, and can be present in healthy goats (Figure 5b). [14]
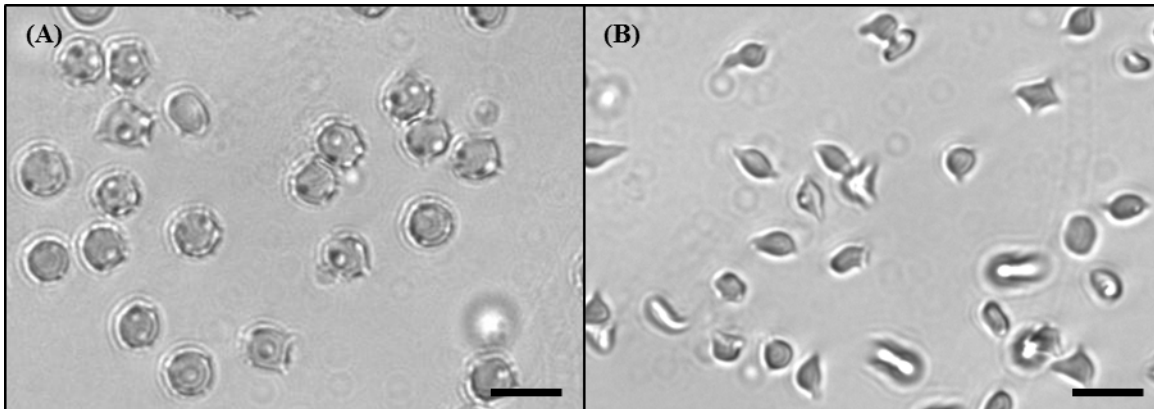
Figure 5. (A) Echinocytes in donor blood from a healthy pig and (B) young goat at 40x magnification. Error bars are 10μm.

1.3.3 Oviparous vertebrate red blood cells

The erythrocytes of egg-laying (oviparous) vertebrates have a distinct morphology. First, all such red blood cells are nucleated. They are also ovoid, with a major axis diameter larger than that of the largest mammalian red blood cells [6]. The erythrocyte membrane generally has a much higher shear modulus than mammalian red blood cells due to the presence of additional cytoskeletal elements [8]. Birds have the smallest red blood cell sizes, and fish and amphibians the largest – the former can have cell volumes 100 times larger than mammalian red blood cells [4]. The largest observed red blood cell diameters are found in amphibians.

Bird red blood cells are generally 2-3 times larger than mammalian cells, with mean cell volume of 105 to 286fl, in comparison to an average mammalian mean cell volume 62.1fl [6]. Major components of the red blood cell membrane are similar to those in mammals, but with two additional cytoskeletal elements: the marginal band, and the transmarginal band material. The former of these is a collection of microtubules attached to the membrane, and is responsible both for the ellipsoidal shape of the avian red blood cell as well as differences in how the red blood cell is able to deform. [16] The transmarginal band is believed to help maintain the position of the nucleus within the cell and also contribute to the formation of the ellipsoidal shape. Despite the presence of the nucleus, the mean cellular hemoglobin concentration in birds is similar to that of mammals, suggesting that hemoglobin may also be present within the nucleus itself [17].

Reptile red blood cells are nucleated, oblate ellipsoids with a biconvex rather than biconcave shape. Erythrocyte size and length/width (L/W) ratio can vary drastically across families and even within families of reptiles [18]. Snakes and lizards generally have the smallest erythrocytes, and turtles and crocodiles have the largest among reptiles [18]. The average major axis of lizard erythrocytes is 12.43-16.85μm with a 1.56 to 1.99 L/W ratio [18]. A comprehensive study of turtle species determined a median erythrocyte length of 21.9μm and width of 13.7μm; within this study, aquatic freshwater turtles had the largest erythrocytes and land turtles the smallest. As with other vertebrates, erythrocyte size and overall erythrocyte count are inversely proportional [19].

Amphibians have larger red blood cells than reptiles, birds and mammals [18]. The three-toed amphiuma – a 1 meter long short-legged aquatic salamander from the southeastern United

5

States (Figure 6) – has the largest known red blood cells of vertebrate species: 70μm long and 40μm wide [18]. It has been noted that larger salamanders tend to have larger blood cells [20], and more active salamanders typically have smaller red blood cells than their less active counterparts [21]. The relative size of the nucleus also varies across amphibian families, with the largest nuclei (0.22-0.34 nucleocytoplasmic ratio) in urodeles (salamanders) and the smallest (0.10-0.16 nucleocytoplasmic ratio) in anurans (frogs and toads) [18]. As with reptiles, aquatic amphibians tend to have larger red blood cells than terrestrial amphibians [18].
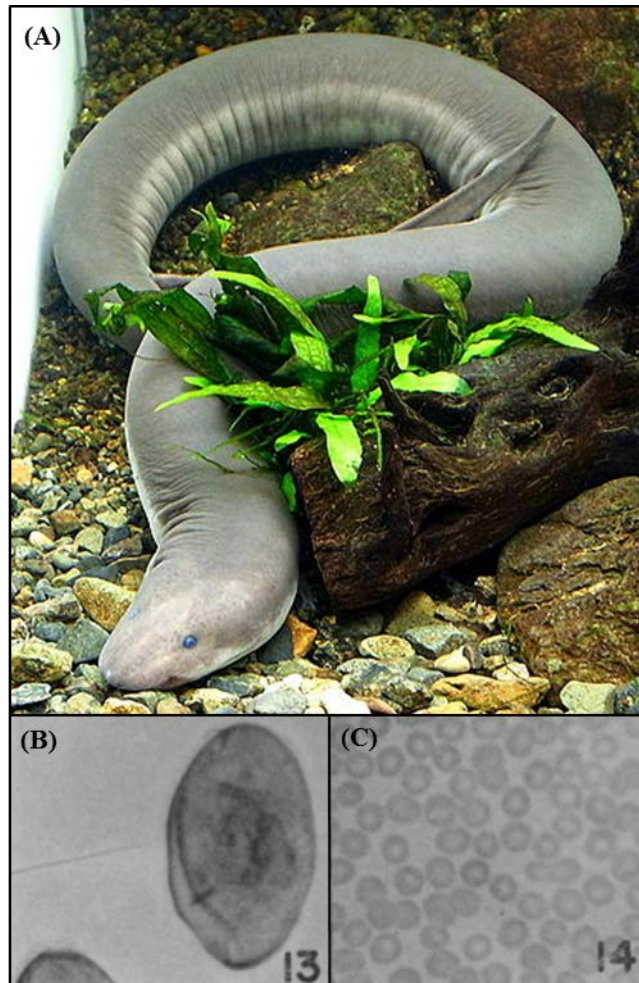
Figure 6. (A) Three-toed amphiuma (*Amphiuma tridactylum*) – a salamander from the southeastern United States with the largest recorded red blood cells among vertebrate species. Image available by creative commons license: https://en.wikipedia.org/wiki/Amphiuma_tridactylum#/media/File:Amphiuma_tridactylum.jpg (B) From [22] Amphiuma blood smear x695 and (C) from [22] human blood smear x695

1.3.4 Evolution of red blood cells

The origin of red blood cells in vertebrates can be traced to the rise of oxygen-circulating fluids, the first of which accomplished this task with an iron-containing protein known as hemoglobin [23]. Red blood cells followed shortly thereafter as a means to package and carry hemoglobin. Experimentally, red blood cells have been shown to require less pressure for passage through small blood vessels compared to hemoglobin solutions [24]. Hemoglobin-

6

carrying red blood cells have been found in multiple Animal phyla, and it is possible that they arose several different times within differing branches [23].

The largest distinction between mammalian red blood cells and those of other vertebrates is the absence of a nucleus. This has been attributed to differences in atmospheric conditions during geologic periods. Mammals emerged in the Triassic period of the Mesozoic era as the atmospheric oxygen content was in decline, with only about half the oxygen compared to present day. Expulsion of the erythrocyte nucleus was likely an adaptation to increase oxygen exchange in the capillaries via the greater exposed surface area of a biconcave cell, enabling the rise of highly active, warm-blooded mammals. Birds, which developed from d, emerged in the Jurassic period, when atmospheric oxygen content was returning to present day levels. Although they too were warm-blooded and active, with strong circulatory systems, the higher oxygen content meant there was no evolutionary need to expel erythrocyte nuclei. [25]

There are several hypotheses about why the size of vertebrate erythrocytes spans such a large range. This field of research is ongoing, and it is likely that erythrocyte size is based on many factors ranging from evolutionary factors to habitat. A few of the primary hypotheses are described here. Often the first question that comes to mind when considering the range of erythrocyte sizes is to what extent capillary size also varies. Some studies suggest a correlation between capillary size and red blood cell size across amphibian, reptilian and mammalian species [17], where red blood cells were generally ~25% larger than the smallest capillaries. However, across all vertebrate species the range of capillary diameters (3 - 20μm) is significantly smaller than the range of cell sizes (3.3μm - 70μm), and the majority of vertebrates have capillaries less than 5μm in diameter [4]. There is no correlation between animal body size and erythrocyte size, as illustrated by examples in Figure 1 [4]. Researchers identified a strong positive correlation between erythrocyte size and genome size among mammals, although the statistical significance of the correlation was increased by excluding data from Artiodactyls [12]. Some researchers consider this to be related to metabolic activity of the species; other studies have also observed a decrease in erythrocyte size with increasing activity level [18]. Ultimately, for each of these theories there are counterarguments, with new examples and ideas surfacing regularly. The enormous number of vertebrate species and the degree of complexity required when considering evolutionary characteristics, habitat, activity level, and general anatomy and physiology makes the development of a unified understanding of cell size an extraordinarily complex problem.

Despite disagreement about why red blood cell sizes vary so much, there are a few generally accepted trends concerning cell size and hemoglobin. A study of 441 mammalian, avian and reptilian species representing 101 families found a strong positive correlation between mean cell volume and mean cell hemoglobin (Figure 7) – in other words, large cells have more hemoglobin. [6]
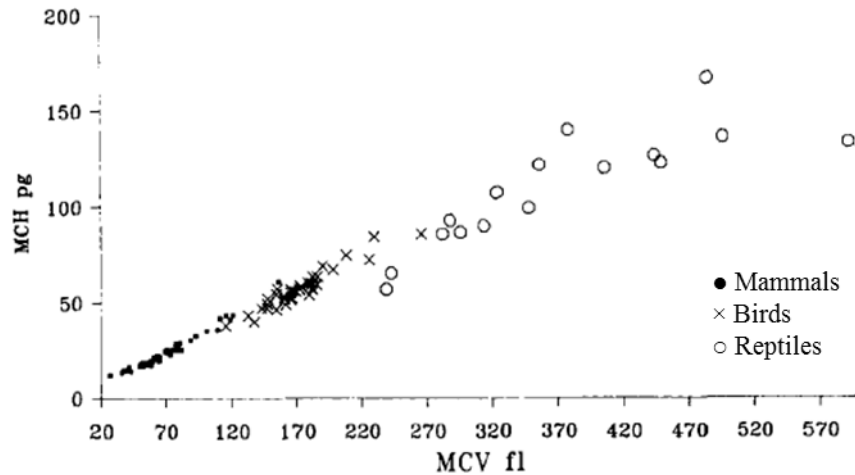
Figure 7. From [6]. Mean cell hemoglobin (MCH) versus mean cell volume (MCV) for 101 vertebrate families.

Based only on this relationship, one could deduce that animals with smaller cells, and therefore less hemoglobin per cell, may have a larger overall number of cells to increase total hemoglobin. The data support this inverse correlation between mean cell volume and red blood cell count (Figure 8), but with a nonlinear relationship. [6] Similarly, there is an inverse correlation between erythrocyte size and total erythrocyte count [26, 6, 19].
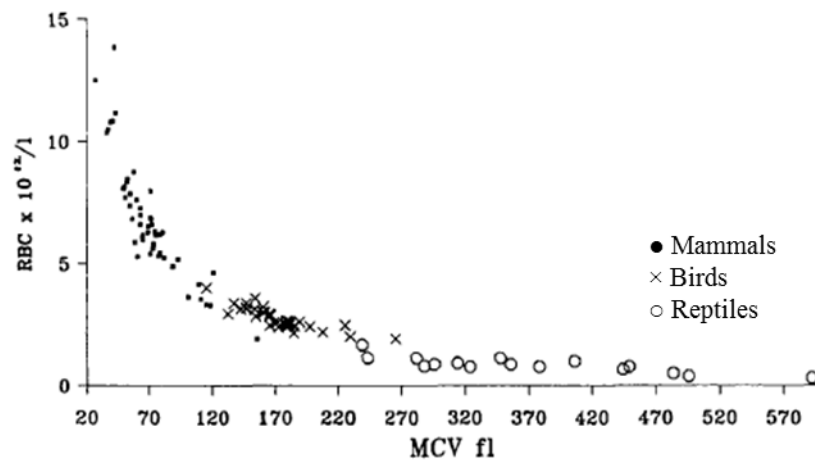
Figure 8. From [6]. Red blood cell count (RBC) versus mean cell volume (MCV) for 101 vertebrate families.

Therefore, mammals and birds have a higher total amount of hemoglobin per unit volume of blood than reptiles. The authors surmise that this is reflective of the oxygen demands of "warm-blooded" (endothermic) animals – mammals and birds – versus "cold-blooded" (exothermic) reptiles. They also note that although bird erythrocytes have greater mean cell hemoglobin than mammals, their overall mean cell hemoglobin concentration is lower, while their packed cell volume (hematocrit) and overall hemoglobin count are larger than in mammals. They suggest that these differences may be attributed to the nucleus present in avian erythrocytes: for the former case, the nucleus occupies additional space in the erythrocyte which would be filled by hemoglobin in mammalian red blood cells of equivalent size, and for the latter, the nucleus is imposing its own oxygen-demands on the erythrocyte, in addition to that required by the bird's tissues.

8

1.3.5 *Life without red blood cells*

The crocodile icefish (family Channichthyidae, Figure 9a) are the only known adult vertebrates without red blood cells [27]. They were first "discovered" by whalers in South Georgia – a British territory due east of the southernmost tip of South America – in the early 1900s, who dubbed them "bloodless fish" for their colorless blood (Figure 9b). Swedish professor Johan T. Rudd began to research them after repeated reports from whalers and biologists in the area, and found that their circulatory fluid contained ~1% white blood cells by volume and no erythrocytes. [28] In fact, Rudd found that the plasma lacked hemoglobin entirely. Instead, the very low water temperature (-1.8°C to 1.55°C) of their Antarctic habitat diminishes the oxygenation requirements of the icefish while simultaneously resulting in water with a much higher oxygen solubility than is found in warmer waters [28, 29]. The latter allows the crocodile icefish to oxygenate from water passed over the gills, with O_2 dissolved directly into the plasma and circulated without the use of hemoglobin [27].
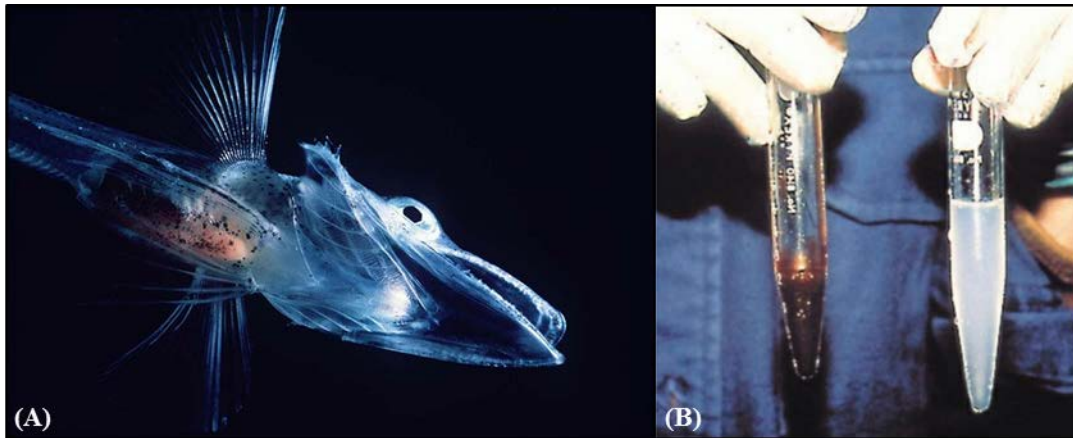
Figure 9. (A) Crocodile icefish from Antarctica (used under Creative Commons license, CC BY-SA 3.0, https://commons.wikimedia.org/w/index.php?curid=207851), (B) from [27] freshly drawn-blood from hemoglobin-expressing notothenioid fish (left) and hemoglobinless Antarctic icefish (right)

1.4 Comparative Studies of Vertebrate Blood Flow

The viscosity of whole blood is dependent on shear rate, temperature, hematocrit, plasma viscosity, red blood cell characteristics and tubing diameter. Viscometers and rheometers provide the means to precisely control flow profile, shear rate and temperature, and are commonly used in hemorheology studies. For suspension flow, and particularly for blood, as flow is induced the suspended particles or cells migrate away from the walls, changing the apparent viscosity of the solution. This change is negligible for flow in channels or vessels greater than 500µm wide. However, it becomes important as diameters decrease below that size; furthermore, as it becomes relevant, the variations in cell characteristics which contribute to migration also become important. This is covered in greater detail in Chapter 2. The important point is that the results of studies of blood viscosity in large channels cannot be extrapolated to the microscale channels of lab-on-a-chip devices [30]. The rheology of human blood has been extensively studied in both viscometers and microscale vessels, but the existing comparative work in non-human blood has focused on flow either in large viscometers or in capillary-size vessels. A brief review of such studies is presented here.

1.4.1 Viscometer studies

Amin and Sirs [31] studied blood in horse, sheep, cattle, goat, camel, pig, dog, rabbit and man, using solid lithium heparin as an anticoagulant. They compared blood viscosity at low (11.5 s^{-1}) and high (230 s^{-1}) shear rates in a Wells-Brookfield viscometer and a Coulter-Harkness capillary viscometer (500 μm inner diameter). Results are shown in Figure 10. They concluded that at high shear rates, where horse and camel blood had the highest relative viscosity, viscosity is dominated by shape factor and erythrocyte flexibility. At low shear rates, horse and human blood were the most viscous, suggesting that erythrocyte aggregation is also important, and that less flexible cells have a lower tendency to aggregate.
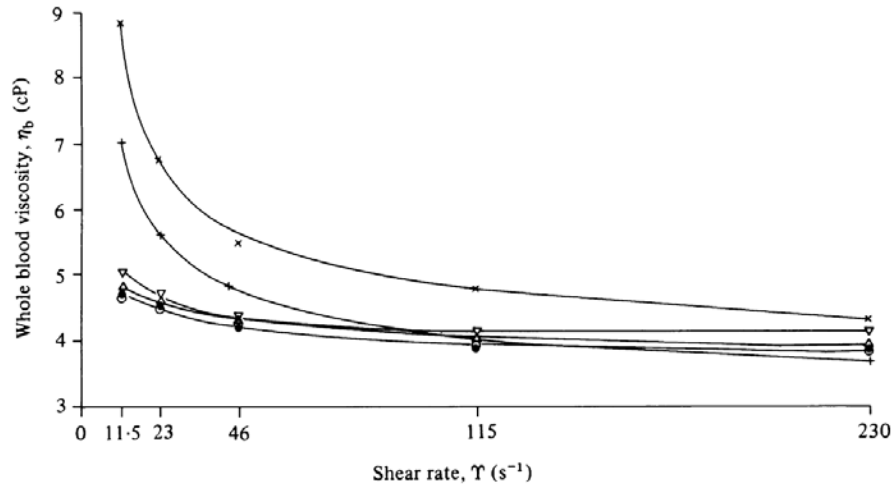
Figure 10. From [31] "The effect of shear rate (s-1) on whole blood viscosity at 37.5°C and haematocrit 30% for (+) man, (x) horse, (●) sheep, (△) goat, and (▽) camel."

In 1969, Usami et al. [32] studied heparinized elephant, human, dog, sheep and goat blood in a CDM coaxial cylinder viscometer at shear rates from 0.052 s^{-1} to 52s^{-1}, at hematocrits up to 85%. Elephant, human and dog blood all exhibited a strong viscosity dependence on hematocrit, with elephant blood consistently the most viscous of the three at all hematocrits (Figure 11). Sheep and goat blood, on the other hand, did not show a strong hematocrit dependence until ~40%, at which point viscosity increased rapidly, such that at 85-95% hematocrit, they were the most viscous of all blood types.

10
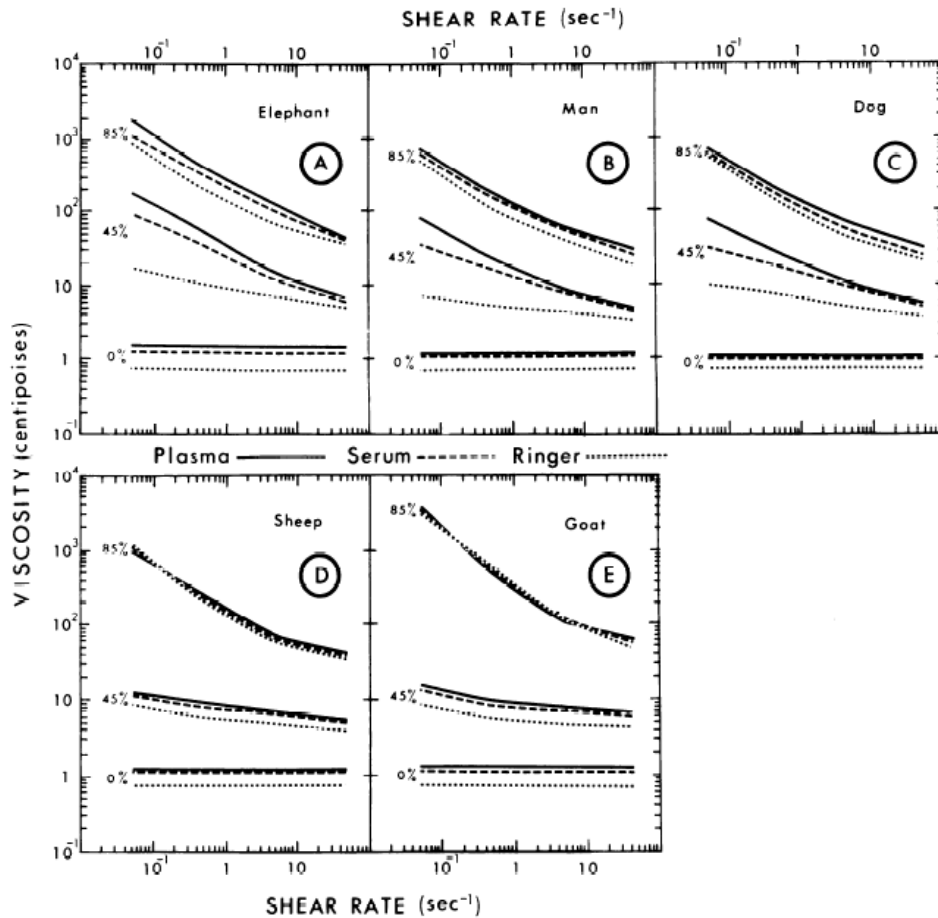
Figure 11. From Usami et al [32]. Relationship of viscosity and shear rate for elephant, man, dog, sheep and goat blood in a cylindrical viscometer.

Windberger et al [33] studied horse, pig, dog, cat, rat, cattle, sheep, rabbit and mouse blood in a Contraves LS30 viscometer (Couette co-axial cylinder, shear rates of 0.7 s^{-1}, 2.4 s^{-1}, and 94 s^{-1}) with K-EDTA as an anticoagulant. They also measured erythrocyte aggregation under differing conditions for each species to analyze the role of aggregation in whole blood viscosity. Each species had differing hemorheological behaviors dependent on shear rate and aggregation. At low shear rate, horse, rat, pig, dog and cat had high whole blood viscosity, while cattle, sheep, rabbit and mouse blood were less viscous. With the exception of the rat, the blood cells for the species in the former group are known to aggregate, and this behavior was likely an important factor. The authors were surprised at the inclusion of rat blood in that group, and performed additional experiments to understand why the rat blood viscosity was elevated; accounting for aggregation, hematocrit and suspending fluid viscosity did not explain this difference, and they concluded that other factors such as red blood cell characteristics must be involved. At high shear rate, they observed less variation in whole blood viscosity across all species.

1.4.2 Tubing-based studies

In 1918, J. W. Trevan [34] constructed capillary viscometers with 800μm and 200μm diameters, and compared blood at different hematocrits suspended in solutions of differing viscosity. The study included sheep, dog, cat and human red blood cells. However, the author did

11

not discuss the size of the blood cells, as the goal was to understand the role of hematocrit in relative blood viscosity. Comparison of the results across species is complicated by the fact that hematocrits were not consistent across species. The author did not attribute any viscosity differences to cell characteristics.

Gaehtgens et al [35] prepared suspensions of Peking duck blood cells anticoagulated with heparin in buffered Ringer-Tyrode solutions and perfused them through glass capillaries 5-11µm in diameter. They found the relative viscosity of the duck blood to be 4-6 times higher than similar human red blood cell suspensions at the same hematocrit and flow rate. The authors did not include measurements or discussion of the characteristics of duck red blood cells aside from the presence of a nucleus.

Stone et al [30] studied heparinized goat, sheep, dog, human, camel and llama blood at 0 – 90% hematocrit in a 600µm diameter Ostwald viscometer at $100s^{-1}$. Erythrocytes suspended in native plasma and in albumin had similar trends. At all hematocrits, goat blood exhibited the highest relative viscosity, human blood had the lowest, and sheep blood was intermediate between the two (Figure 12). Camel and llama blood, however, had among the lowest viscosities at low hematocrit but were as viscous as goat blood at high hematocrit. This is the earliest comparative study to use highly precise measurement techniques; the authors note earlier studies which failed to identify a size or shape dependence, but used less sophisticated equipment.
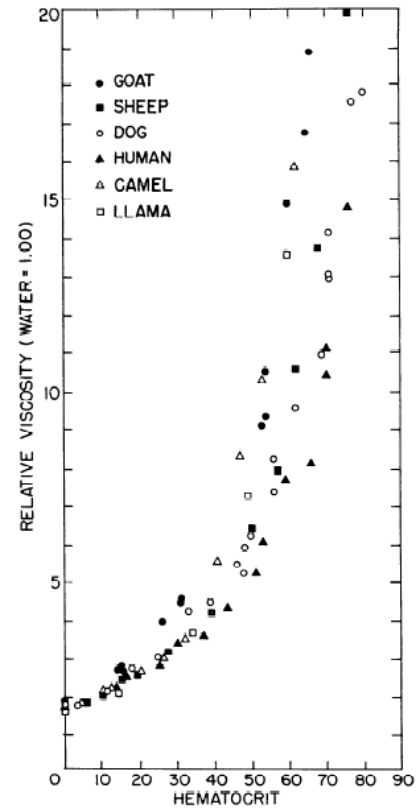
Figure 12. From Stone et al. [30] Relative viscosity versus hematocrit for goat, sheep, dog, human, camel and llama red blood cells suspended in homologous plasma

1.4.3 Notes on anticoagulant selection

Anticoagulants are necessary for all *ex vivo* handling of blood. Common options include the potassium salt of ethylene-diamine-tetraacetic acid (K_3-EDTA), heparin, sodium-citrate, and manual defibrination of whole blood. Historically there has been some disagreement as to the relative effects of various anticoagulants on blood flow properties. Rampling and Sirs evaluated erythrocyte deformability based on centrifugal packing rate; using this technique, they concluded that for storage periods of less than 24 hours, heparin had the lowest impact, while defibrination with glass beads had the largest immediate impact on cell flexibility. As storage times were extended, heparin and EDTA treated cells became progressively less deformable, while ACD-treated cells retained their initial flexibility for the longest period of time [36]. Heparin has been shown to alter rheological behavior by decreasing hematocrit and increasing aggregation, as well as decreasing red blood cell deformability by changing the number of reticulocytes (young erythrocytes) in the sample. The change in cell deformability is of particular interest, and several explanations are considered possible: changes in the lipid bilayer as a result of increased cholesterol, loss of symmetry in the bilayer, or other membrane-cytoskeleton related changes [37]. K_3-EDTA is currently the recommended anticoagulant for hemorheological studies at it has the least effect on the stiffness of human red blood cells [38].

12

However, these recommendations are based on human red blood cells, and some studies in vertebrate red blood cells have found different effects. Nemeth [39] et al. compared red blood cell deformability in rats and beagle dogs when treated with K_3-EDTA and sodium-heparin. They found that red blood cell deformability was identical for both anticoagulants in rats, but that heparin increased deformability in beagle red blood cells. In domestic animals, excess dosage with unfractionated heparin will cause excess agglutination in horses. Excess EDTA may cause echinocytosis in many species and induce the formation of keratocytes in stored cat blood [14]. EDTA has been observed to cause hemolysis in reptile blood, so heparin is the recommended anticoagulant for those vertebrates [18]. EDTA is recommended for avian blood, as other anticoagulants will cause cell clumping [40].

1.5   Summary

The impact of varying red blood cell characteristics on blood flow is important both from a fundamental biophysics perspective as well as in the development and design and microfluidic devices utilizing whole blood. Despite extensive research on human blood in these flow conditions, there is little similar research utilizing and comparing different types of animal blood.

Works Cited:

[1]   G. Gulliver, "On the Red Corpuscles of the Blood of Vertebrata and on the Zoological Import of the Nucleus, with Plans of their Structure, Form, and Size (on a A Uniform Scale), in many of the different Orders," *Proceedings of the Zoological Society of London,* vol. 30, no. 1, pp. 91-103, 1862.

[2]   R. Fåhræus, "The suspension stability of the blood," *Physiological Reviews,* vol. 9, no. 2, pp. 241-274, 1929.

[3]   C. G. Caro, T. J. Pedley, R. C. Schroter and W. A. Seed, The Mechanics of the Circulation, 2nd Edition, Cambridge University Press, 2011.

[4]   U. Windberger and O. K. Baskurt, "Comparative Hemorheology," in *Handbook of Hemorheology and Hemodynamics*, IOS Press, 2007, pp. 267-285.

[5]   S. Al-Roubaie, E. D. Jahnsen, M. Mohammed, C. Henderson-Toth and E. A. Jones, "Rheology of embryonic avian blood," *American Journal of Physiology,* vol. 301, no. 6, pp. H2473-H2481, 2011.

[6]   C. M. Hawkey, P. M. Bennett, S. C. Gascoyne, M. G. Hart and J. K. Kirkwood, "Erythrocyte size, number and haemoglobin content in vertebrates," *British Journal of Haematology,* vol. 77, no. 3, pp. 392-397, 1991.

[7]   T. M. Fischer, "Shape memory of human red blood cells," *Biophysical Journal,* vol. 86, no. 5, pp. 3304-3313, 2004.

[8]   M. Nikinmaa, Zoophysiology (Volume 28): Vertebrate Red Blood Cells: Adaptations of function to respiratory requirements, Berlin: Springer-Verlag, 1990.

[9]   J. Dupire, M. Socol and A. Viallat, "Full dynamics of a red blood cell in shear flow," *Proceedings of the National Academy of Sciences,* vol. 109, no. 51, pp. 20808-20813, 2012.

[10] C. Uzoigwe, "The human erythrocyte has developed the biconcave disc shape to optimise the flow properties of the blood in the large vessels," *Medical Hypotheses,* vol. 67, pp. 1159-1163, 2006.

[11] The Editors of Encyclopedia Britannica, "Red Blood Cell," Encyclopedia Britannica, 1 May

2015. [Online]. Available: https://www.britannica.com/science/red-blood-cell. [Accessed 12 July 2016].

[12] T. R. Gregory, "Nucleotypic effects without nuclei: Genome size and erythrocyte size in mammals," *Genome,* vol. 43, pp. 895-901, 2000.

[13] G. Gulliver, "On the size and shape of red corpuscles of the blood of vertebrates, with drawings of them to a uniform scale, and extended and revised tables of measurement," *Proceedings of the Zoological Society of London,* pp. 474-495, 1875.

[14] J. W. Harvey, Atlas of Veterinary Hematology, Philadelphia: W.B. Saunders Company, 2001.

[15] R. Yagil, U. A. Sod-Moriah and N. Meyerstein, "Dehydration and camel blood. II. Shape, size and concentration of red blood cells," *American Journal of Physiology,* vol. 226, no. 2, pp. 301-304, 1974.

[16] P. Agre and J. C. Parker, Red Blood Cell Membranes: Structure, Function, Clinical Implications, CRC Press, 1989.

[17] G. K. Snyder and B. A. Sheafor, "Red Blood Cells: Centerpiece in the Evolution of the Vertebrate Circulatory System," *American Zoologist,* vol. 39, pp. 189-198, 1999.

[18] H. Arikan and K. Çicek, "Haematology of amphibians and reptiles: a review," *Northwestern Journal of Zoology,* vol. 10, no. 1, pp. 190-209, 2014.

[19] W. Frair, "Turtle Red Blood Cell Packed Volume, Sizes, and Numbers," *Herpetologica,* vol. 33, no. 2, pp. 167-190, 1977.

[20] H. M. Smith, "Cell Size and Metabolic Activity in Amphibia," *Biological Bulletin,* vol. 48, no. 5, pp. 347-378, 1925.

[21] F. J. Vernberg, "Hematological Studies on Salamanders in Relation to Their Ecology," *Herpetologica,* vol. 11, no. 2, pp. 129-133, 1955.

[22] S. Garrison, "Cell Size in the Amphiuma," *Bios,* vol. 20, no. 4, pp. 237-243, 1949.

[23] C. P. Mangum, "Respiratory function of the red blood cell hemoglobins of six animal phyla," in *Comparative and environmental physiology*, Berlin, Springer-Verlag, 1992, pp. 117-149.

[24] G. K. Snyder, "Erythrocyte evolution: the significance of the Fahraeus-Lindqvist Phenomenon," *Respiration Physiology,* vol. 19, pp. 271-278, 1973.

[25] V. M. Gavrilov, "Origin and development of homoiothermy: A case study of avian energetics," *Advances in Bioscience and Biotechnology,* vol. 4, pp. 1-17, 2013.

[26] D. L. Ryerson, "A preliminary survey of reptilian blood," *Journal of Entomological Zoology,* vol. 41, pp. 49-55, 1949.

[27] B. M. Sidell and K. M. O'Brien, "When bad things happen to good fish: the loss of hemoglobin and myoglobin expression in Antarctic icefishes," *Journal of Experimental Biology,* vol. 209, pp. 1791-1802, 2006.

[28] J. T. Rudd, "Vertebrates without erythrocytes and and blood pigment," *Nature,* vol. 173, no. 4410, pp. 848 - 850, 1954.

[29] G. F. Holeton, "Oxygen uptake and circulation by a hemoglobinless Antarctic fish (Chaenocephalus acertaus Lonnberg) compared with three red-blooded Antarctic fish," *Comparative Biochemistry and Physiology,* vol. 34, pp. 457-471, 1970.

14

[30] H. O. Stone, H. K. Thompson, Jr. and K. Schmidt-Nielsen, "Influence of erythrocytes on blood viscosity," *American Journal of Physiology,* vol. 214, no. 4, pp. 913-918, 1968.

[31] T. M. Amin and J. A. Sirs, "The blood rheology of man and various animal species," *Quarterly Journal of Experimental Physiology,* vol. 70, pp. 37-49, 1985.

[32] S. Usami, S. Chien and M. I. Gregersen, "Viscometric characteristics of blood of the elephant, man, dog, sheep and goat," *American Journal of Physiology,* vol. 217, no. 3, pp. 884-890, 1969.

[33] U. Windberger, A. Bartholovitsch, R. Plasenzotti, K. J. Korak and G. Heinze, "Whle blood viscosity, plasma viscosity and erythrocyte aggregatoin in nine mammalian species: reference values and comparison of data," *Experimental Physiology,* vol. 88, no. 3, pp. 431-440, 2003.

[34] J. W. Trevan, "The viscosity of blood," *Biochemical Journal,* vol. 12, pp. 60-71, 1918.

[35] P. Gaehtgens, G. Will and F. Schmidt, "Comparative Rheology of Nucleated and Non-Nucleated Red Blood Cells," *Pflügers Archiv,* vol. 390, pp. 283-287, 1981.

[36] M. Rampling and J. A. Sirs, "The Effect of Haematocrit and Anticoagulants on the Rate of Packing of Erythrocyte by a Centrifuge," *Physics in Medicine and Biology,* vol. 15, no. 1, pp. 15-21, 1970.

[37] L. Heilmann, W. Rath, K. Pollow and R. L. Bick, "The rheological changes after cesarean section: The influence of low molecular weight or unfractionated heparin on the rheological properties of blood," *Clinical Hemorheology and Microcirculation,* vol. 37, pp. 211-218, 2007.

[38] O. K. Baskurt, M. Boynard, G. C. Cokelet, P. Connes, B. M. Cooke, S. Forconi, F. Liao, M. R. Hardeman, F. Jung, H. J. Meiselman, G. Nash, N. Nemeth, B. Neu, B. Sandhagen, S. Shin, G. Thurston and J. L. Wautier, "New Guidelines for Hemorheological Laboratory Techniques," *Clinical Hemorheology and Microcirculation,* vol. 42, no. 2, pp. 75-97, 2009.

[39] N. Nemeth, O. K. Baskurt, H. J. Meiselman and I. Miko, "Species-specific effects of anticoagulants on red blood cell deformability," *Clinical Hemorheology and Microcirculation,* vol. 43, pp. 257-259, 2009.

[40] T. W. Campbell, "Chapter 9: Hematology," in *Avian Medicine: Principles and Application*, Lake Worth, Wingers Publishing, Inc., 1994, pp. 176-198.

Chapter 2
Blood Flow in Arterioles

This research covers *in vitro* blood flow in the size range comparable to arterioles within the human body. The importance of hemorheological studies in this range of vessel diameters was covered in Chapter 1. This chapter provides additional background on the physics of blood flow in these vessels (10-300μm diameter).

2.1   Studies in Human Blood

The early 1900s blood flow experiments of Swedish researchers Robin Fåhræus and Torsten Lindqvist spurred modern research in hemodynamics at the microscale level [1], and ultimately this dissertation project. Their studies arose from a renewed European interest in blood sedimentation during the 1920s, but the historical investigation of this phenomenon dates back to ancient Greece.

2.1.1 Evolution of the studies of blood sedimentation

Fåhraeus begins his pivotal 1929 paper [2] with an interesting historical review, contextualizing the importance of hemodynamics and hemorheology in human history. Briefly, Hellenic physicians observed and labeled four "humors" – the vascular fluids comprising blood – based on the discrete phases visible in clotted blood. Hippocrates is credited as the first to develop a medicinal theory of these humors; an increase in vascular *phlegma* (what we now know to be fibrin) was considered to be "the most important cause of almost all diseases" [2]. Even as human understanding of blood and disease advanced in subsequent centuries, this correlation between high fibrin levels (in the form of the buffy coat), increased blood sedimentation rate and disease states remained at the core of medicine, leading to treatments such as the infamous blood-letting, which persisted into the 1800s. Research and speculation on the interplay between fibrin and increased sedimentation velocity continued until the end of the 19th century, when studies quickly ceased. When Fåhraeus shared his accidental observations on the increased red blood cell sedimentation rate in pregnant women, interest was renewed and thousands of papers were published in the span of 10-15 years, particularly in Scandinavia and Germany.

2.1.2 Sedimentation velocity and the importance of erythrocyte aggregation

As the study of blood sedimentation advanced, the role of erythrocyte aggregation, and ultimately the aggregation process itself became of central importance. Factors such as fibrin concentration and hematocrit were demonstrably important, but rouleaux formation is also critical. Although this dissertation does not address differences in sedimentation rates, aggregation is an important blood characteristic to understand.

Erythrocyte aggregation is a reversible process in which red blood cells align in chains called rouleaux. Eventually these rouleaux will cluster together to form spherical globules. Both of these structures can be observed in Figure 1. It should be noted that blood cell sedimentation is negligible until rouleaux and rouleaux globules have formed. Aggregation happens only at very low shear rates – a disturbance in the fluid will disrupt the chains and the red blood cells will separate completely [3]. However, rouleaux can be observed in some capillary beds, and particularly in horses, which have blood that has an extremely strong tendency to aggregate [2].

16

Figure 1. Photo from TL Fabry [3] of sedimenting erythrocytes at x16 magnification. Slim rouleaux are beginning to cluster into spheres

Aggregation is enhanced in various disease states as well as during the course of pregnancy.

Aggregation is a different mechanism from the irreversible coagulation process, which includes a chemical cascade that can be blocked through the use of anticoagulants such as heparin, sodium-citrate, or K_3 EDTA. Aggregation can also be prevented by suspending red blood cells in medium lacking electrolytes and certain macromolecules. There are a number of explanations and detailed studies of the aggregation mechanism – both the properties of the suspending cell medium and cellular factors are considered important [4, 5, 6, 7, 8] – but disagreement as to the relative importance of these and other factors persists.

Finally, although aggregation is a normal occurrence in humans and exceedingly common in horses, it is actually a very rare phenomenon among animals. Aggregation has only been observed in humans, horses, pigs, buffalo and cats, and is considered negligible or nonexistent in other species [9, 10].

2.1.3 The Fåhræus Effect

As Fåhraeus and other researchers pursued a greater understanding of blood sedimentation and aggregation *ex vivo*, the *in vivo* behavior of blood also became important to understand, particularly in small vessels where aggregation could be observed. At this point, there was a parallel body of research on the flow of suspensions in small tubes, giving hemodynamic researchers a relevant framework for their own experiments. Some of these suspension flow models are applicable to the present thesis, and are discussed in Chapter 6.

To investigate the flow of blood from large vessels through the microcirculatory system, Fåhraeus streamed blood through glass capillaries of varying diameters (50 - 1500μm) and measured the volume of the plasma and erythrocytes in each capillary. These values were compared to the bulk hematocrit of the blood. His results, shown in Figure 2, demonstrate that hematocrit is constant until the tubing diameter decreases below 100 μm, at which point the volume of red blood cells in the capillary drops noticeably.

DIAMETER OF THE TUBES	VOLUME OF THE BLOOD		AVERAGE VELOCITY OF THE ERYTHROCYTES; THAT OF THE PLASMA = 100
	Erythrocytes	Plasma	
mm.	per cent	per cent	
1,100	40.5	59.5	100
0,750	40.1	59.9	101
0,450	39.8	60.2	103
0,250	39.2	60.8	106
0,095	33.6	66.4	135
0,050	28.0	72.0	175

Figure 2. Results from Fåhraeus [2] on diameter-dependence of vessel hematocrit

17

The dependence of hematocrit on vessel diameter is now referred to as the Fåhraeus Effect. As is noted in the rightmost column of Figure 2, this decrease in hematocrit is accompanied by – and is, in fact, caused by – an increase in the average velocity of the erythrocytes compared to the plasma velocity. It is critical to understand that the composition of the blood in the larger container feeding the capillary and the composition of the blood being collected at the vessel outlet is *identical*. As Fåhraeus says, "the composition of a drop from bleeding narrow vessels is not the same as the composition of the blood in the vessels themselves." At any discrete instant, the blood in the capillary will have a lower proportion of blood cells and a higher proportion of plasma than either the inlet or outlet reservoirs; however, this lesser proportion of blood cells is moving many times more quickly than the plasma, such that the outlet is being refilled with blood cells more rapidly than it is with plasma – in fact, at the rate exactly recreating the original proportion. Thus, the outlet reservoir has an identical hematocrit to the inlet reservoir, despite the cell-poor vessel connecting them. This can also be considered from the perspective of a finger-prick: the blood that wells up has the same hematocrit as found in the body overall, rather than the low (5-20%) hematocrit of the capillaries.

These experiments have been recreated in various forms a number of times over the past eight decades. The decrease in hematocrit in smaller vessels is also documented *in vivo*. An excellent example of this is depicted in Figure 3, which shows the decline in hematocrit from 30% in the small arterioles to ~7% in capillaries and once again increasing as the blood enters the venous system.
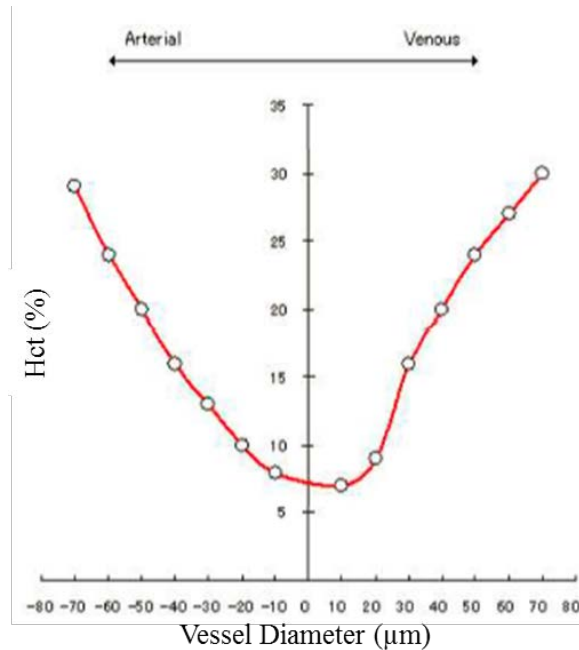
Figure 3. From [11]. Blood vessel hematocrit in the mesentery of a cat.

2.1.4 The Fåhræus-Lindqvist Effect

As hematocrit diminishes with vessel diameter, there are related changes in the hemodynamics – most importantly, a decrease in viscosity. Torsten Lindqvist and Fåhraeus studied this experimentally with an apparatus similar to that used in the hematocrit experiments. At the time, researchers were using Ostwald viscometers, which utilized vertical capillary tubes

18

where blood flow was driven only by gravity. Fåhraeus and Lindqvist wanted to avoid the sedimentation bias which would be introduced over time in such a device, and so created a horizontal viscometer with pressure-driven flow through narrow glass capillaries. They measured the inlet pressure, and calculated the viscosity of the blood (their own blood) by comparing the results to analogous experiments with water.

Their results (Figure 4) coincided with the drop in hematocrit – as channel diameter decreased below 300μm, the relative viscosity of the blood also began to drop. Thus, they concluded: "The law of Poiseuille does not apply to the flow of blood in capillary tubes of a diameter below about 0.3mm."
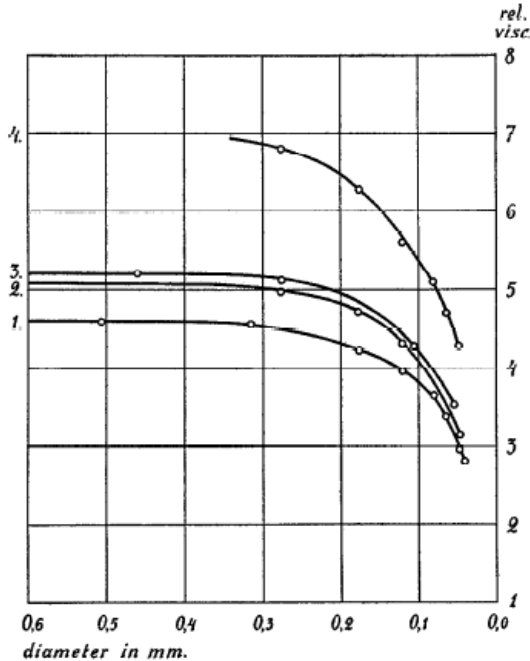
Figure 4. Results from Fåhraeus and Lindqvist, 1930 [12]. The vessel diameter decreases from left to right, with a decrease in viscosity (relative to water) beginning at 0.3mm. Series 1 and 2 were blood from Torsten Lindqvist (relative plasma viscosity = 1.63 and 1.65), Series 3 is from Robin Fåhraeus (relative plasma viscosity = 1.60), and Series 4 is from Lindqvist but with part of the plasma removed (relative plasma viscosity = 1.72) to investigate a higher viscosity blood sample.

This diameter-dependence of blood viscosity is known as the Fåhraeus-Lindqvist Effect, and has been an area of significant study since it was first published.

2.2 Cell-Free Layer

The development of a cell-free layer of plasma along the vessel walls is central to the Fåhraeus and Fåhraeus-Lindqvist Effects. Regardless of particle type and the presence of any type of particle migration, a less particle-laden regime along the wall would be mathematically expected. This is illustrated in Figure 5.
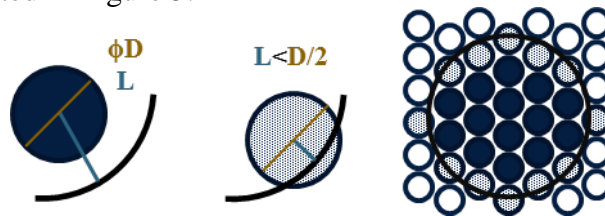
Figure 5. Cross-sectional illustration of the natural cell-free layer for theoretical particle-laden flow through a circular channel. Left: a particle with diameter D, with L representing the distance from the particle's center to the channel wall. Center: If L < D/2, the particle's bounds would extend beyond the flow channel – an impossibility. Thus, the closest any particle can be to the wall is L=D/2. Right: The resulting cross-section of particle-laden flow for close-packed particles. The dark blue particles are able to flow and the light blue particles either must not exist or would be physically pushed inwards.

19

If flow properties such as slip and shear are ignored, there are theoretical instances where the packing fraction at the wall is identical to the overall packing fraction (e.g. particles with appropriately-sized quadrilateral cross-sections in an ideal formation for flow through a quadrilateral channel). Ignoring these few and unlikely exceptions, which are virtually irrelevant when dealing with biological particles such as cells, it is apparent that the possible maximum packing fraction at D ≤2 from the wall will always be less than the possible maximum packing fraction at >D/2 from the channel wall.

This is an interesting basic consideration, but does not account for the 1-3μm cell-free layer that forms in blood vessels. In this case (and other cases, as will be seen), there is an additional factor at work.

2.2.1 *Particle migration*

The first step in examining particle migration is to consider how rigid particles behave near channel or vessel walls. In Stokes flow, where viscous effects strongly dominate inertial effects (Reynold's Number <<<1), the problem can be simplified, and it can be shown that no particle migration will occur (Figure 6).
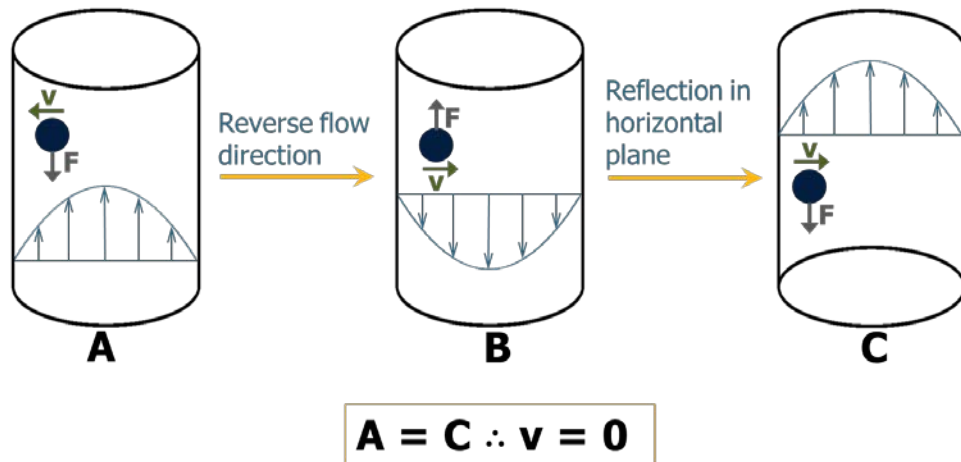
Figure 6. Assume Stokes flow where Re ~ 0. (A) the particle is falling in Stokes Flow, with a downwards force (F) and an arbitrary direction of velocity (v) chosen to be towards the channel walls. In (B) the flow direction is reversed, changing the direction of F and the flow, and therefore the direction of v. This diagram can then be reflected in the horizontal plane to produce (C), where the force F and flow direction are identical to (A). The only difference between (C) and (A) is the direction of v – thus, v=0 and no lateral particle migration will occur.

This is an interesting first look, but physiological flows and those occurring in laboratory settings are unlikely to be creeping flow. Therefore, it is important to examine what happens when inertial forces are non-negligible. This dimensional analysis is thoroughly covered by [13]; rather than entirely repeating that discussion here, only the main points will be addressed.

Rigid particles in faster flow are subject to shear, slip, and interactions with the vessel wall. As illustrated in Figure 7, these forces have an equilibrium point at ~0.6R – this is known as the Segre-Silberberg Effect for the researchers who first observed it [14]. However, the migration induced by these forces is *very slow*; for most practical applications, such as flows seeded with rigid particles for particle image velocimetry, this migration can be considered to be negligible.

20
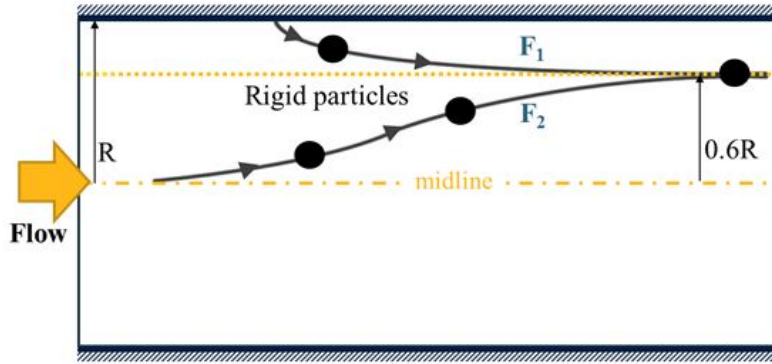
Figure 7. Illustration of rigid particle migration in flow. Rigid particles are subject to two primary forces – F_1, resulting from shear and the vicinity of the vessel wall, and F_2 resulting from slip and shear. These forces are equal at $6/10^{ths}$ of the radius – over a very long period of time, rigid particles will migrate to this position.

The external forces acting upon a deformable particle are the same as for a rigid particle. However, the ability of a particle to deform causes an entirely different reaction. First consider the case of a rigid particle near a wall subject to shear flow over a time- and length-scale where slow particle migration is irrelevant. At an instantaneous moment shown in Figure 8a, the shear flow will cause a spherical rigid particle to rotate, but its trajectory will remain unchanged. This rotation may become more pronounced or change slightly for a non-spherical particle, as in Figure 8b, but the downstream trajectory will remain the same, because although lift is possible for certain orientations of non-spherical particles, overall no net lift is possible. An excellent discussion of this in the context of the mirror symmetry time reversal theorem is presented by Amini et al [15].
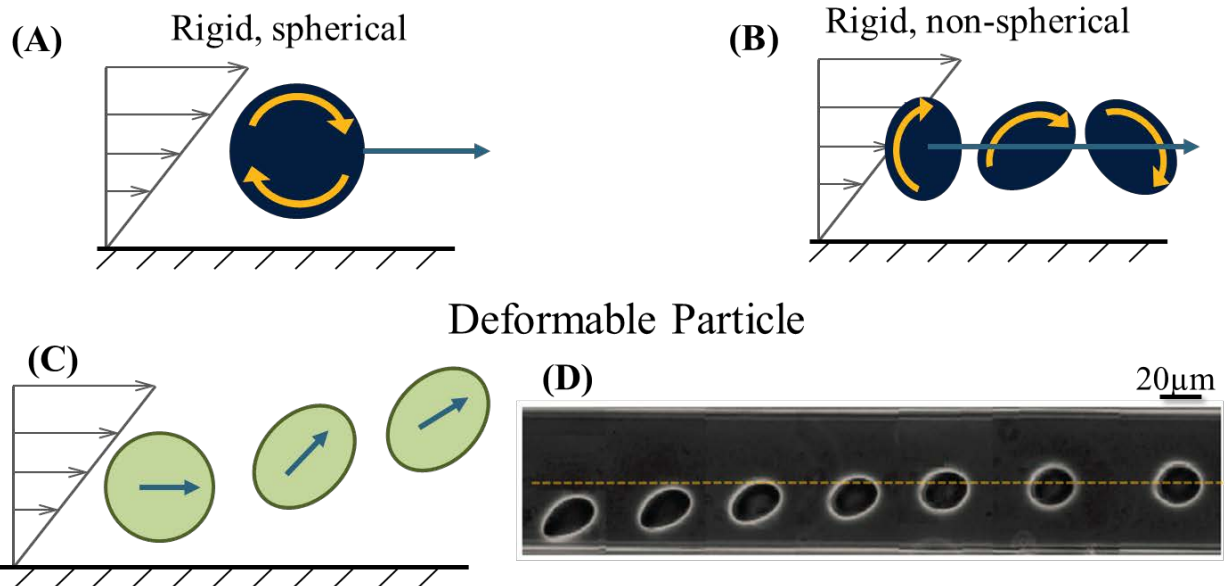
Figure 8. (A) Rotation in shear flow with no lift for a spherical rigid particle (B) Rotation in shear flow with no lift for a non-spherical rigid particle (C) Deformation and lift for a spherical particle in shear flow (D) Micrographs of deformation and lift to centerline (yellow line) for a deformable particle, from Coupier et al [16].

21

The same shear forces that cause a rigid particle to rotate will result in the elongation of a deformable particle, which will be maintained while the shear rate across the particle surface is not in equilibrium (Figure 8c). In addition, this deformation exposes a higher instantaneous cross-section of the particle to the wall forces, further inducing migration. This is a significantly faster process than rigid particle migration; Figure 8d shows optical micrographs of this process for a 19μm diameter deformable particle travelling at 920μm/s; the move from wall to centerline occurs over the span of 2.5cm, taking ~25 seconds [16].

The diagram and Buckingham Pi analysis of this lift force is shown in Figure 9. Ultimately, the lift force is affected by the deformability of the particle (represented by the capillary number, Ca), the ratio of the internal particle viscosity to that of the carrying fluid, the diameter of the particle relative to channel size, and the relative position within the channel.

3 Units:

[Mass]
[Length]
[Time]

8 Variables:

$F - [MLT^{-2}]$ $a - [L]$
$\mu_f - [ML^{-1}T^{-1}]$ $d - [L]$
$\mu_d - [ML^{-1}T^{-1}]$ $H - [L]$
$U - [LT^{-1}]$ $Ca - [-]$

Capillary Number, Ca

$$Ca = \frac{\mu \dot{\gamma} a}{G}$$

↑Ca = ↑deformability

5 Dimensionless Groups

$$\frac{F}{\mu U a} = f\left(Ca, \frac{\mu_d}{\mu_f}, \frac{a}{H}, \frac{d}{H}\right)$$
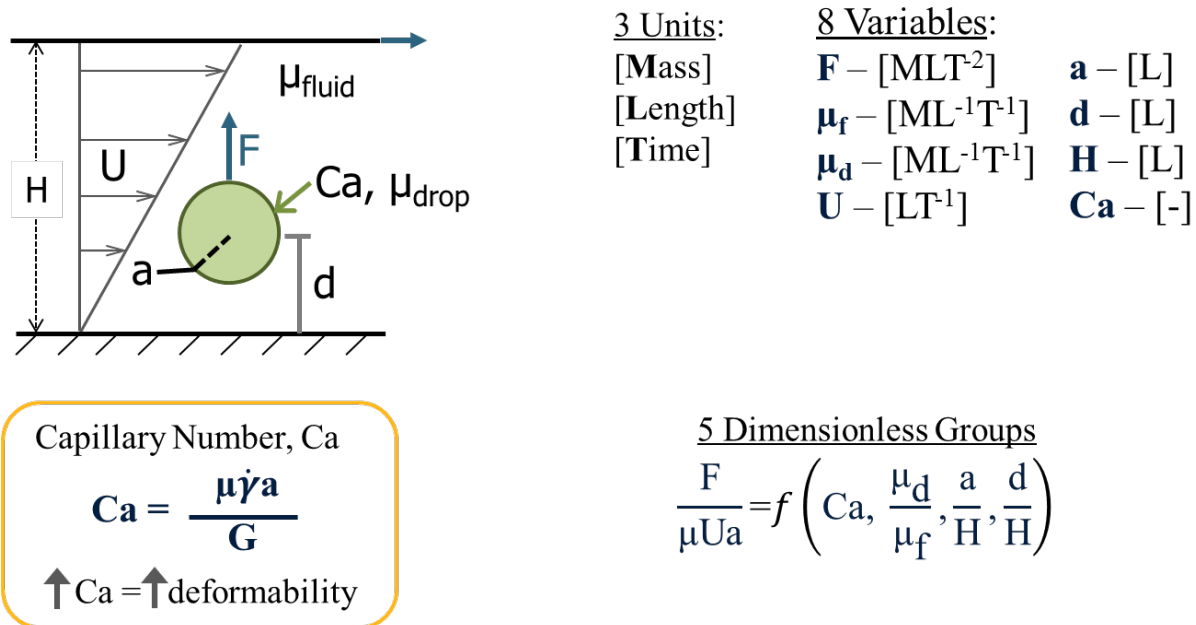
Figure 9. Lift force (F) for a deformable particle with capillary number (Ca), internal viscosity (μ_{drop}), and diameter (*a*) at a distance (*d*) from the channel wall, suspended in a fluid with viscosity (μ_{fluid}), velocity field (U) and channel width (H). Buckingham Pi theorem states that for a certain number of physical variables (n=8) composed of physical dimensions (k=3), the physically meaningful original equation (p) can be constructed from p = n - k dimensionless parameters.

Several different experimental and numerical analyses of the dimensionless groups in Figure 9 have been performed. Scaling depends on the viscosity ratio and distance relative to the wall and/or center of channel. Overall, the lift force increases with increasing fluid viscosity, particle diameter, and fluid velocity [17, 18]. The viscosity ratio has differing effects on migration velocity depending on particle shape, size and deformability. Increases in the viscosity ratio (μ_d/μ_f) for a red blood cell at rest or stretched in shear flow will result in drastic decreases in the drift velocity away from the wall. This is also true for prolate ellipsoids although the decline in velocity is much less rapid, whereas oblate ellipsoids maintain a nearly steady and quite low migration velocity regardless of viscosity ratio [19].

22

2.2.2 *Suspensions of deformable particles*

This treatment considers the migration behavior of a single deformable particle. However, as particles or cells are added to the system, particle collisions will add an additional force to the system. In laminar flow, these collisions are the result of particles on neighboring streamlines interacting due to the velocity gradient. Distance from the wall and distance between particle centers at the time of collision both influence the outcome, but deformability of each particle is the most important factor. In a collision between particles of differing deformability, the more rigid particle will experience a much larger displacement than the more deformable particle. Displacement of two colliding deformable particles will be greater than that of the deformable particle in the heterogeneous collision, but less than that of the rigid particle [20]. As the system is scaled up to the level of particle-laden flow, these displacements become relevant in the context of blood flow in arterioles. At this level, the outcome depends on the concentration of stiff versus deformable particles. For suspensions such as whole blood with a high concentration of deformable particles (red blood cells) and a low concentration of rigid particles (platelets), the rigid particles will migrate and accumulate towards the channel wall [20]. This high concentration of platelets at the vessel wall is important in facilitating platelet adherence to the vessel wall, a crucial step in the process of coagulation and wound healing [21].

2.2.3 *Influence on blood viscosity*

The development of the cell-free layer due to deformable cell migration away from the vessel walls impacts the overall blood viscosity. In simplified terms, the least viscous component of the suspension – the plasma – dominates the region of the flow with the highest amount of shear stress, essentially acting as a lubricating layer. The impact of this 1-3μm layer depends on the scale of the blood vessel. In very large vessels (>300-500μm), the cell-free layer is negligible in respect to overall tubing diameter, and the red blood cell laden core represents ~100% of the flow. At this size, the red blood cell velocity and whole blood velocity are equal. This is also true in very small vessels where the diameter of the red blood cell is equal to or greater than the diameter of the capillary, which acts as a type of plug flow. [22] It is in the middle of these two regimes – the arteriole size range – where the size of the cell-free layer becomes relevant. In these vessels, the red blood cells are clustered in the faster-moving center of the channel, and have a higher velocity than the average velocity across the entire channel. As vessel size decreases from 300μm to 10μm, the relative size of the cell-free layer increases, as does its lubricating effect. The result is the Fåhraeus-Lindqvist Effect.

2.3   Conclusions

The dynamics of blood flow in arteriole vessels differs significantly from behaviors in larger arteries or much smaller capillaries. Red blood cell properties such as deformability play a major role in hemorheology within these vessels. Blood in arterioles cannot be treated as a homogeneous fluid, as the formation of a cell-free layer induces a distinct heterogeneity across the vessel. Within this same range, viscous forces dominate flow behavior, with *in vivo* Reynolds numbers ranging from 0.005 in 10μm capillaries to ~0.5 in larger 100μm diameter vessels. [23] Shear rates at the wall are much higher than in larger arteries and veins, and flow is quasi-steady, with the pulsatile flow from the hard having a generally negligible effect in this regime.

These unique characteristics of flow in 10-300μm diameter vessels are interesting from a biophysics perspective, and have rightfully garnered significant attention from the research community. With the rise of biomedical microfluidic devices, however, research in this regime is

23

even more critical. The interplay between red blood cell characteristics and hemorheology is complex, but an understanding of the fundamentals provides some context for the experimental setup and results in the next chapters.

Works Cited:

[1]   H. L. Goldsmith, G. R. Cokelet and P. Gaehtgens, "Robin Fahraeus: evolution of his concepts in cardiovascular physiology," *American Journal of Physiology - Heart and Circulatory Physiology,* vol. 257, no. 3, pp. H1005-H1015, 1989.

[2]   R. Fåhræus, "The suspension stability of the blood," *Physiological Reviews,* vol. 9, no. 2, pp. 241-274, 1929.

[3]   T. L. Fabry, "Mechanism of Erythrocyte Aggregation and Sedimentation," *Blood,* vol. 70, pp. 1572-1576, 1987.

[4]   H. Baumler, B. Neu, E. Donath and H. Kiesewetter, "Basic phenomena of red blood cell rouleaux formation," *Biorheology,* vol. 36, pp. 439-442, 1999.

[5]   E. W. Merrill, E. R. Gilliland, T. S. Lee and E. W. Salzman, "Blood rheology: Effect of fibrinogen deduced by addition," *Circulation Research,* vol. 18, pp. 437-446, 1966.

[6]   S. Asakura and F. Oosawa, "On interaction between two bodies immersed in a solution of macromolecules," *Journal of Chemical Physics,* vol. 22, pp. 1255-1256, 1954.

[7]   G. Barshtein, I. Tamir and S. Yedgar, "Red blood cell rouleaux formation in dextran solution: dependence on polymer conformation," *European Biophysics Journal,* vol. 27, pp. 177-181, 1998.

[8]   O. K. Bakurt, M. Bor-Kucukatay, O. Yalcin and H. J. Meiselman, "Aggregation behavior and electrophoretic mobility of red blood cells in various mammalian species," *Biorheology,* vol. 37, pp. 417-428, 2000.

[9]   M. Kumaravel and M. Singh, "Sequential analysis of aggregation process of erythrocytes of human, buffalo, cow, horse, goat and rabbit," *Clinical Hemorheology and Microcirculation,* vol. 15, no. 3, pp. 291-304, 1995.

[10] O. K. Baskurt, R. A. Farley and H. J. Meiselman, "Erythrocyte aggregation tendency and cellular properties in horse, human and rat: a comparative study," *American Journal of Physiology,* vol. 273, pp. H2604-H2612, 1997.

[11] R. Lima, T. Ishikawa, Y. Imai and T. Yamaguchi, "Blood Flow Behavior in Microchannels: Past, Current and Future Trends," in *Single and Two-Phase Flows on Chemical and Biomedical Engineering*, Bentham Science, 2012, pp. 513-547.

[12] R. Fåhræus and T. Lindqvist, "The viscosity of the blood in narrow capillary tubes," *American Journal of Physiology,* vol. 96, no. 3, pp. 562-568, 1931.

[13] H. G. Hornung, Dimensional Analysis: Examples of the use of symmetry, Mineola, New York: Dover Publications, Inc., 2006.

[14] G. Segré and A. Silberberg, "Radial particle displacements in Poiseuille flow of suspensions," *Nature,* vol. 189, pp. 209-210, 1961.

[15] H. Amini, W. Lee and D. Di Carlo, "Inertial microfluidic physics," *Lab on a Chip,* vol. 14, pp. 2739-2761, 2014.

[16] G. Coupier, B. Kaoui, T. Podgorski and C. Misbah, "Noninertial lateral migration of vesicale in bounded Poiseuille flow," *Physics of Fluids,* vol. 20, no. 11, 2008.

24

[17] C. A. Stan, A. K. Ellerbee, L. Guglielmini, H. A. Stone and G. M. Whitesides, "The magnitude of lift forces acting on drops and bubbles in liquids flowing inside microchannels," *Lab on a Chip,* vol. 13, pp. 365-376, 2013.

[18] P. C.-H. Chan and L. G. Leal, "The motion of a deformable drop in a second-order fluid," *Journal of Fluid Mechanics,* vol. 92, no. 1, pp. 131-170, 1979.

[19] P. Olla, "The lift on a tank-treading ellipsoidal cell in a bounded shear flow," *Journal de Physique II,* vol. 7, no. 10, pp. 1533-1540, 1997.

[20] A. Kumar and M. D. Graham, "Mechanism of margination in confined flows of blood and other multicomponent suspensions," *Physical Review Letters,* vol. 109, 2012.

[21] P. A. Aarts, S. A. van den Broek, G. W. Prins, G. D. Kuiken, J. J. Sixma and R. M. Heethaar, "Blood platelets are concentrated near the wall and red blood cells in the center in flowing blood," *Arteriosclerosis, Thrombosis and Vascular Biology,* vol. 8, pp. 819-824, 1988.

[22] Y. C. Fung, Biodynamics: Circulation, Springer, 1984.

[23] C. G. Caro, T. J. Pedley, R. C. Schroter and W. A. Seed, The Mechanics of the Circulation, 2nd Edition, Cambridge University Press, 2011.

Chapter 3
Experimental Protocol

3.1   Experiment Overview

Measurements were performed with blood from four mammalian species (goat, sheep, pig, llama) and two oviparous vertebrates (chicken, turkey). Blood was prepared at five hematocrits (10, 20, 30, 40 and 50%). Pressure drop was measured in four types of tubing with nominal inner diameters ranging from 62.5μm to 152.4μm (Figure 1), with syringe pump driven flow. Flow rates ranged from tens to hundreds of microliters per hour depending on tubing diameter.

Pressure Transducers

PEEK Tubing
ID: 63.5 − 152.4μm
Length: 7 − 55cm

Blood
10-50% Hematocrit
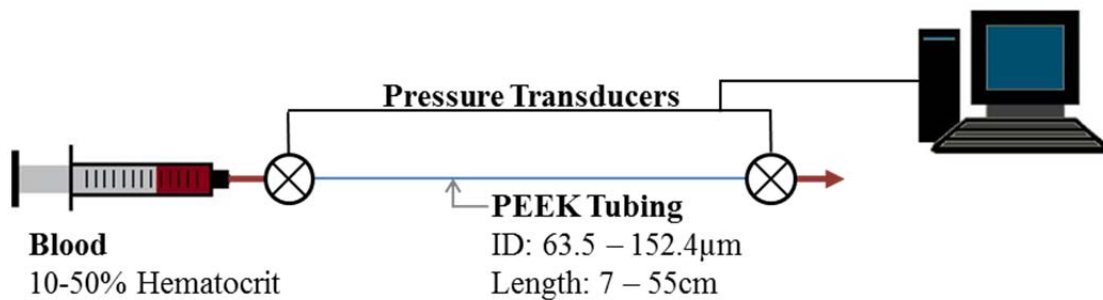
Figure 1. Schematic of experimental setup

Images of the red blood cells for each species are shown in Figure 2. These animals were selected to represent a range of red blood cell characteristics as well as availability from reputable laboratory suppliers. Goat erythrocytes are typically considered the smallest vertebrate red blood cells, with an average diameter of ~3μm [1]. In addition, goat erythrocytes have flat surfaces rather than the concavity seen in other mammalian cells, and irregularly shaped poikilocytes (Figure 2a) are common in clinically healthy animals [2]. In research labs using a substitute for non-human blood, sheep blood is a common choice. Sheep have biconcave, non-aggregating red blood cells with an average diameter of 4.4μm (Figure 2b). Pig blood (Figure 2c) was selected for its physiological
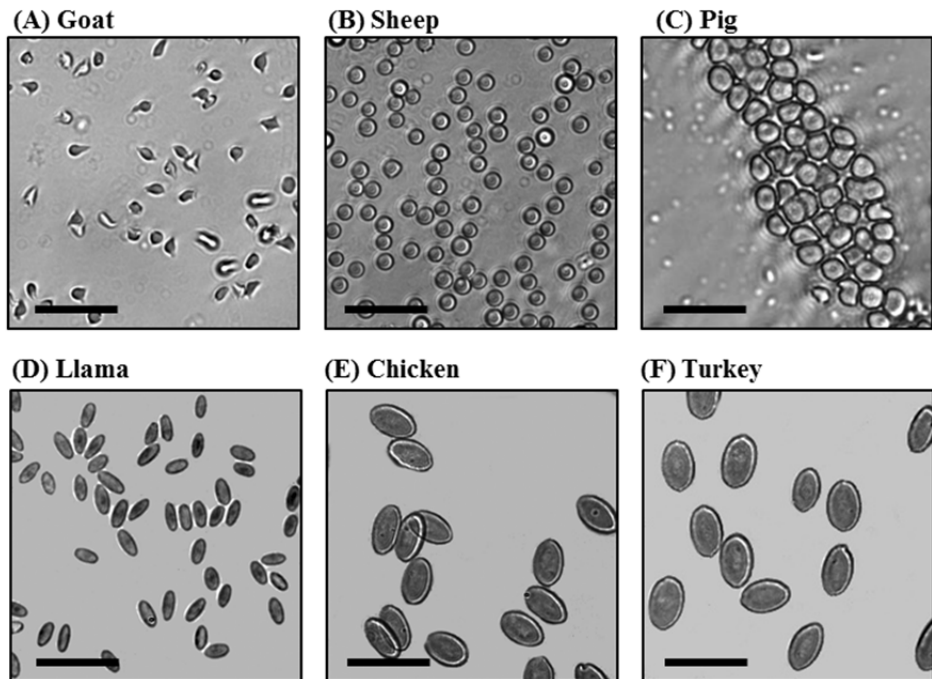
Figure 2. Optical micrographs of (A) goat, (B) sheep, (C) pig, (D) llama, (E) chicken and (F) turkey red blood cells. Scale bars: 20μm.

similarity to human blood, sharing a similar average diameter (7μm), biconcave shape, and aggregation tendency. Members of the Camelidae family such as alpacas, camels and llamas are unique among mammals as they have elliptocyte red blood cells, which are oval and flat rather than biconcave [2]. Llama red blood cells (Figure 2d) are 8μm by 3μm. Finally, two species with nucleated erythrocytes were included: chickens (12μm by 7μm) and turkeys (12μm by 8μm), as shown in Figure 2e and Figure 2f.

3.2   Sample Preparation

Whole blood and the corresponding homologous plasma for each blood type were obtained from Lampire Biological Laboratories.[1] Both whole blood and plasma included an anticoagulant at a ratio of 7.5:92.5 anticoagulant to blood/plasma. K_3-EDTA was selected as the anticoagulant based on its minimal impact to blood cell properties and flow characteristics [3]. Blood samples were shipped and stored at 4°C-8°C and used within 2 weeks of arrival. Plasma was shipped frozen. It was thawed and aliquoted into ~10ml volumes upon arrival, and refrozen for storage up to 5 years. One hour prior to sample preparation, an appropriate volume of plasma was allowed to thaw at room temperature. Thawed plasma being used within 4 days was stored at 4-8°C to avoid the negative effects of additional freeze/thaw cycles.

3.2.1 Hematocrit measurement

The blood sample was removed from the refrigerator and mixed by gentle inversion for 2-5 minutes or until solution was homogenized with no cells remaining on the bottom of the container. Two capillary tubes (Drummond Heparinized Capillary Tubes, Item #1-000-3200-H) were filled by placing one end in contact with the blood sample. The tubes were placed in the SpinCrit rotor hub in the loading position; once loaded, placing the SpinCrit hub in the run position effectively sealed both ends of the capillary tubes via gentle pressure against a rubber stopper (Figure 3). Tubes were centrifuged for 6.5 minutes (goat blood) or 5 minutes (all other blood types). Centrifugation times were determined by centrifuging samples for an initial 2.5 minute period, measuring the hematocrit, and centrifuging for additional 30 second intervals until the measured hematocrit was consistent across time intervals.
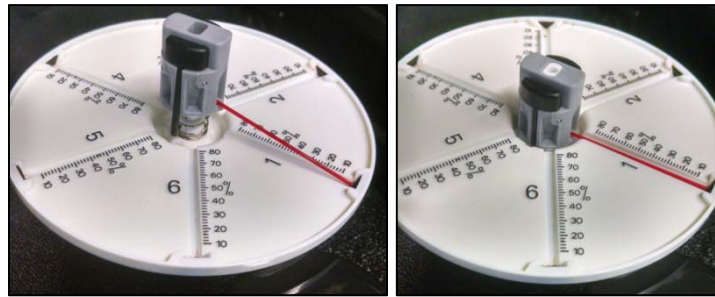
Figure 3: SpinCrit rotor in loading position (left) and run position (right)

To determine the volume fraction of red blood cells, or the hematocrit, of the sample, a centrifuged capillary tube was removed from the SpinCrit rotor and held under a magnifying lamp. Digital calipers with 0.01mm resolution were used to measure the length of the tube

---

[1] Unfiltered turkey plasma was not available from the supplier, so plasma for dilutions and plasma data collection was obtained by centrifuging whole turkey blood and collecting the plasma layer by Pasteur pipet.

ال‏منارة للاستشارات

www.manaraa.com

containing packed red blood cells (A) and the total length of the fluid in the tube (B) as shown in Figure 4. The percent hematocrit (Ø) was then found by:

$$\frac{A}{B} \times 100 = \emptyset \qquad (3.1)$$

A comparison of repeated measurements on the same tube by multiple individuals found that the determined values were consistent within ±0.03mm, translating to a hematocrit measurement error of ±0.001 (0.1%). The hematocrit measurement and calculation was repeated for the 2nd tube and the values averaged to determine the hematocrit of the sample blood.
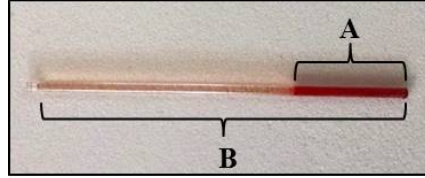
Figure 4: Capillary tube with whole
blood post-centrifugation

3.2.2 Dilution to a lower hematocrit

If the desired hematocrit ($\emptyset_{final}$) was less than the measured sample hematocrit ($\emptyset_{actual}$), the blood was diluted via the addition of homologous plasma. For an initial dilution, the following equation was used to calculate the required volume of sample blood ($V_{initial}$):

$$\frac{\emptyset_{final} V_{final}}{\emptyset_{actual}} = V_{initial} \qquad (3.2)$$

The required plasma volume (V_{plasma}) was then calculated by:

$$V_{final} - V_{initial} = V_{plasma} \qquad (3.3)$$

Dilutions were performed in a 2.0ml Eppendorf tube (V_{final} = 2.0ml). A micropipette was used to transfer the calculated volumes of $V_{initial}$ and V_{plasma} into a clean Eppendorf tube, which was then capped and inverted 15-20 times to thoroughly homogenize the blood. The hematocrit of this blood sample was measured in three capillary tubes using the previously described method.

3.2.3 Concentration to a higher hematocrit

If the desired hematocrit hematocrit ($\emptyset_{final}$) was greater than the measured sample hematocrit ($\emptyset_{actual}$), the sample was concentrated by centrifuging a predetermined volume of the sample blood ($V_{initial}$) – typically 2.0ml when using a 2.0ml Eppendorf tube. The tube was filled via micropipette and the sample spun in a Benchmark myFuge for 60 seconds or until enough blood cell sedimentation occurred to leave an appropriate volume of clear plasma at the top of the tube. A volume of plasma (V_{plasma}) was carefully removed by micropipette, avoiding any disruption of the red blood cells, as calculated by:

28

$$V_{initial} - \frac{\emptyset_{actual}V_{initial}}{\emptyset_{final}} = V_{plasma} \tag{3.4}$$

The tube was then recapped and inverted 15-20 times to thoroughly homogenize the blood. The hematocrit of this blood sample was measured in three capillary tubes using the previously described method.

3.2.4 Hematocrit parameters and further hematocrit adjustment

The hematocrit was considered acceptable if the average value from the three capillary tubes was ±1% of the target hematocrit, i.e. for a target hematocrit of 20%, an average value within the range of 19.00% to 21.00% was acceptable. If the hematocrit fell outside of the defined range, the hematocrit was further adjusted using the previously described methods. By considering the prepared sample volume (V_{final}) to be the new initial volume ($V_{initial}$), straightforward manipulation of equations 3.2 and 3.3 yields the following equation to dilute the sample by adding a volume of plasma (V_{plasma}) via micropipette:

$$\frac{\emptyset_{actual}V_{initial}}{\emptyset_{final}} - V_{initial} = V_{plasma} \tag{3.5}$$

After all prepared hematocrits were within an acceptable range, the original sample bottle of blood was returned to the refrigerator. The prepared blood in Eppendorf tubes was placed in a room temperature water bath and allowed to equilibrate to room temperature.

For each blood type (goat, sheep, pig, llama, chicken, turkey), data collection was performed for five hematocrits (10%, 20%, 30%, 40%, 50%) and plasma. A complete data run for a single hematocrit in each tubing length generally required 6-8ml of prepared blood. The complete volume for a single hematocrit was prepared at once in 4 Eppendorf tubes and preferably used the same day. However, the hematocrit was found to be stable for several days in sealed Eppendorf tubes stored at 4-8°C. The hematocrit of prepared blood used after the initial day was measured before use to confirm it remained within the acceptable range.

The supplier considers whole blood in K_3-EDTA to be stable for three weeks when stored at 4-8°C, and comparison of hematocrits on subsequent days of sample preparation showed little change in the original blood sample. However, to further minimize any impact of changes in red blood cells due to storage, the higher hematocrit samples were prepared and run first.

3.3   Data Collection Setup

Pressure drop measurements were performed in an experimental setup consisting of a syringe pump (Chemyx Fusion 200), narrow-gauge tubing, and two pressure transducers.

3.3.1 Pressure transducer signal amplification

Two pressure transducers were used to measure gage pressure at the tubing inlet and outlet. Both transducers were Honeywell 26PC miniature flow-through pressure transducers. The specifications of each transducer are listed in Table 1.

29

Table 1: Pressure transducer specifications

Catalog Number	Measurement Location	Type	Pressure Range	Sensitivity	Full Scale Span	Null Offset	Max Overpressure	Error (% span)
26PC6CF6G	Inlet	flow-through, vacuum gage	±15psi	6.67mV/psi	100mV	0 mV	45 psi	±1.0
26PCAFG6G	Outlet	flow-through, vacuum gage	±1psi	16.7mV/psi	50mV	0 mV	20 psi	±1.0

The millivolt output of the inlet pressure transducer (26PC6CF6G) was amplified with an Omega Model DMD-465 bridge amplifier. The wiring diagram for the transducer and DMD-465 is shown in Figure 5. The bridge excitation was set to 10.00V and the output offset to 0.00V. The inlet pressure transducer gain was set to 100. The gain and linearity were verified by sealing one end of the transducer flow-through port and applying a stable pressure via a syringe at the opposite port and measuring both the transducer output (mV) and signal conditioner output (V) at 55.3mV (5.53V) and 96.2mV (9.62V).
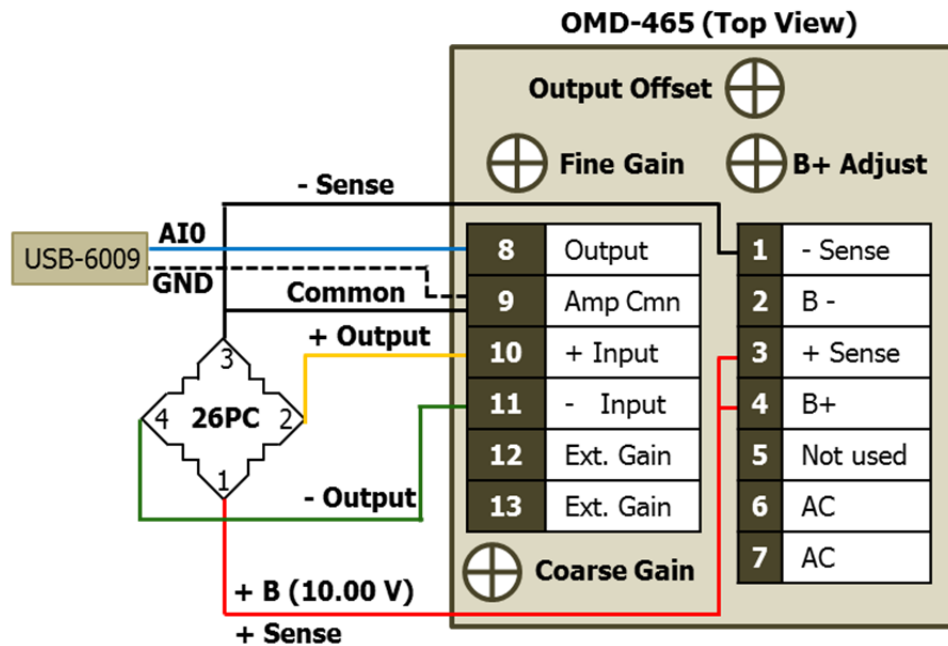
Figure 5. Wiring diagram for Omega Model DMD-465 bridge amplifier and 26PC6CF6G pressure transducer

The millivolt output of the outlet pressure transducer (26PCAFG6G) was amplified with a previously assembled system consisting of a strain gage signal conditioner (Omega OM2-161) mounted on a backplane (Omega OM2-8608). The wiring diagram for the transducer (26PC series) and signal conditioner is shown in Figure 6. The detailed calibration

30

procedure is available in Appendix A. With the bridge in zero condition, the gain for the outlet transducer was set at 100, based on a supply voltage of 5.00V with an output offset of 0.00V. The gain and linearity were verified by sealing one end of the transducer flow-through port and applying a stable pressure via a syringe at the opposite port and measuring both the transducer output (mV) and signal conditioner output (V) at 14.23mV (1.423V) and 15.45 mV (1.545V).

Prior to both calibration and use, the signal conditioners for both transducers were plugged in and allowed to warm up for at least one hour.
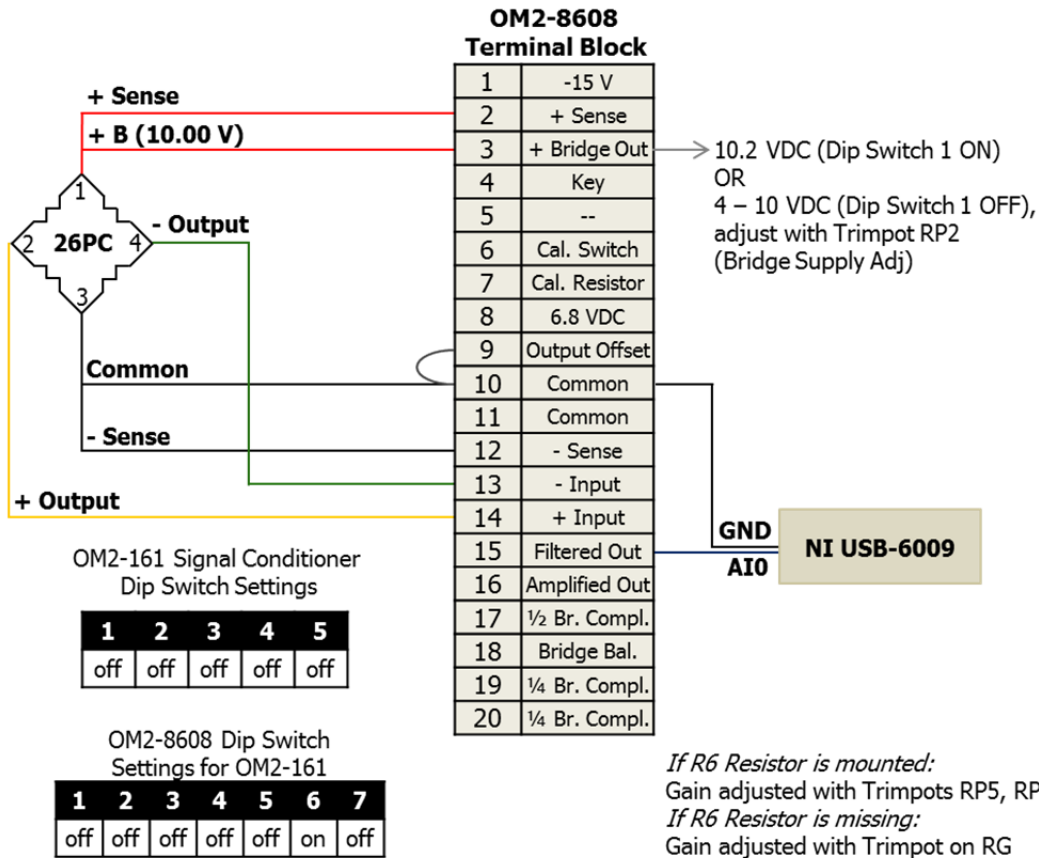
Figure 6. Wiring diagram for strain gage signal conditioner (Omega OM2-161) mounted on a backplane (Omega OM2-8608) with 26PCAFG6G pressure transducer.

3.3.2 Fluid path setup

Pressure drop of the blood flow was measured in polyetheretherketone (PEEK) polymer tubing manufactured by Upchurch Scientific and purchased from IDEX Health & Science. This tubing was selected based on its microscale inner diameters, capability of withstanding high pressure environments with no expansion of the inner channel, biocompatibility, flexibility, ability to trim lengths without specialized equipment, and very smooth internal surface. Four different tubing diameters were selected for initial experiments, each with an outer tubing diameter of 1/16", ensuring compatibility with pressure-tight HPLC fittings. Tubing lengths were designed to maximize use of the inlet pressure transducer range (15psi/103.4kPa) for a reasonable approximation of the viscosity of 40-50% hematocrit blood based on the Hagen-Poiseuille Equation. Tubing parameters are listed in Table 2.

Table 2. PEEK tubing parameters

Product #	Inner Diameter (μm)	Inner Diameter (in)	Tolerance (±μm)	Length (cm)
1560	63.5	0.0025	12.7	7.0
1561	101.6	0.004	12.7	25.0
1535	127	0.005	12.7	40.0
1562	152.4	0.006	12.7	55.0

The inlet and outlet pressure transducers were connected to the PEEK tubing through the use of Upchurch Scientific PEEK unions and fittings with ferrules (Figure 7). In order to firmly mate the barbed connectors of the pressure transducers with the barbed threaded union fittings, a small length of Tyvek tubing was used to mate the two barbs and avoid exposure of the fluid path to the flexible Tyvek tubing. The flow was driven by a Fusion 200 syringe pump with either a glass 100μl Hamilton Gastight syringe (#1560, 1561, 1535 tubing) or a glass 1.0ml Hamilton Gastight syringe (#1562 tubing).

Figure 7. Experimental flow path

Room temperature was monitored through the use of two K-type thermocouples attached to a digital thermocouple reader. Thermocouples were attached to the tubing adjacent to the inlet and outlet pressure transducers. Observed values were entered into the LabVIEW program. Daytime room temperature fluctuations were minimal, with a typical range of 23.0°C ± 0.8°C.

3.3.3 Data collection software

Data was collected via a National Instruments NI-6009 USB data acquisition module and a National Instruments Labview code (PressureTempMeasure_Omega.vi).

Collected files were named according to the format in Table 3 both for recordkeeping purposes and automated data input in Matlab (see Chapter 5). The LabVIEW program automatically inserts the date and the first underscore, so only the non-italicized parts need to be entered in the filename field. Hyphens replace periods in the tubing diameter. The first trial of each run does not require a number designation. The second row shows the correlating filename input and the third row in Table 3 indicates the resulting filename.

Table 3. Naming system for data files

YYYY.MM..DD_	animal	hct _	tube diam _	tube length _	flow rate (ulhr)	trial#	.txt
2015.06.03_	sheep	20_	101-6_	7cm_	100ulhr	2	.txt
2015.060.03_llama30_63-5um_7cm_100ulhr2.txt.txt							

32

The LabVIEW program front panel is shown in Figure 8. When first opening the program, the sample rate is set to 20Hz, and the appropriate transducers (15psi and 1psi) were selected from the dropdown menu. Inlet Temp and Outlet Temp were updated each time the thermocouple temperature changed. The hematocrit was entered for each sample. The filename was updated for each sample, tubing diameter, flow rate and trial number. With the code running, the voltages for the inlet pressure transducer, outlet pressure transducer and force sensor were plotted on the chart. Clicking "Collecting Data" began data collection, with the pressure and force values displayed in kilopascals, pounds per square inch, and Newtons, respectively. Clicking "Stop/Save" ended data recording and brought up a "Save As" menu, generating the filename from the Labview code and entered text.
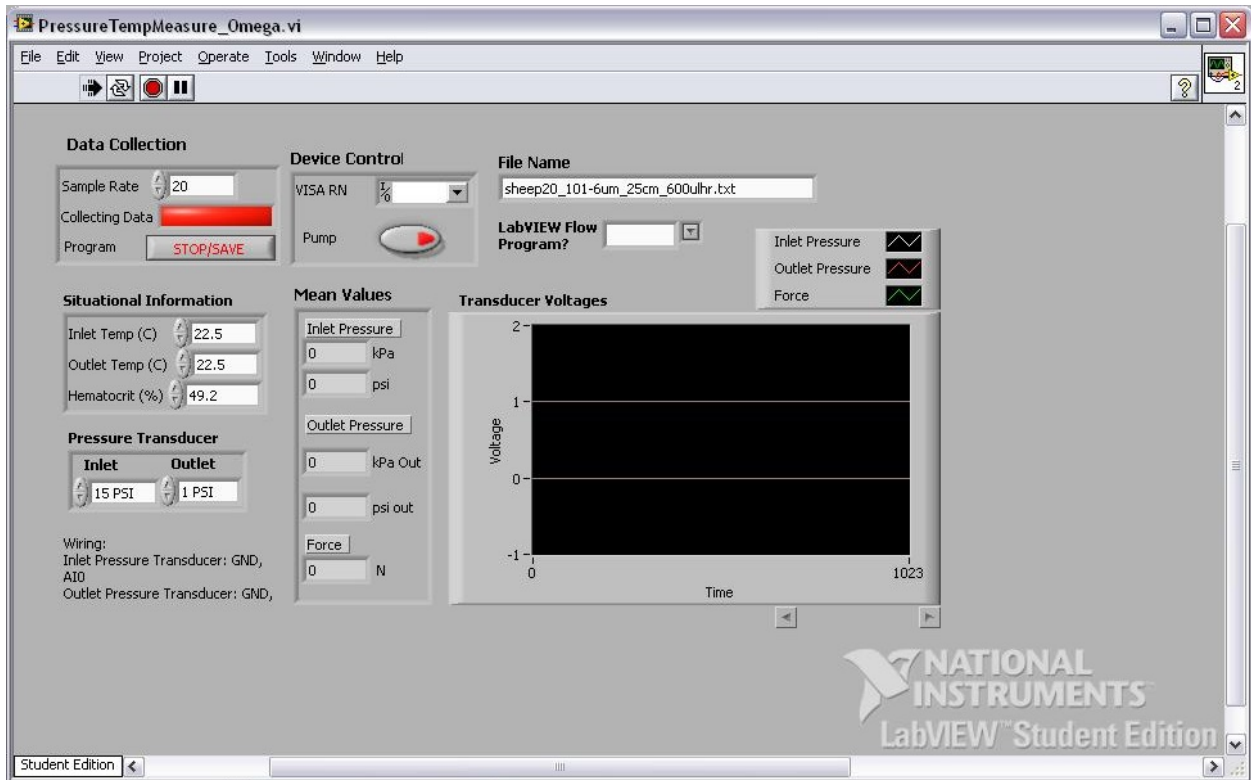
Figure 8. LabVIEW program front panel

The text files consisted of three columns of data. In the first row, columns one and two were the inlet and outlet temperatures in °C. The third entry in the first row was the percent hematocrit. The remaining rows consisted of paired sets of inlet and outlet pressure data and force measurements. The first column was inlet pressure data in kPa, the second column was outlet pressure data in kPa and the third was force data in Newtons.

3.4   Data Collection Protocol
One hour prior to data collection, the syringe, fittings and PEEK tubing were filled with fresh 1.0% Bovine Serum Albumin (BSA) solution to minimize potential cellular adhesion to the walls of the tubing and fittings [4], and the transducer amplifiers were connected to the building power supply. Any tubes of blood acquired from the fridge were placed in a room-temperature water bath for one hour to equilibrate to room temperature.

33

To commence data collection, the appropriate data was entered into the LabVIEW program and the program was set to run in order to monitor the tubing pressures while loading blood into the system. The BSA was flushed from the tubing and syringe with phosphate-buffered saline solution (PBS). The Eppendorf tube of blood was thoroughly mixed by inverting it 15-20 times.

For blood flow in the #1560, #1561 and #1535 tubing (64.5μm, 101.6μm and 127μm nominal diameters, respectively), the fluid path was filled with blood from the Eppendorf tube prior to connecting the glass syringe, as the glass syringe itself was not large enough to prime the system. First, a 1ml disposable syringe was filled to ~0.75 ml with the homogenized blood. This syringe was used to completely fill the fluid path of the outlet pressure transducer and associated fittings. Next, it was attached to the fluid inlet and the inlet transducer and connected fittings were filled. With the syringe still attached to the inlet luer-slip fitting, the appropriate PEEK tube was placed in the union and the fitting tightened. It is important that fitting be loose when the tube is first inserted, as the end of the tube will extend past the end of the fitting and be in contact with the union bore. Slight pressure was then applied to the syringe until the tube was completely filled with blood. The free end of the tube was then attached to the outlet transducer fittings and the plastic syringe removed from the inlet. To avoid introducing bubbles into the system when attaching the glass syringe, the inlet luer-lock fitting was completely filled with blood either by gently depressing the syringe plunger as the plastic syringe was removed from the outlet or by manually filling it with a syringe and needle. The glass syringe was then filled to maximum capacity (100μl) with the sample blood and attached to the inlet, while ensuring that the luer-lock syringe and fitting were completely tightened. The syringe was seated in the syringe pump and the appropriate syringe diameter and flow rate settings verified.

For blood flow in the #1562 (152.4μm diameter) tubing, the larger 1.0ml glass syringe holds enough volume for the initial priming of the system as well as data collection. Therefore, the previous steps require only the glass syringe, eliminating the potential for bubbles arising from attaching and reattaching syringes at the inlet.

The flow rate range used depended on the tubing diameter; ranges were selected to correspond to *in vivo* blood cell velocities of 0-35mm/sec in arterioles of similar diameter [5]. The flow rates are listed in Table 4.

Table 4. Flow rates in μl/hr for each tubing diameter

#1560 (Ø 63.5μm)	#1561 (Ø 101.6μm)	#1535 (Ø 127μm)	#1562 (Ø 152.4μm)
10	10		
25	25	25	
50	50	50	
100	100	100	
200	200	200	
300	300	300	
400	400	400	
500	500	500	500
600	600	600	750
	700	700	1000
	800	800	1250
	900	900	1500
	1000	1000	

34

Flow was started as soon as the syringe was loaded to avoid red blood cell sedimentation. Higher flow rates were measured first to minimize cell aggregation and sedimentation. For #1560 tubing, flows began at 600 μl/hr and were stepped down to 10 μl/hr. The initial data collection for each blood sample in #1561 and #1535 tubing began at 600 μl/hr, stepped upwards to 1000 μl/hr, and then proceeded from 500 μl/hr to 10 or 25 μl/hr. This progression was to evaluate whether the high flow rates would exceed the pressure transducer maximum; if the higher flow rate readings were within acceptable limits, the second and third data runs were started at 1000 μl/hr and proceeded through the slower flow rates to 10 or 25 μl/hr. Analysis of average values recorded in the lab notebook and later of the data itself showed no difference in the measured values for flow beginning at 600 μl/hr or 1000 μl/hr. For #1562 tubing, flow began at 1500 μl/hr and ended at 500 μl/hr.

At each flow rate, the flow was allowed to reach a steady state as determined by observation of the inlet transducer voltage in the LabVIEW chart. The time to reach steady state varied based on the tubing diameter, blood type and hematocrit, but was generally at least 30 seconds for start-up flow and 20 seconds to 2 minutes for changing between flow rates. Changes in low flow rates (10-100μl/hr) required the most time to equilibrate. Flow in #1562 tubing was also given additional time to equilibrate, with a 60 second minimum.

Occasionally the observed transducer voltages failed to equilibrate and would vary in sinusoidal fashion over a small range of voltages; these fluctuations were given additional time to equilibrate, and if they did not, the data recording period was extended. Subsequent analysis of mean pressure values for oscillating versus steady runs of the same tubing, flow rate and blood type yielded comparable average pressure drop values.

After reaching steady state, data collection was started via the LabVIEW program. At least 500 data points were collected (25 seconds at 20Hz), with times extended for fluctuating data and for flow in #1562 tubing (minimum of 2 minutes per flow rate). The average inlet pressure value was also recorded in a lab notebook for general reference. After this time, selecting "Stop/Save" halted data collection. The flow rate was adjusted to the next value, and then the file was saved. The flow rate was updated in the LabVIEW interface and the program was set to run again. This was repeated for all flow rates, and then for the system with no flow, completing one data set.

After each data set, the glass syringe was removed to be refilled. The fitting at the inlet of the PEEK tubing was loosened, and 0.3-0.5ml of newly homogenized blood were flushed through the inlet to remove any bubbles or cellular aggregates. The inlet fitting was then retightened, the glass syringe refilled and reattached, and the data collection process was repeated two more times for a total of three data sets per combination of tubing diameter, blood type and percent hematocrit.

When changing to a new tubing diameter for the same blood type and hematocrit, the original PEEK tubing was removed and immediately thoroughly flushed with PBS and air via a syringe and HPLC fitting. The new tubing was then fitted to the inlet and filled with blood, then connected to the tubing outlet.

The inlet and outlet pressure transducers were attached to lab stands to facilitate rearrangement for differing tubing lengths. The lab stands were positioned to minimize bends in the tubing and to keep the transducers at equal heights.

Upon completion of data collection for the day, the system was partially disassembled and cleaned. First the PEEK tubing in use was removed and cleaned as previously described. The HPLC fittings were removed from the transducer flow paths and allowed to soak in PBS while

additional cleaning took place. The glass syringe was also briefly flushed and allowed to soak in PBS during this time. Through the use of plastic syringes, the inlet and outlet transducers and connecting tubing were flushed thoroughly first with PBS, then 70% ethanol, and finally DI water. The HPLC fittings were then removed from the PBS solution and rinsed with 70% ethanol and DI water; the glass syringe was cleaned through the same process. Finally, the working area and the syringe pump were disinfected with 70% ethanol.

Works Cited:

[1] T. M. Amin and J. A. Sirs, "The blood rheology of man and various animal species," *Quarterly Journal of Experimental Physiology,* vol. 70, pp. 37-49, 1985.

[2] J. W. Harvey, Atlas of Veterinary Hematology, Philadelphia: W.B. Saunders Company, 2001.

[3] O. K. Baskurt, M. Boynard, G. C. Cokelet, P. Connes, B. M. Cooke, S. Forconi, F. Liao, M. R. Hardeman, F. Jung, H. J. Meiselman, G. Nash, N. Nemeth, B. Neu, B. Sandhagen, S. Shin, G. Thurston and J. L. Wautier, "New Guidelines for Hemorheological Laboratory Techniques," *Clinical Hemorheology and Microcirculation,* vol. 42, no. 2, pp. 75-97, 2009.

[4] Y. Nahmias and S. Bhatia, Microdevices in Biology and Medicine, Norwood: Artech House, 2009.

[5] Y. C. Fung, Biomechanics: Circulation, New York: Springer-Verlag, 1997.

Chapter 4
System Validation

The ability of the experimental system to accurately measure corresponding flow rate and pressure drop, and therefore solution viscosity, was validated by analysis and comparison of a numerical flow system and experimental data collected for solutions of known viscosity – water, 20% w/w glycerol and 40% w/w glycerol. The numerical simulation was first used to determine what, if any, corrections needed to be made to account for the changes in geometry upstream of the narrow tubing inlet. After making these corrections, the experimental results were analyzed to determine the actual tubing diameters used in the experiment, within the specified manufacturing tolerance range. Finally, the simulation geometry was updated to the calculated tubing diameters, and the simulation and experimental results were compared to validate the system.

4.1 Numerical Simulation of Experimental Setup
4.1.1 Simulation geometry and theoretical calculations

The flow path from the Wheatstone bridge of the inlet pressure transducer to the tubing outlet includes the small-diameter PEEK tubing as well as several millimeters of flow through the connecting fittings and the pressure transducer itself. For an incompressible Newtonian fluid, the Hagen-Poiseuille equation (4.1) describes the pressure drop (ΔP) through a long cylindrical vessel of length L, constant diameter (d) based on flow rate (Q) and dynamic viscosity (μ):

$$\Delta P = \frac{128\mu LQ}{\pi d^4} \tag{4.1}$$

The fluid path from the position of the silicon sensor inside the pressure transducer to the outlet of the downstream barb of the fluid connector is 12.5mm long and 1.0mm in diameter. This outlet is flush with the inlet of tubing adapter (Upchurch Scientific P-663, 1/16" tubing barb to 10-32 thread) with a length of 21.75mm and a 1.0mm diameter thru hole. This adapter is threaded to the union assembly (Upchurch P-760, 10-32 threading) with a 1.30mm diameter, 1.0mm long bore separating the adapter and the PEEK tubing inlet. The relative pressure drops for an arbitrary Newtonian fluid in the inlet section and within the PEEK tubing are listed in Table 1.

Table 1. Pressure drop (ΔP) calculated for a fluid of arbitrary viscosity (μ) and flow rate (Q) for the upstream (inlet) sections and PEEK tubing sections of the flow path

Length (mm)	Diameter (mm)	ΔP (*π/128μQ)	ΔP_{tube}/ΔP_{inlet}
34.25 (inlet)	1.0	34.25	-
1 (inlet bore)	1.27	0.384	-
70	0.0635	4,305,297	124,307
250	0.1016	2,346,201	67,742
400	0.127	1,537,606	44,395
550	0.1524	1,019,584	29,438

Given that the pressure drop in the PEEK tubing section of the flow path is ~30,000 to 125,000 times larger than the pressure drop imparted by the inlet section, this upstream section of flow can be considered negligible for future calculations.

In addition to the length added by the inlet portion of the flow, there is an abrupt contraction at the PEEK tubing inlet. At this point, the diameter of the flow path decreases by a factor of 6-13, depending on the diameter of the PEEK tubing. For pipe flow, a sudden contraction imparts head loss based on the ratio of the vessel diameter upstream and downstream of the contraction. The contraction results in the formation of vena contracta downstream of the contraction, where the cross-sectional area of the streamlines is at a minimum and less than that of the small vessel diameter (Figure 1). The flow after the vena contracta expands similar to flow after an abrupt enlargement, and it is this expansion which imparts additional head loss rather than the contraction itself. However, this is a turbulent effect, and although there is an observed decreased in the transition Reynolds number for microscale flow [1, 2], the reported values are still far above the maximum Reynolds number in this experiment.
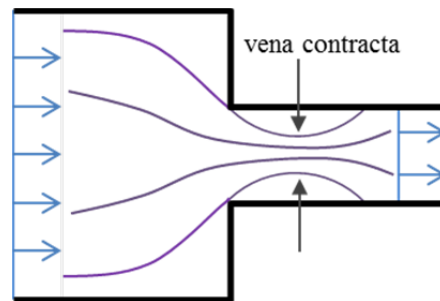

Figure 1. High Reynolds number flow through a sudden contraction

There have been some attempts to determine the effect of flow through a sudden contraction for low Reynolds number flow in microscale channels [3, 4, 5], but there is still disagreement as to the relative size and importance of this effect. Therefore, rather than using a potentially erroneous calculation to compensate for the additional pressure drop at the contraction, a computation model of the flow feature was developed in Comsol Multiphysics.

Based on the simplicity and symmetry of the flow path, a one-dimensional axisymmetric model was used, as shown in Figure 2. The simulation was based on the 63.5μm diameter PEEK tubing at the maximum experimental flow rate of 600μl/hr to determine the maximum effect from the contraction flow.
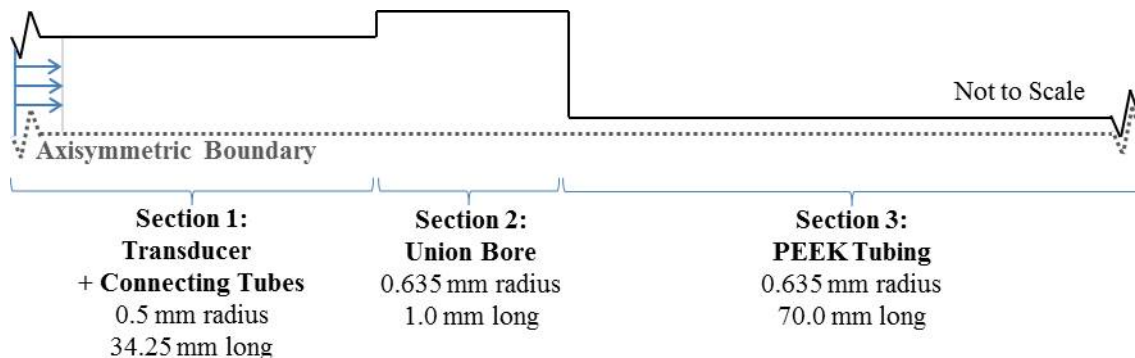

Figure 2. Schematic of Comsol geometry (not to scale)

38

4.1.2 *Determination of physical constants for numerical simulation*

The experiments using water and aqueous glycerol solutions took place at temperatures of 22.7-23.0°C. The dynamic viscosities of both water and glycerol are strongly temperature-dependent, so the viscosity and density values used for the Comsol model were selected to reflect an experimental temperature of 23.0°C. The literature values of water at this temperature were used in the model. The dynamic viscosity of aqueous glycerol solutions is available in the literature at discrete values at 10°C intervals, and the relationship between temperature and viscosity is nonlinear. Several groups have developed equations describing this relationship, but the calculated viscosities vary ±5% at a given temperature compared to other equations and reported values. Given this range and the degree of temperature variance inherent to the given experiment, the accepted standardized temperature/viscosity values were plotted (Figure 3a). The dynamic viscosities at 23.0°C for 20% w/w glycerol and 40% w/w glycerol were calculated via linear interpolation between the 20°C and 30°C literature values, and the results plotted in Figure 3b.
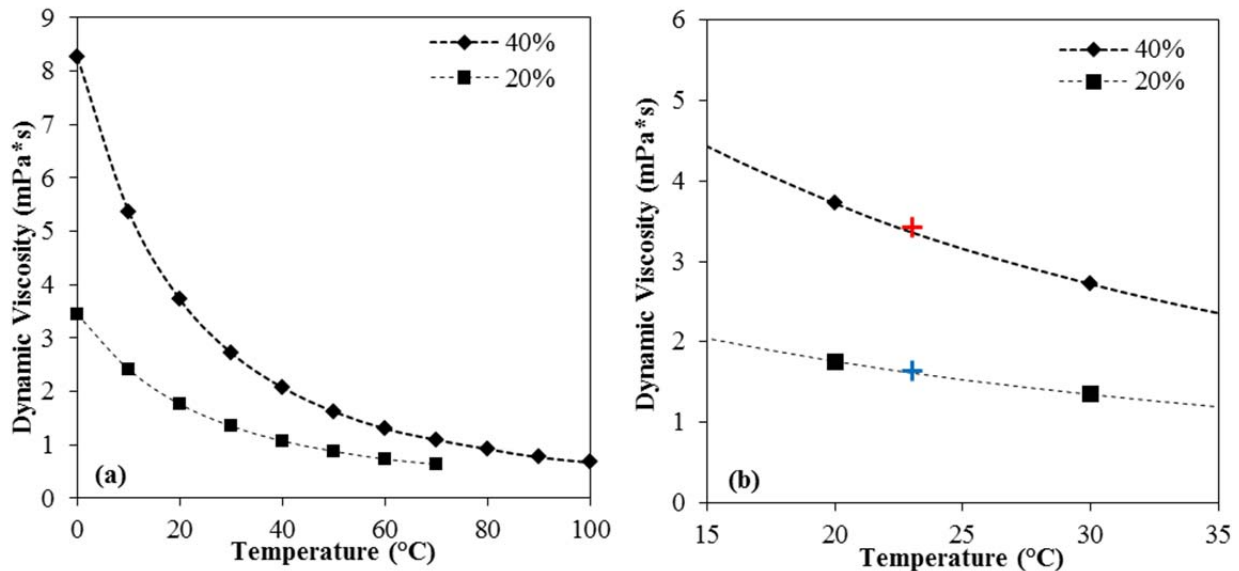

Figure 3. (a) Dynamic viscosity of 20%, 30% and 40% w/w aqueous glycerol solutions versus temperature [6] and (b) the same values with the values for 20% w/w glycerol (+) and 40% w/w glycerol (+) at 23.0°C as calculated by linear interpolation.

The plot indicates that although the values derived by linear interpolation are not completely accurate, they are quite close to the expected values. Given the other sources of experimental error and the simplifications made in the finite element model, these interpolated values were used as the reference viscosity values in the Comsol simulation. All reference values are listed in Table 2.

Table 2. Density and viscosity values used in Comsol simulation

Liquid	Density (g/ml) @ 23.0°C	Dynamic Viscosity (mPa*s) @ 23.0°C
Water	0.99754	0.932
20% w/w Glycerol	1.04591	1.637
40% w/w Glycerol	1.09798	3.420

39

The density of water and aqueous glycerol solutions is very nearly linear with respect to temperature in the region of interest, as shown in Figure 4. Linear interpolation between 20°C and 30°C was used to determine the density of the aqueous glycerol solutions for the simulation.
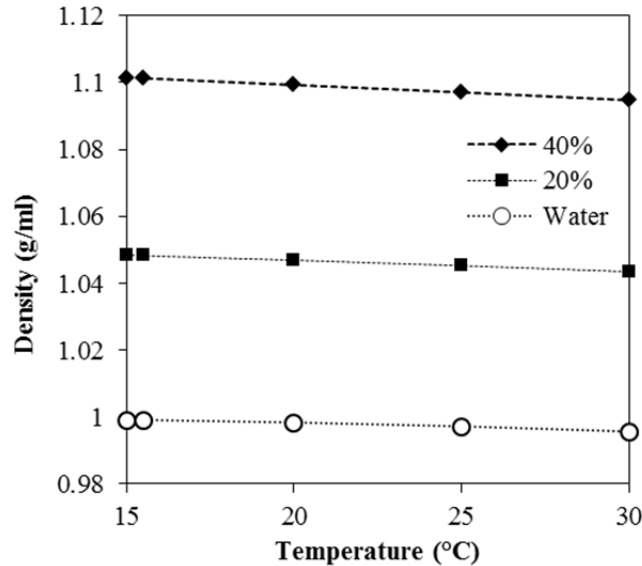

Figure 4. Density of water and aqueous glycerol solutions as a function of temperature.

4.1.3 Simulation results

A visualization of how the velocity changes in the transition through the bore into the PEEK tubing is shown in Figure 5. Qualitatively, this indicates regions of high shear in the final ~0.5mm upstream of the PEEK tubing inlet as the streamlines converge and flow accelerates into the smaller cross-section area. The Figure 5 inset provides a more detailed view at the tubing inlet; note that no vena contracta is present in this region.
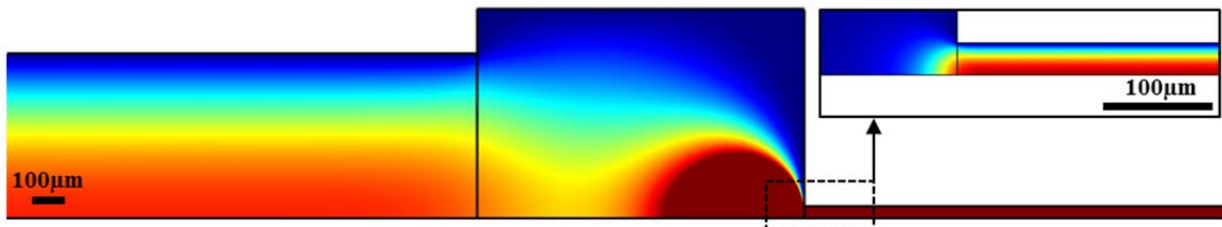
Figure 5. 2D velocity plot at inlet to PEEK tubing with detailed inset.

The simulation pressure results are plotted in Figure 7, with a blue bar indicating the PEEK tubing inlet at a z-position of 35.25 millimeters.

A more detailed graph view from the flow into the tubing inlet is presented in Figure 6. The deflection in pressure begins just upstream of the PEEK tubing inlet, follows a smooth decrease, and eventually follows a linear trend in the region of the PEEK tubing itself.

40
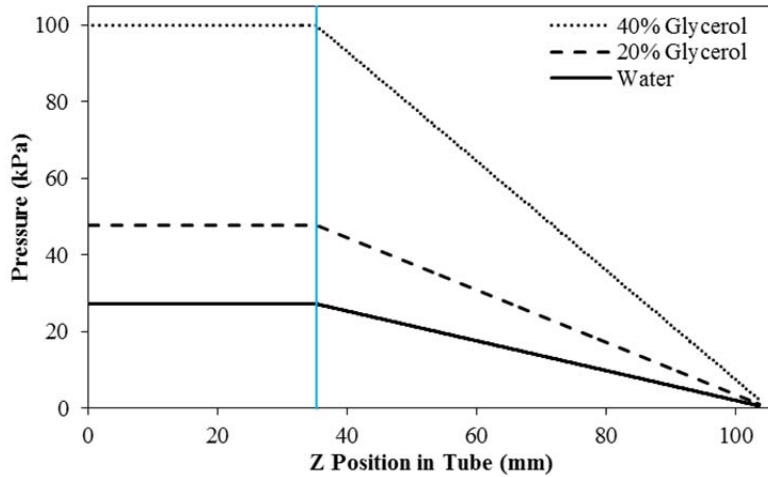
Figure 7. Plot from numerical simulation of pressure versus downstream position in tubing. Blue bar indicates the tubing inlet at Z = 35.25mm.

The pressure gradient with respect to z-position was also calculated in Comsol; the results are presented in Figure 8. As with the pressure versus position graphs, these charts indicate three primary regions of flow. The pressure gradient, or pressure drop per unit length, in the pressure transducer and tubing connections is steady and nearly zero. Pressure gradient changes significantly at the PEEK tubing inlet, and finally reaches a new steady state within the tubing.
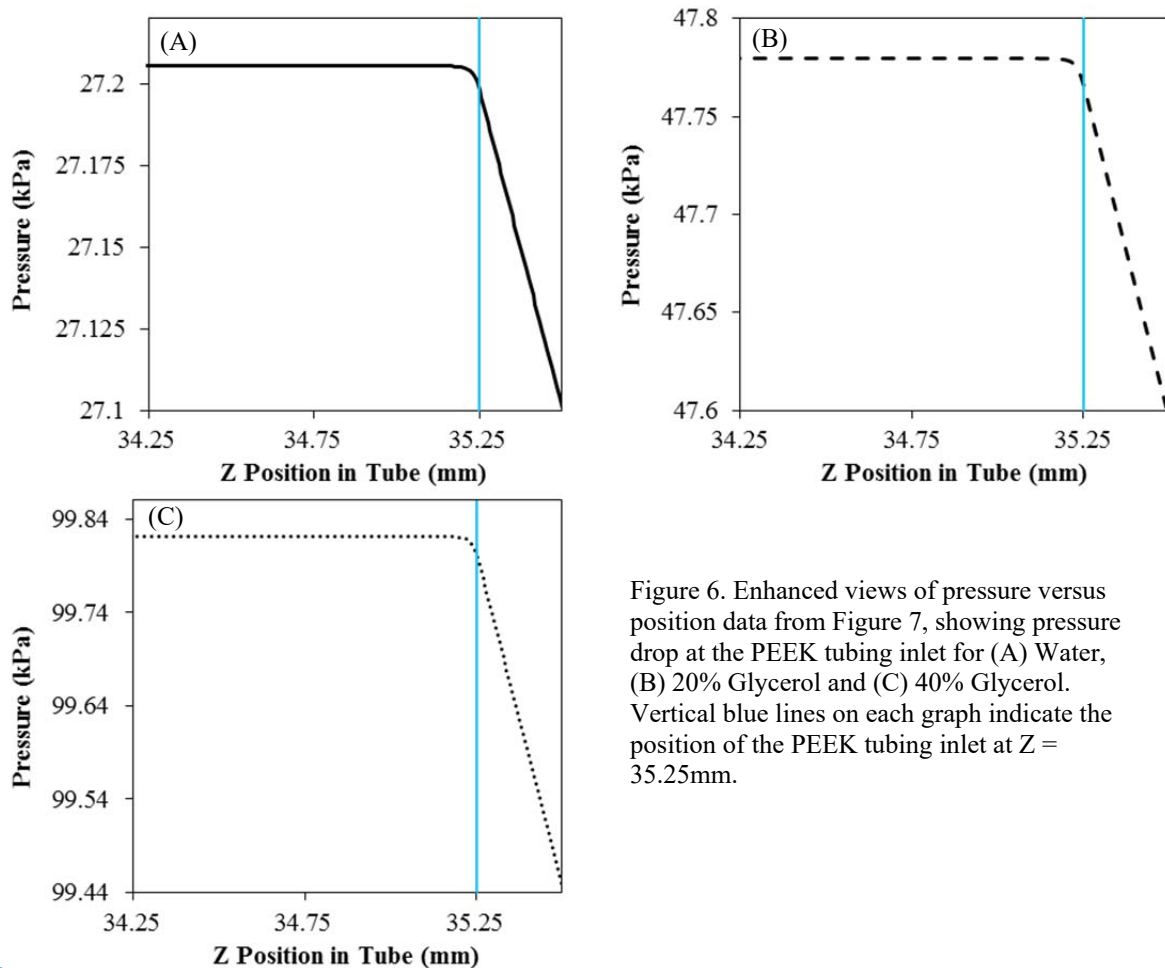
Figure 6. Enhanced views of pressure versus position data from Figure 7, showing pressure drop at the PEEK tubing inlet for (A) Water, (B) 20% Glycerol and (C) 40% Glycerol. Vertical blue lines on each graph indicate the position of the PEEK tubing inlet at Z = 35.25mm.

41

Figure 8. Pressure gradient with respect to z-position.

The pressure gradient values in the inlet region and the PEEK tubing region are listed in Table 3. Note that the flow in the PEEK tubing is fully developed within 120μm – less than two channel diameters – of the tubing inlet (Water: 72.84μm, 20% Gl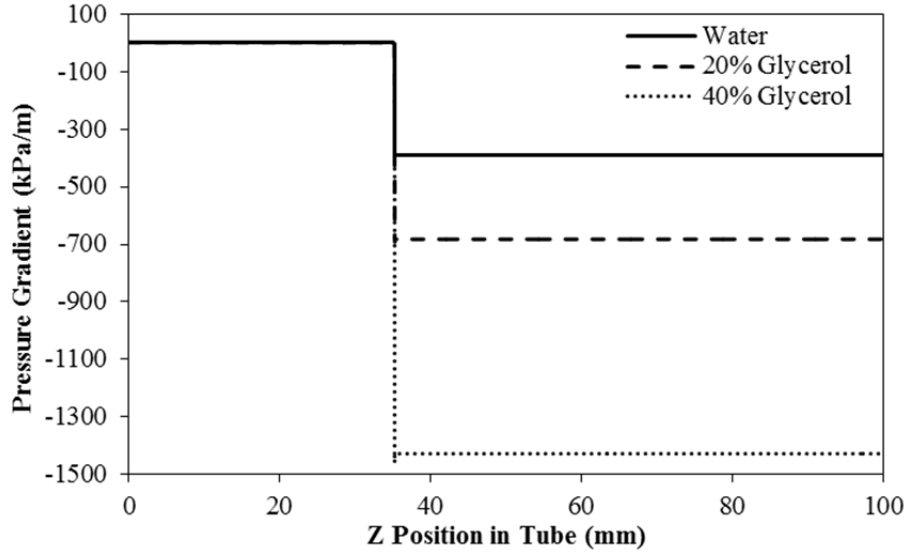ycerol: 113.67μm, 40% Glycerol: 107.7μm). Flow perturbation imparted by the PEEK tubing outlet spans a length of roughly the same size (Water: 109.9μm, 20% Glycerol: 128.3μm, 40% Glycerol: 92.42μm).

Table 3. Comsol simulation values

Liquid	Section 1&2 (Transducer + Connectors)		Section 3 (PEEK Tubing)	
	Pressure Gradient (Pa/m)	Z-Position Range (mm)	Pressure Gradient (Pa/m)	Z-Position Range (mm)
Water	-6.317	1.286 – 33.26452	-388559	35.32284 – 105.1401
20% Glycerol	-11.095	1.286 - 33.26452	-682407	35.36367 – 105.1217
40% Glycerol	-23.1803	1.597 – 33.04115	-1425687	35.35770 – 105.15758

More importantly, these results can be used to investigate the two "irregularities" in the flow path: the additional flow path length within the transducer and upstream tubing, and the impact of the abrupt contraction into the PEEK tubing. If the flow through the contraction is momentarily disregarded, the pressure drop in the inlet regimes (Sections 1 and 2) and the PEEK tubing can be compared, as in the theoretical calculations of Table 1. The results are presented in Table 4, and show that pressure drop in the PEEK tubing is over 3,600 times larger than that in the rest of the system.

Table 4. Comparison of pressure drop in inlet sections and in the PEEK tubing in the Comsol model

Flow Section	Water ΔP (Pa)	20% Glycerol ΔP (Pa)	40% Glycerol ΔP (Pa)
1 (Transducer)	0.214	0.376	0.794
2 (Inlet Bore)	7.311	12.841	26.803
3 (PEEK tubing)	27205.607	47779.830	99821.778
$\Delta P_3/(\Delta P_1 + \Delta P_2)$	3615	3615	3617
Contraction	35.561	90.316	180.177
$\Delta P_3/(\Delta P_{contraction})$	765	529	554

42

The most noticeable change in the pressure and pressure gradient graphs is, as expected, at the entrance to the PEEK tubing. In this region, the shear rate and average velocity are increasing substantially as the flow enters the much smaller diameter tube; the streamlines converge into a cross-sectional area ~1/400th the initial size. The flow quickly reaches steady state within the PEEK tubing, but this entrance length also imparts an additional pressure drop. The pressure drop caused by these features is considered to be the length of the model between the steady state pressure gradients in the inlet sections and the PEEK tubing, the corresponding Z-values for which are listed in Table 3. The total pressure drop in this transition region is 35.561 Pa for water, 90.316 Pa for 20% w/w glycerol and 180.177 Pa for 40% w/w glycerol (Table 4). As with the pressure drop in upstream tubing sections, these values are negligible (<1/500th) in comparison to the actual tubing pressure drop.

4.1.4 Conclusions

The simulation demonstrates that there is additional pressure drop imparted both by the length of larger diameter tubing leading from the transducer to the PEEK tubing and by the flow into the contraction at the PEEK tubing inlet. The pressure drop within the PEEK tubing is larger than that in the upstream tubing by a factor of more than 3,600, and can therefore be considered negligible. The flow through the contraction has a larger contribution to the overall pressure drop, but is still smaller than the pressure drop within the PEEK tubing by a factor of 500 to 700. This translates to 0.2% of the span, which is far less than the experimental error. Therefore, the minor effects of the contraction flow can be neglected when evaluating experimental data.

4.2 Data Collection with Newtonian Solutions of Known Viscosity

4.2.1 Experimental setup

Experiments for all tubing sizes and flow rates using the previously described protocol (Chapter 3) were conducted using three liquids of known density and viscosity. These results were used to validate the ability of the pressure drop tubing system to accurately measure pressure drop and ultimately solution viscosity. The selected liquids were deionized water, 20% w/w glycerol and 40% w/w glycerol. Aqueous glycerol solutions were selected due to their use as calibration standards for viscometers and their well-characterized properties at a range of temperatures and dilutions. The viscosity range from DI water to 40% w/w glycerol spanned the range of expected viscosities from the blood flow data. Experiments were conducted at a measured room temperature of 22.7°C – 23.0°C. Glycerol solutions were prepared fresh on the day of use, using a lab scale to mix the appropriate amounts of glycerol and water in a 2.0mL microcentrifuge tube. Measured weights were accurate to 0.001g.

The three data sets collected for each fluid/tubing/flow rate combination were averaged to determine a pressure drop per unit length for each data set. The Hagen-Poiseuille equation (4.1) was used to calculate three effective viscosities for each flow rate based on PEEK tubing with the maximum possible diameter (nominal diameter + tolerance), the nominal diameter, the minimum diameter (nominal diameter – tolerance) and the theoretical viscosity. These values, as well as the theoretical viscosities determined in section 4.1.2, were plotted for each flow rate and fluid. The results are presented below.

4.2.2 Experimental results: #1560 tubing

The results for #1560 tubing, with a nominal diameter of 63.5µm, are presented in Figure 9. The viscosity values are, of course, significantly different for each working fluid. The critical observation is that, regardless of fluid, the expected viscosity falls both within the range of possible viscosity values based on diameter tolerance and also at very nearly the same place in the diameter range for each example. This strongly indicates that deviation in calculated viscosity can be attributed to the actual tubing diameter differing from the nominal value.
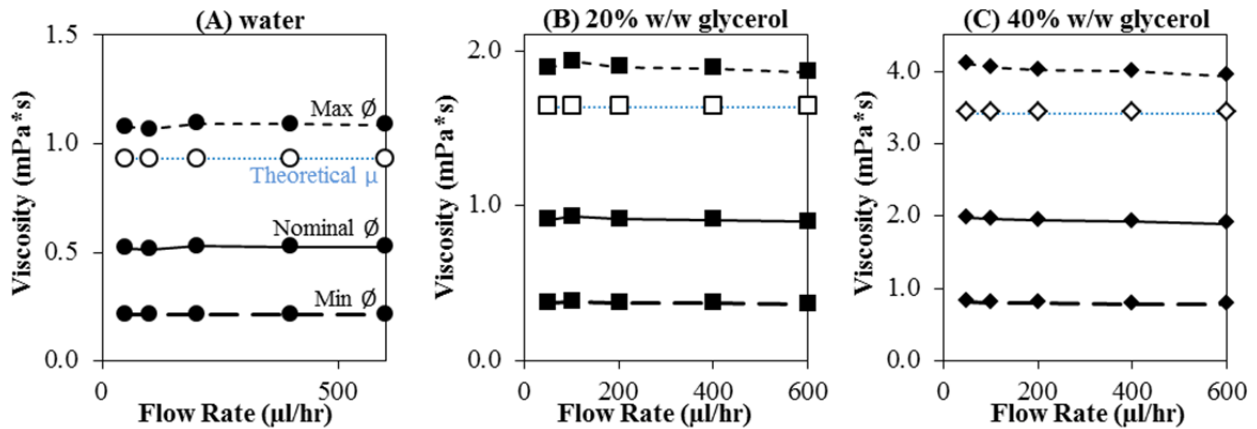
Figure 9. Experimental viscosity in #1560 tubing calculated for maximum diameter (**- - -**), nominal diameter (**——**), minimum diameter (**— —**) and compared to the theoretical viscosity (**·····**) for (A) water, (B) 20% w/w glycerol and (C) 40% w/w glycerol. Error bars are not included for experimental data as they are quite small – on the order of 0.01 mPa*s, or 1% of the mean viscosity for each data point.

Based on this conclusion, it is possible to calculate a reasonable estimate of the actual tubing diameter. The diameter value corresponding to the experimental pressure drop and theoretical viscosity values was calculated for each flow rate, using the Hagen-Poiseuille equation. The mean and standard deviation of these calculated diameters were calculated for each working fluid, and are plotted in Figure 10. These three calculated diameters are averaged to determine what will now be considered the actual working diameter. The calculated average diameter was 73.35µm, with a standard deviation of 0.13µm.
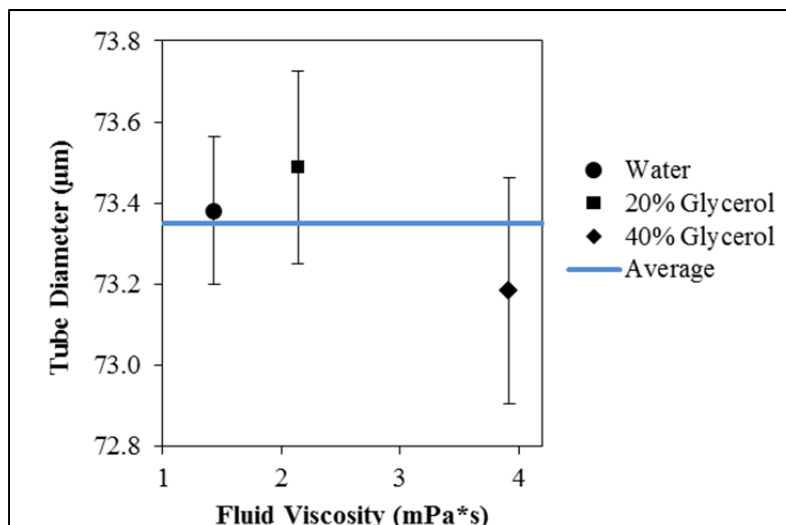
Figure 10. Average corrected #1560 tubing diameter based on water, 20% glycerol and 40% glycerol. The blue line indicates the average of these values.

4.2.3 Experimental results: #1561, #1535, #1562 tubing

These same calculations were applied to evaluate the actual tubing diameters of #1561, #1535 and #1562 tubing. As shown in Figure 11, the trends from Figure 9 held for each type of tubing, with the theoretical viscosity falling at similar positions in the span of possible diameter-viscosity relationships regardless of working fluid.
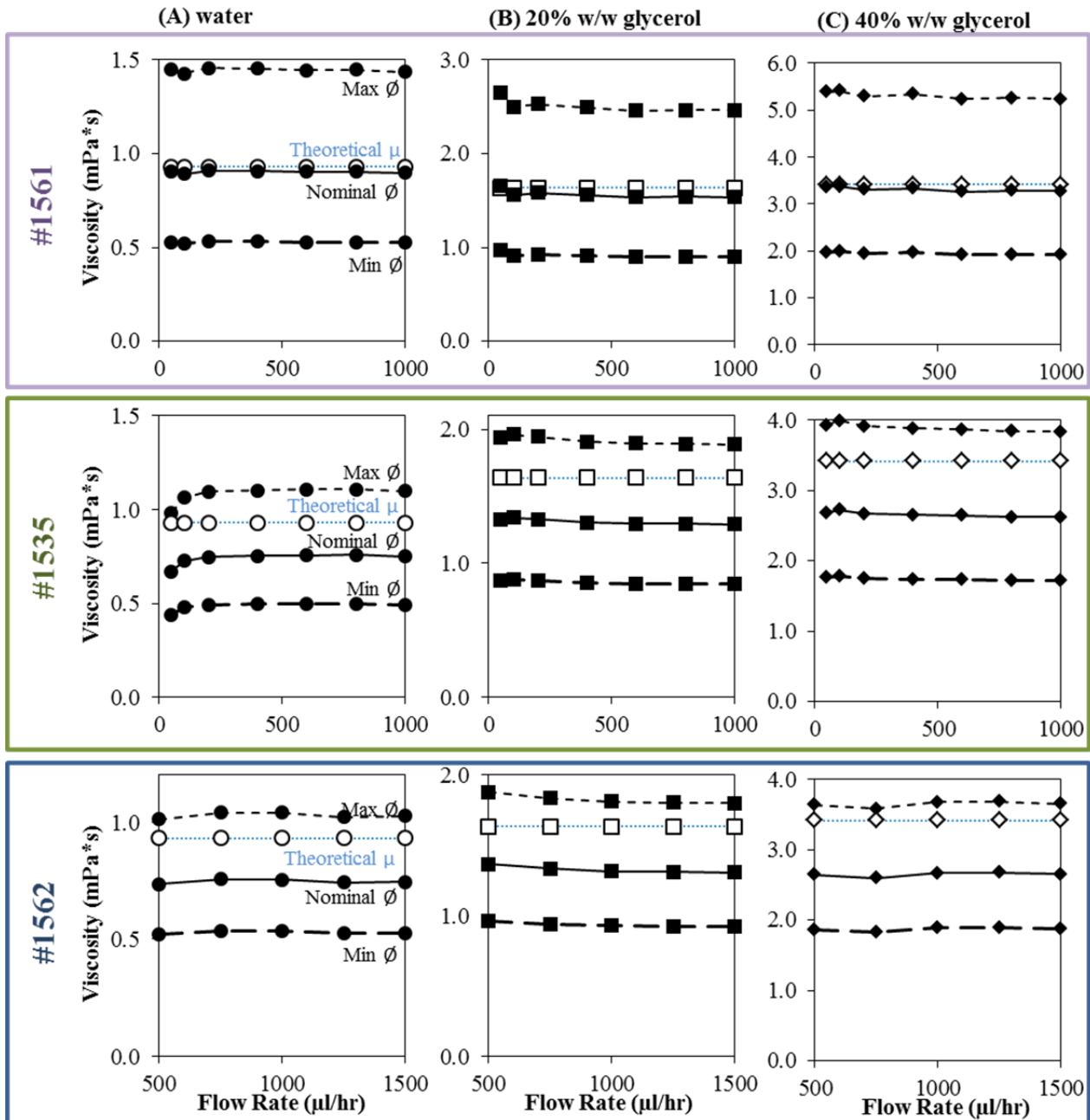
Figure 11. Experimental viscosity in #1561 (top), #1535 (middle) and #1562 tubing (bottom) calculated for maximum diameter (‑ ‑ ‑), nominal diameter (——), minimum diameter (— —) and compared to the theoretical viscosity (·····) for (A) water, (B) 20% w/w glycerol and (C) 40% w/w glycerol. Error bars not included for experimental data as they are small – on the order of 0.01 mPa*s, or 1% of the mean viscosity for each data point.

45

The calculated averages for each working fluid are shown in Figure 12. For the second smallest nominal diameter (#1561), the average values for water, 20% glycerol and 40% glycerol were all within a standard deviation of one another (Figure 12a). There was a larger amount of variation in the larger average tubing diameters (Figure 12b and Figure 12c), specifically with the high viscosity 40% glycerol. However, gap between the low range of the average diameter calculated from the 40% glycerol data and the upper range of the other data points was still extremely small: 264 nm for #1535 and 528nm for #1562. The corresponding differences in calculated viscosity are well within the existing experimental range, so no additional adjustments were used to account for this spread in calculating the actual diameter.

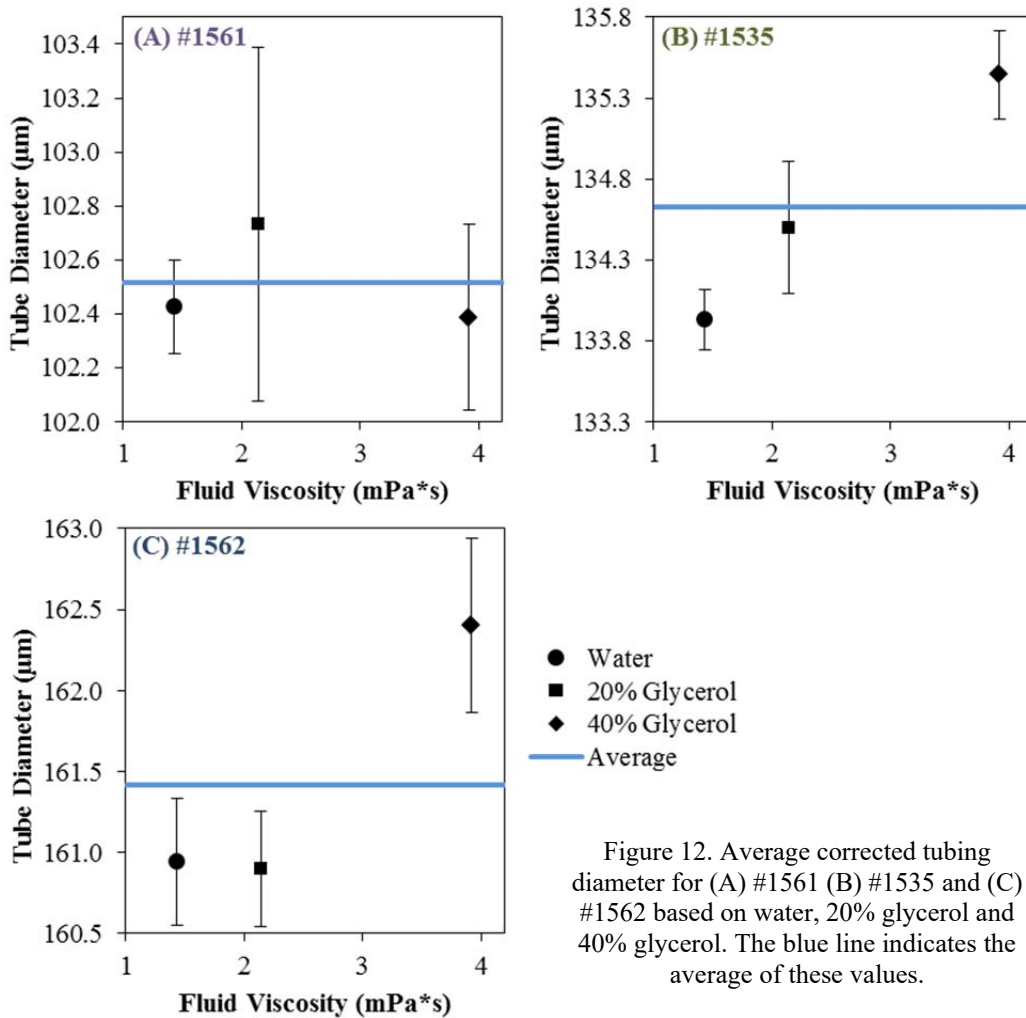Figure 12. Average corrected tubing diameter for (A) #1561 (B) #1535 and (C) #1562 based on water, 20% glycerol and 40% glycerol. The blue line indicates the average of these values.

The final results for the calculated tubing diameters are presented in Table 5. These values are used for all subsequent calculations and data analysis.

Table 5. Final calculations for mean tubing diameter based on experimental correlation with theoretical viscosity values

PEEK Tubing	Mean Diameter (μm)	Standard Deviation of Diameter (μm)
#1560	73.35	0.13
#1561	102.52	0.34
#1535	134.58	0.50
#1562	161.41	0.54

4.3   Comparison of Simulation and Experimental Results

The values for pressure drop calculated from the original Comsol model were based on a nominal tubing diameter of 63.5μm; given that pressure drop values with diameter to the fourth power, these results were significantly different from the experimentally measured pressure drop. As a final validation of the system, the Comsol geometry was updated with a PEEK tubing diameter of 73μm. The simulation results are compared to the experimental results in Table 6.

Table 6. Pressure drop per unit length results from experimental data, theoretical calculations and Comsol simulation for 73.5μm diameter, 7.0 cm long tubing at 600μl/hr

Fluid	Experimental △P/L (Pa/m)	Theoretical △P/L (Pa/m)	Simulated △P/L (Pa/m)	% Diff.
Water	219192 ± 844	216881	222464	1.1
20% w/w glycerol	375252 ± 1573	380897	39073	3.7
40% w/w glycerol	793190 ± 3010	795766	816259	2.5

The theoretical pressure drop per unit length values, calculated via Hagen-Poiseuille, are expected to be within the range of the experimental data because the 73.5μm diameter was calculated in part based on the theoretical solution viscosities. The simulated values are slightly higher than the experimental or theoretical values – this is due in part to the 0.5μm diameter difference between the simulation geometry and the calculated geometry, artificially decreasing pressure drop by ~6000 – 22000 Pa/m.

Therefore, based on the good agreement between the simulated and experimental pressure drop results, the experimental apparatus can be considered an accurate and reliable way to measure of pressure drop and viscosity.

Works Cited:

[1] F. F. Abdelall, G. Hahn, S. M. Ghiaasiaan, S. I. Abdel-Khalik, S. M. Jeter, M. Yoda and D. L. Sadowski, "Pressure drop caused by abrupt flow area changes in small channels," *Experimental Thermal and Fluid Science,* vol. 29, pp. 425-434, 2005.

[2] C. Rands, B. W. Webb and D. Maynes, "Characterization of transition to turbulence in microchannels," *International Journal of Heat and Mass Transfer,* vol. 49, pp. 2924-2930, 2006.

[3] Y. C. Toufik and S. M. Ghiaasiaan, "Pressure drop caused by flow area changes in capillaries under low flow conditions," *International Journal of Multiphase Flow,* vol. 34, no. 1, pp. 2-12, 2008.

[4] P. M.-Y. Chung, M. Kawaji, A. Kawahara and Y. Shibata, "Two-Phase Flow Through Square

and Circular Microchannels - Effects of Channel Geometry," *Journal of Fluids Engineering,* vol. 126, no. 4, pp. 546-552, 2004.

[5] J. D. Wehking, "Pressure Losses Experienced by Liquid Flow Through PDMS Microchannels with Abrupt Area Changes," University of Central Florida, 2005.

[6] Glycerine Producers' Association, "Physical properties of glycerine and its solutions," 1963.

Chapter 5
Initial Results

5.1   Initial Data Analysis
The collected text files were imported and analyzed in Matlab (batch_read_files_v4.m). This program imported all text files from a specified folder. For each data set, represented by a single text file, the program calculated the average pressure drop from all data points. The standard deviation of pressure drop for each trial was calculated as the Pythagorean sum of the variance of collected data and the linearity error of the pressure sensor itself (±0.25% Full Span). The data were then grouped into the appropriate sets of 3 repeated trials for each blood type, hematocrit, tubing diameter and flow rate. Pressure drop versus flow rate was plotted for each data set of blood type, hematocrit and tubing diameter. These graphs were visually analyzed for discrepancies and are presented in the following section.

5.1.1 Pressure drop versus flow rate – comparison of data sets
Each blood type resulted in a total of 24 pressure drop versus flow rate graphs (4 tubing diameters, 6 hematocrits). The validity of each data set was assessed by comparing the pressure drop versus flow rate curve on the graph to the other corresponding data sets. For the most part, all three data sets for each diameter and hematocrit were within a standard deviation of one another at each flow rate. A typical result with good agreement between data sets in shown in Figure 1.
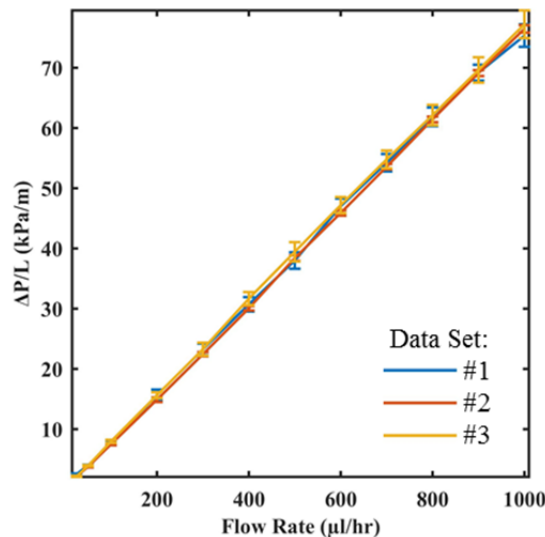
Figure 1. Example of typical pressure drop versus flow rate results (data for chicken blood, 10% hematocrit, 134.6μm diameter tubing)

However, in some cases in which there was some variation between data sets. If all data sets overlapped within a standard deviation, all data sets were retained for future analysis (Figure 2a). When two data sets were within a statistically similar range and the third was outside this range, the outlying data set was excluded from future analysis (Figure 2b).
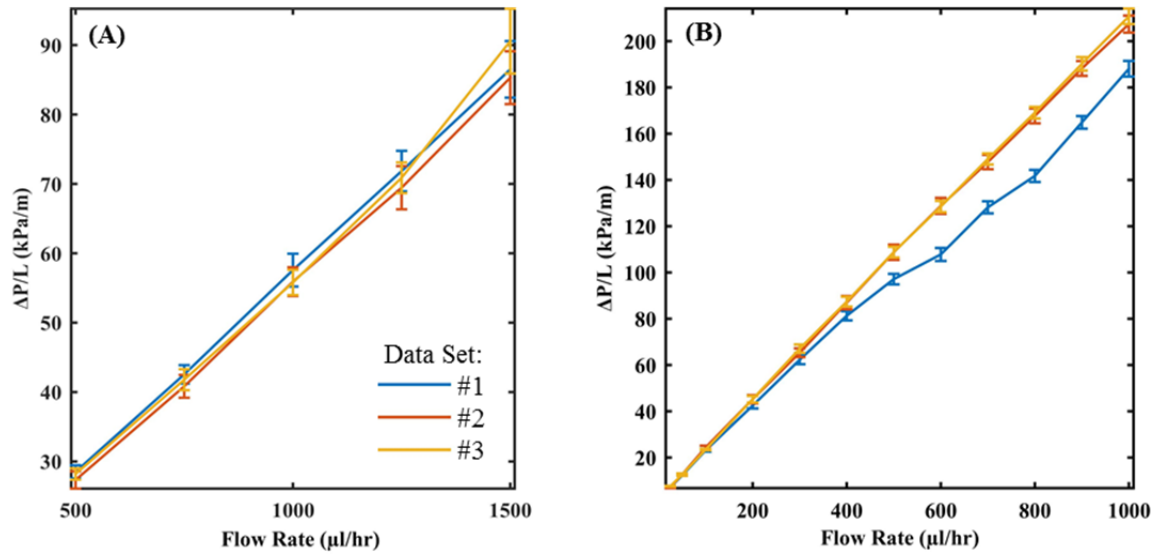
Figure 2. Examples of (A) variation in data sets for which all data sets were retained in final analysis and (B) variation of a single data set (#1) which was removed from future analysis. Data from (A) chicken blood, 10% hematocrit, 161.4μm diameter tubing and (B) chicken blood, 40% hematocrit, 134.8μm diameter tubing.

Reasons for aberrant data sets included the presence of irregular molecules in the blood causing clots and bubbles inadvertently introduced into the system. Out of 432 data sets, a total of 40 were excluded from further analysis. The porcine blood had the largest number of excluded data sets, which was likely a result of issues with aggregates in the blood. Across all blood types, the first trial was excluded most often, probably due to residual amounts of PBS in the system after the cleaning process.

5.2 Viscosity and Blood Type

### 5.2.1 Calculation of viscosity from experimental data

The experimental setup is similar in form and function to a capillary rheometer, often used to evaluate the flow properties of non-Newtonian fluids such as polymers. However, capillary rheometers do not produce pure, homogeneous shear flow, so some corrections are required to convert pressure drop/flow rate measurements into viscosity. The inlet and outlet effects on overall pressure drop have previously been shown to be negligible (Chapter 4), and so no further correction is required. The most important correction is to account for a non-parabolic velocity profile. The wall shear rate for a non-Newtonian fluid is generally greater than that of a Newtonian fluid. In blood flow, this effect is also influenced by the development of a cell-free layer at the wall, reducing the effects of red blood cells in this region. The development of a cell-free boundary and cell-rich core imposes a non-parabolic velocity profile, as shown in Figure 3.
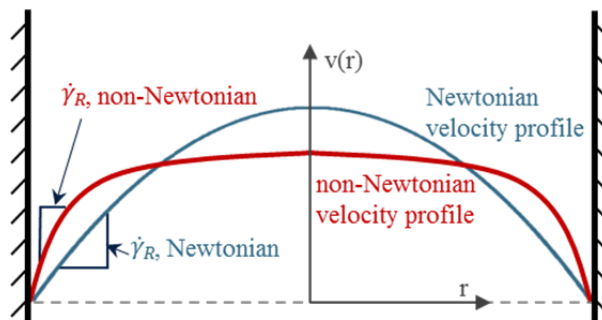
Figure 3. General comparison of Newtonian and non-Newtonian velocity profiles.

The Weissenberg-Rabinowitsch correction allows for a point-by-point determination of the true shear rate ($\dot{\gamma}_R$) based on the differentiation of the apparent shear rate and known shear stress (τ). The data set can then use the actual shear rate to determine viscosity

50

(μ) via the Newtonian equation:

$$\mu = \frac{\tau}{\dot{\gamma}_R} \tag{5.1}$$

For the no-slip condition, laminar flow in a horizontal pipe is a balance of the pressure and viscous forces acting along the cross-section and length of the pipe. This leads to the force balance:

$$p_1 \pi r^2 - (p_1 - \Delta p)\pi r^2 - 2\pi r l = 0 \tag{5.2}$$

which simplifies to:

$$\frac{\Delta p}{l} = \frac{2\tau}{r} \tag{5.3}$$

To apply the Weissenberg-Rabinowitsch correction for, the natural logarithm of the assumed shear rate, where $\dot{\gamma}_a$ is:

$$\dot{\gamma}_a = \frac{4Q}{\pi r^3} \tag{5.4}$$

is plotted versus the natural logarithm of the wall shear stress, where τ_R is:

$$\tau_R = \frac{\Delta p}{l}\frac{R}{2} \tag{5.5}$$

and the slope (*a*) is calculated at each point:

$$a = \frac{d \ln \dot{\gamma}_a}{d \ln \tau_R} \tag{5.6}$$

For industrial-grade capillary rheometers, this calculation occurs within the software. For the analysis presented in this dissertation, the secant line across the *n-1* and *n+1* data points was used as the determination of the point-by-point slope. For endpoints, the secant line was calculated across *n* to *n+1* and *n-1* to *n*, as appropriate.

Finally, the Weissenberg-Rabinowitsch correction is applied to this value to determine the true shear rate ($\dot{\gamma}_R$) as follows:

$$\dot{\gamma}_R = \dot{\gamma}_a \left[\frac{1}{4}\left(3 + \frac{d \ln \dot{\gamma}_a}{d \ln \tau_R}\right) \right] \tag{5.7}$$

This value is then used to calculate the effective viscosity (μ_{eff}) for a given flow rate and tubing diameter using equation 5.1. The true shear rate ($\dot{\gamma}_R$) is used for all subsequent graphs and calculations.

5.2.2 Results: Effective viscosity versus shear rate

The calculated effective viscosities for each animal blood type are plotted below. Error bars are present, but the overall error was generally small, and some bars are obscured by the plotted points. The reference colors for each blood type are shown in Figure 4; these colors will be used for the remainder of this dissertation.
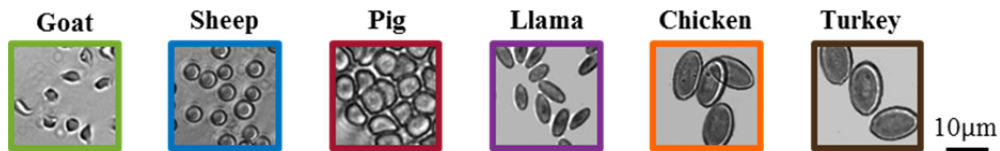
Figure 4. Reference colors for each blood type

51

The experimentally-determined effective viscosity of goat blood is shown in Figure 5. The greatest amount of shear-rate dependence is found in the smallest tubing diameter, particularly at hematocrits of 30% and above. At this size, the goat blood cells are approximately 1/20th the diameter of the tubing. As the tubing diameter increases, the goat blood cell size will eventually become negligible in comparison to vessel diameter; for the 161μm tubing, the viscosity is very nearly constant regardless of shear rate, even at high hematocrit flows.
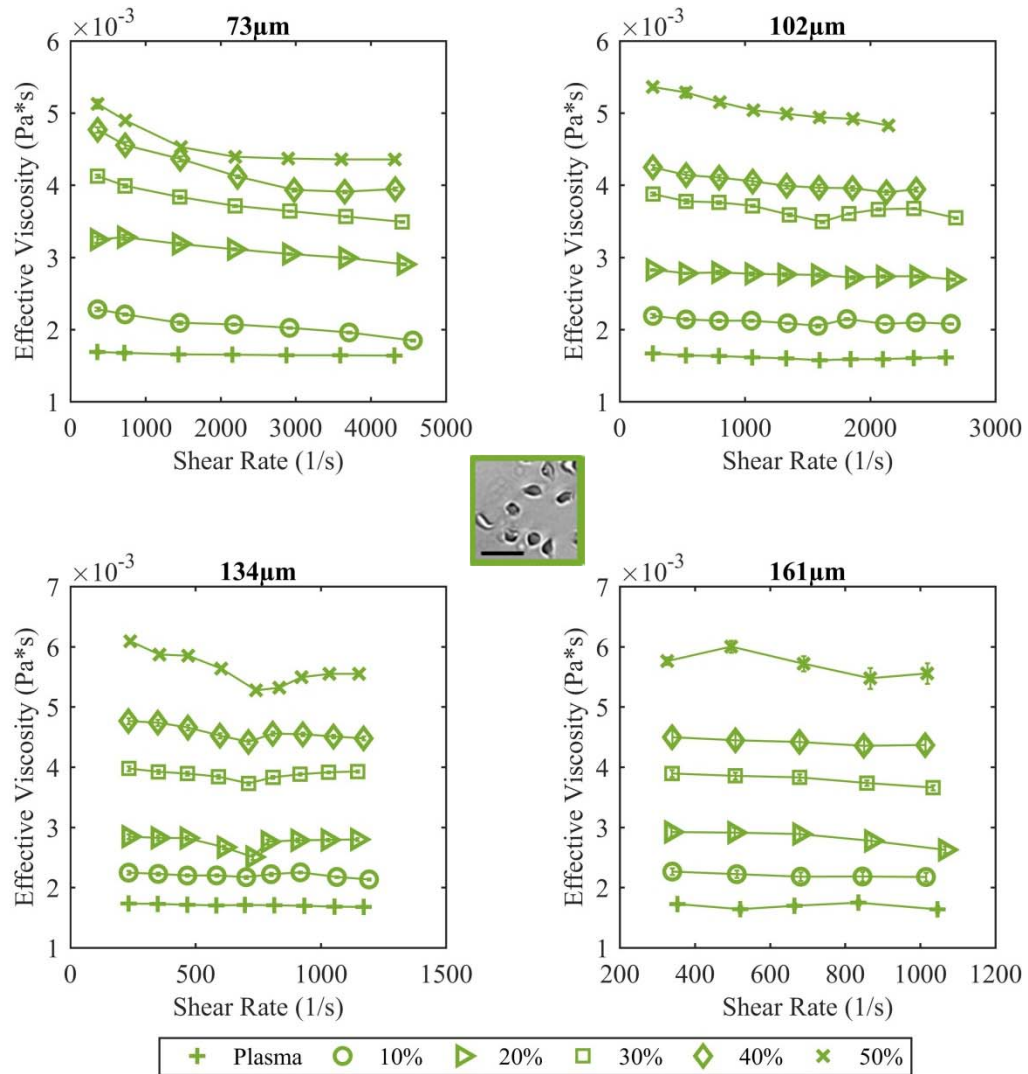
Figure 5. Effective viscosity of goat plasma (+) and whole goat blood at hematocrits of 10% (○), 20% (▷), 30% (□), 40%(◊) and 50% (✕) with respect to calculated shear rate. Center: goat erythroctyes with a 10μm scale bar.

Effective viscosity of sheep blood is presented in Figure 6. As with the goat blood, there is a noticeable viscosity dependence on shear rate at small tubing diameter; this dependence can also be observed for high hematocrit samples even in the largest tubing diameter.

Figure 6. Effective viscosity of sheep plasma (+) and whole sheep blood at hematocrits of 10% (○), 20% (▷), 30% (□), 40%(◊) and 50% (✕) with respect to calculated shear rate. Center: sheep erythrocytes with 10μm scale bar.

Effective viscosity results for pig blood are shown in Figure 7. The porcine blood was exceptionally prone to issues such as clogging, regardless of experiment type or blood sample. Of the blood types selected for this experiment, it is the only one known to regularly aggregate, and this tendency is likely responsible for the large amount of variation present in the data. In particular, the changes in fluid path diameter from the syringe through the connectors into the small-scale tubing are problematic when working with aggregating blood. The differences in diameter result in significant changes in flow velocity and shear rate, allowing rouleaux to form upstream of the small-diameter tubing. The transition to the high shear rate regime of the PEEK

53

tubing is rapid, likely causing rouleaux to enter the tubing itself while disaggregating. These issues were encountered when working with pig blood in a variety of microfluidic systems, essentially anytime there was a need to mix micro- and macro-scale vessel sizes while driving flow at an appreciable rate. Human blood aggregates to a similar degree as pig blood [1, 2], indicating the need for additional planning when utilizing blood with this characteristic.
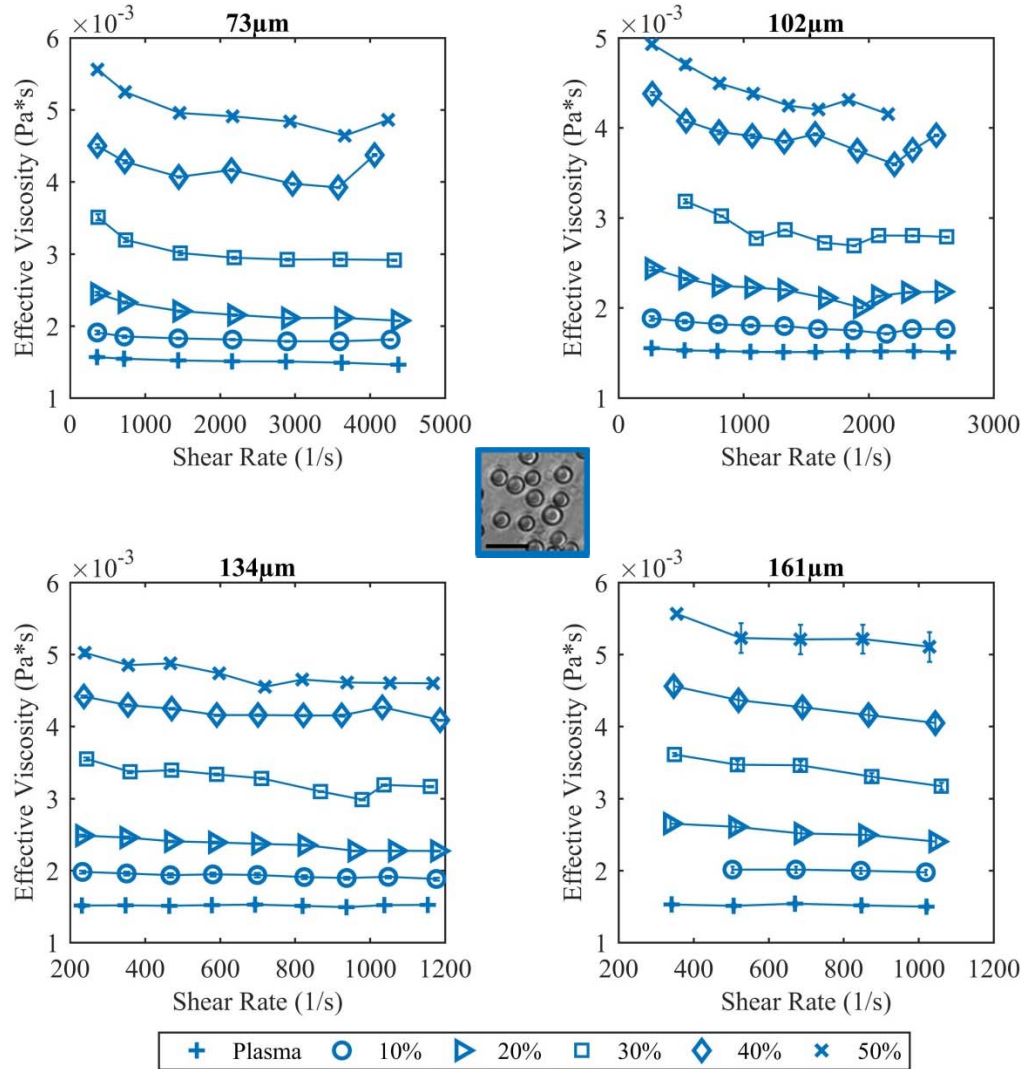

Figure 7. Effective viscosity of pig plasma (+) and whole pig blood at hematocrits of 10% (○), 20% (▷), 30% (□), 40%(◇) and 50% (✕) with respect to calculated shear rate. Center: pig erythrocytes with 10μm scale bar.

Despite the observed issues with clogging, there are still interesting details worth noting in the pig blood viscosity plots. First, as with the other blood types, even a low volume fraction of erythrocytes had an observable impact on the measured viscosity. Porcine plasma itself displayed constant, Newtonian properties. Secondly, nearly all the low hematocrit samples displayed shear-thickening properties, as opposed to the shear-thinning that is expected from blood and the formation of a cell-free layer. This "shear-thickening" – particularly obvious at 10 and 20% hematocrit in the 134μm tubing – is an artifact of this experimental setup. At high flow

54

rates, even more force is applied to the rouleaux with less time to disaggregate in the transition regime, causing rouleaux to build up at the narrow tubing entrance while also potentially be carried further into the tubing itself. Finally, while the measurement issues and shear-thickening artifacts begin at 10% hematocrit, and the problems escalate with increasing hematocrit, in all four tubing diameters the 50% hematocrit samples display very reasonable shear-thinning curves resembling the other blood types. This may initially seem counterintuitive. However, increasing blood hematocrit beyond a certain point is actually a barrier to blood cell aggregation [3]. The high volume fraction occupied by cells impairs the process of reorientation required to form rouleaux – particularly for longer rouleaux – in this case once again allowing the experimental setup to function as expected. Based on these issues and observations, only the plasma and 50% hematocrit data are used in future comparison and analysis.

The effective viscosity of llama blood (Figure 8) was among the most constant over the experimental shear rate ranges for hematocrits of 10-30%. There is an indication of shear-thickening for the 50% hematocrit blood in the 73μm tube. For this vessel diameter, the orientation of the red blood cell is significant – when it is longitudinally oriented with the
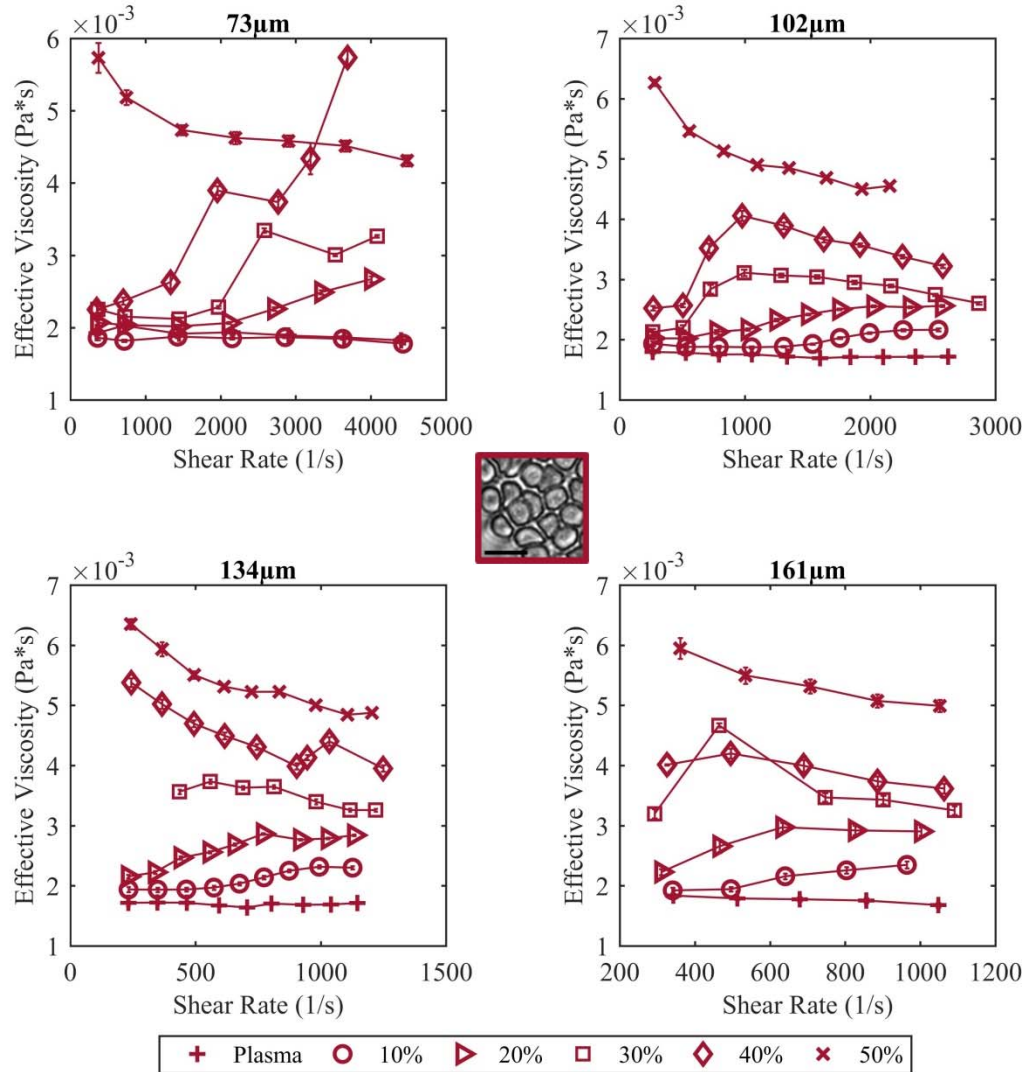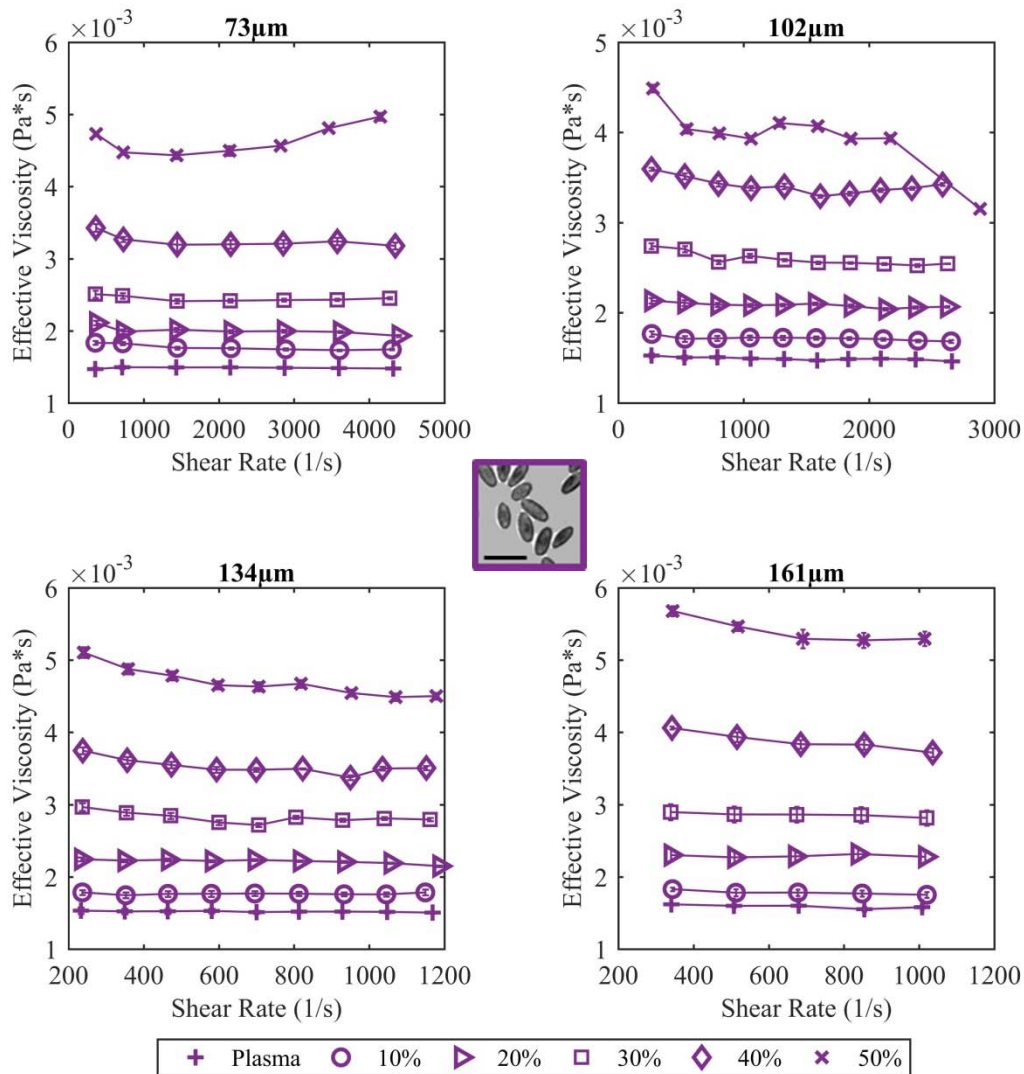

Figure 8. Effective viscosity of llama plasma (+) and whole llama blood at hematocrits of 10% (○), 20% (▷), 30% (□), 40%(◊) and 50% (×) with respect to calculated shear rate. Center: llama erythrocytes with 10μm scale bar.

direction of flow, its size relative to the tube is comparable to the goat and sheep blood cells. Elliptical blood cells are observed to orient in this manner in viscometers, for example [4]. However, if the cell is oriented crosswise to the direction of flow, its long axis is more than 1/10th the size of the vessel diameter. Thus, cell orientation has a strong impact on overall viscosity. Increasing the flow rate has a negligible impact on the length of the transition region before the narrow tubing inlet, and these elongated cells encounter a similar situation as the aggregating porcine blood. The high volume fraction inhibits cell reorientation, which becomes noticeable as the time scale for reorientation at the tube inlet decreases with increasing flow rate.

The mammalian blood had effective viscosities ranging from 1.5 to 7 mPa*s. The first avian blood sample – chicken (Figure 9) – has effective viscosities ranging to greater than 10 mPa*s. Other than this increased range, the trends are similar to what was observed with llama blood. The chicken blood has a relatively constant viscosity at low hematocrits, particularly in the two larger diameter tubes, with some shear-thinning becoming evident as hematocrit increases. It is also noted that in all four tubing diameters, the 50% hematocrit sample does not cover the same range shear rate range as the lower hematocrits. In all four tube sizes, the

Figure 9. Effective viscosity of chicken plasma (+) and whole chicken blood at hematocrits of 10% (○), 20% (▷), 30% (□), 40%(◊) and 50% (✕) with respect to calculated shear rate. Center: chicken erythrocytes, 10μm scale bar

56

pressures at those higher flow rates exceeded the 103.4 kPa maximum of the pressure transducer. This was particularly true in the 161μm tubing, where only the two lowest flow rates were measurable. An additional, lower flow rate was measured for the 50% hematocrit chicken blood for that tubing diameter.

Finally, the effective viscosity of turkey blood is presented in Figure 10. The range of effective viscosities is similar to the mammalian blood types rather than the chicken blood, and at low hematocrits there is almost no observable shear thinning. Unlike the chicken blood, the entire flow rate range was measurable for 50% hematocrit samples in the two larger tubing diameters. However, at 50% hematocrit no flow – even at substantially lower flow rates – was possible in the 73μm tubing.
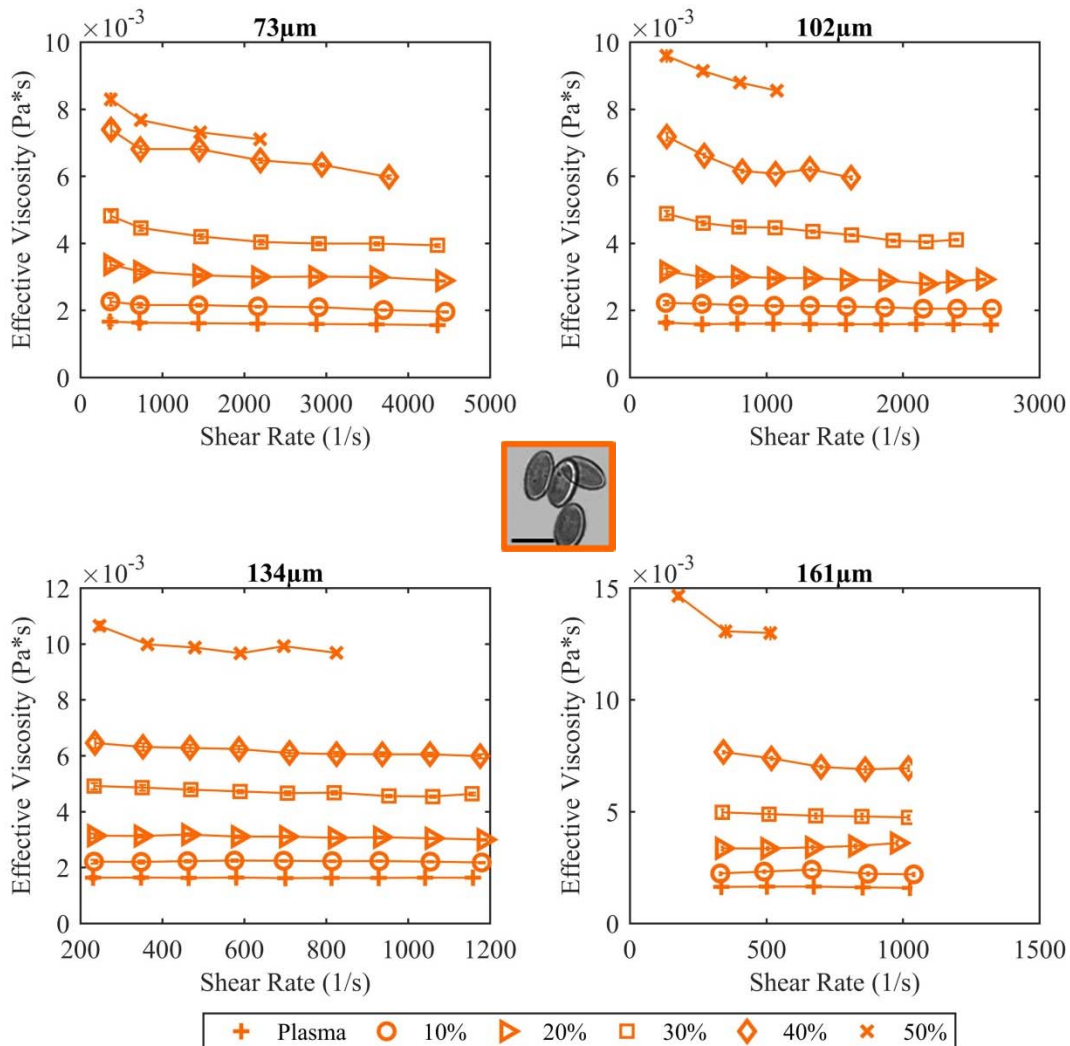

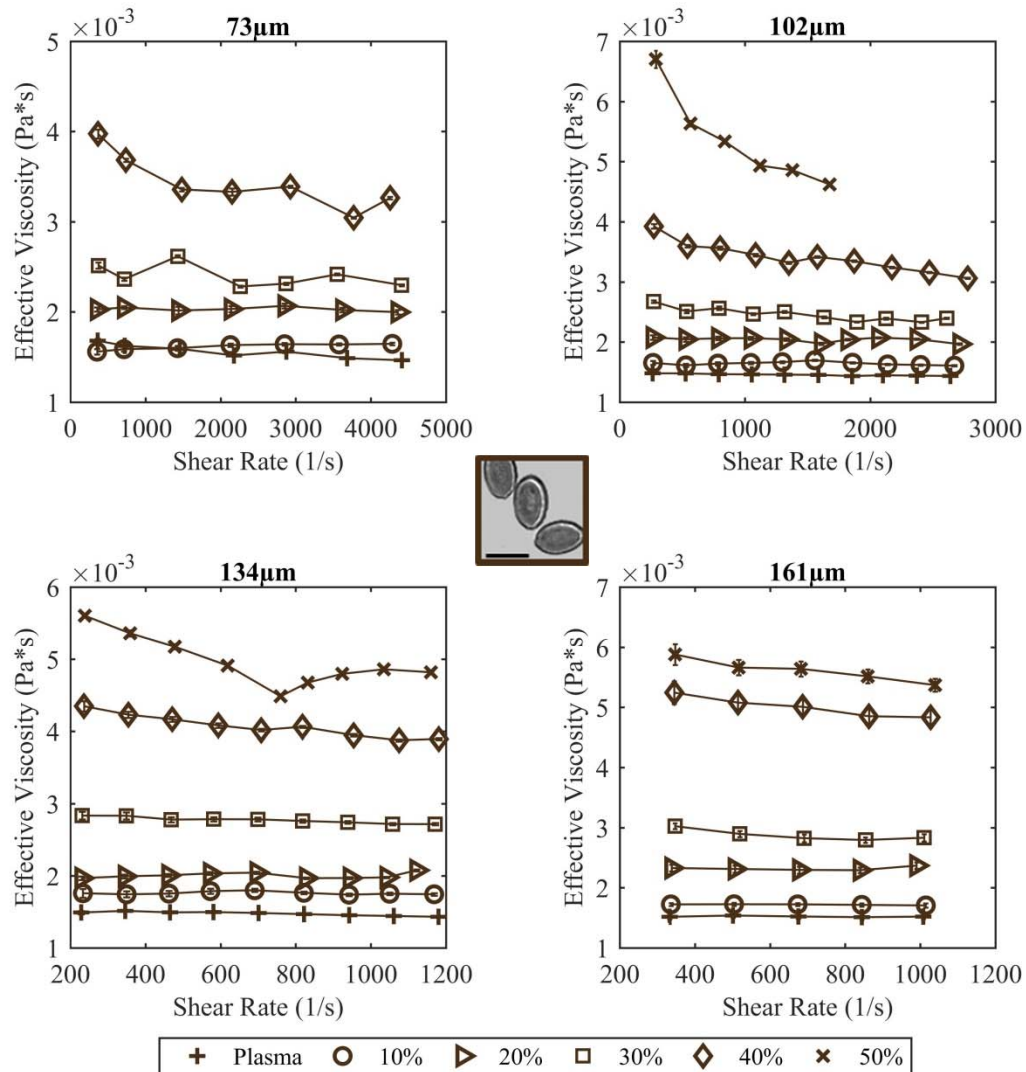
Figure 10. Effective viscosity of turkey plasma (+) and whole turkey blood at hematocrits of 10% (○), 20% (▷), 30% (□), 40%(◇) and 50% (×) with respect to calculated shear rate. Center: turkey erythrocytes, 10μm scale bar

5.3 Comparison Across Blood Types

The effective viscosity of each species for varying hematocrits, flow rates and tubing diameters fell within a similar 1.5 – 10 mPa*s range. However, the effective viscosity is impacted both by the red blood cell characteristics and plasma viscosity. A model is fit to the data to allow for comparison at identical shear rates, and the results are normalized by the plasma viscosity of each species to isolate the impact of differing red blood cell characteristics.

5.3.1 Casson model

The shear-dependent viscosity of human and non-human blood has been modeled using a number of similar methods, the most common of which are the power law equation and the Casson model [5, 6, 7, 8, 9]. The Casson model accounts for non-zero yield stresses. If none are present, the resulting model will take the form of a power law equation. The Casson model was therefore selected to model the relationship between viscosity and shear rate as it allows for fewer assumptions regarding flow at very low shear rates.

The Casson model, originally developed in the 1950s to model the shear-thinning properties of printer inks [10], has the following form:

$$\tau^{0.5} = a|\dot{\gamma}|^{0.5} + b^{0.5} \tag{5.8}$$

where b ultimately represents the yield stress at very low shear rates.

This model was fit to each set of data via linear regression using the true shear rate calculated from the Weissenberg-Rabinowitsch correction to obtain the fitting parameters a and b, as well as the coefficient of determination, R^2.

The fitting parameters and true shear rate were then used to calculate viscosity curves corresponding to each data set:

$$\mu_{Casson} = (a + b|\dot{\gamma}|^{-0.5})^2 \tag{5.9}$$

The R^2 values for all goat, sheep, llama, chicken and turkey data sets were >0.99. Unsurprisingly, the fit was poorer for many of the data sets with pig blood. In that subset, the lowest R^2 value was 0.9298, corresponding to the 30% hematocrit data set in the 162μm tubing.

5.3.2 Plasma viscosity

The average plasma viscosity for each species is shown in
Figure 11. Measured plasma viscosities were constant across shear rates, indicating Newtonian properties in this flow regime. This is in agreement with literature on vertebrate plasma fluid dynamics. The measured plasma viscosities were within the physiologically expected range. Viscometer analysis of plasma viscosity among mammalian species, including sheep, pigs, and humans, found a range of 1.30 (1.24/1.41) to 1.72 (1.63/1.94) mPa*s (median/25th/75th percentiles) when measured at 37°C [11]. Plasma viscosity is influenced by the quantity and characteristics of proteins and other macromolecules present in solution [12], so variation across species – and even between individuals of the same species depending on additional factors such as disease states – is expected. Despite these differences, there is not a consistent relationship between whole blood viscosity and plasma viscosity – for example, the viscometer study by Windberger et al. found the highest plasma viscosity in cattle, and the lowest in rabbits and mouse, but a uniform whole blood viscosity across the three species [11].

58
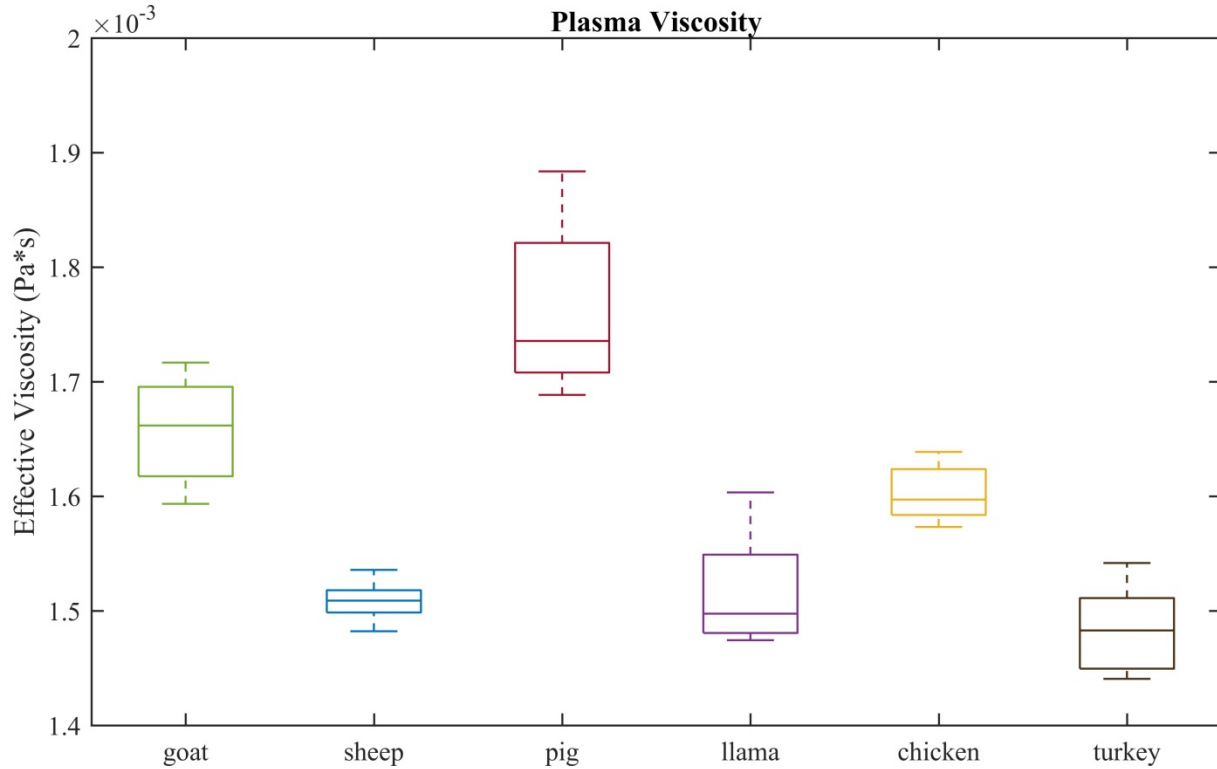
Figure 11. Effective viscosity for each type of plasma, calculated from values at all flow rates in all tubing diameters.

5.3.3 Relative viscosity

The experimental data and model data were normalized by the species-specific plasma viscosity in each tubing diameter, and the results for each hematocrit plotted by tubing diameter: 73μm - Figure 12, 102μm - Figure 13, 134μm - Figure 14 and 161μm - Figure 15. Twenty graphs across four figures is an unwieldy way to examine data for trends, and Chapter 6 will focus on identifying the roles of hematocrit, cell size, cell shape and cell deformability in a more practical fashion by examining trends at single shear rates. These plots are instead intended to visually convey the results of the Casson model (the numerical values of which will also be examined in Chapter 6) and to illustrate some general questions and trends that highlight how the complexity of this problem.

Perhaps the most obvious first point from a quick survey of the graphs is that chicken blood, drawn in orange, has a much higher relative viscosity than any other blood at essentially any hematocrit and tubing diameter, but especially at 30-50% hematocrits. This can be used to frame a few additional questions in preparation for Chapter 6.

First, is the high relative viscosity of chicken blood attributable to its large cell size? The chicken red blood cells are quite large in comparison to the mammalian erythrocytes. And yet, the smallest of all vertebrate erythrocytes – belonging to the goat – are quite often second in relative viscosity, particularly at 20-30% hematocrit in Figure 12 and Figure 13. Furthermore, if size matters, is it surprising that largest red blood cells of this experiment, found in turkey blood, are generally found to have the lowest relative viscosity?

Clearly, simply examining the external dimensions of a red blood cell is not the sole key

59

to this puzzle. The split between nucleated and non-nucleated blood cells is also impacted by the high relative viscosity of chicken blood and low relative viscosity of turkey blood. Shape is, perhaps, the second possibility – chicken erythrocytes being oval-shaped in contrast to the prolated shape of most mammalian species. However, like their nucleated brethren the turkey red blood cells, the similarly elliptical llama blood cells exhibit nearly the lowest relative viscosity of all species. The only major exception was previously discussed in section 5.2.2: flow at 50% hematocrit in the smallest tubing diameter, where orientation of llama red blood cells may have a significant impact at the tubing inlet.

A final piece to consider is the role of cellular deformability, which has yet to be addressed. This topic will be further discussed in subsequent chapters, but a few points are worth mentioning here. First, within the literature llama blood cells and others of the Camelidae family are observed to exhibit little to no deformation in shear flow, and instead orient longitudinally in flow where other mammalian cells would stretch [4, 13]. Secondly, disregarding the aggregating pig blood which is now plotted only at 50% hematocrit, sheep erythrocytes are known to be the most deformable of this subset of vertebrate blood [13].

In short, these graphs indicate that this set of data is worthy of further analysis.

Figure 12. Relative viscosity data (points with error bars) and Casson model (lines) in the 73μm diameter tubing for each species and hematocrit.

Figure 13. Relative viscosity data (points with error bars) and Casson model (lines) in the 102μm diameter tubing for each species and hematocrit.
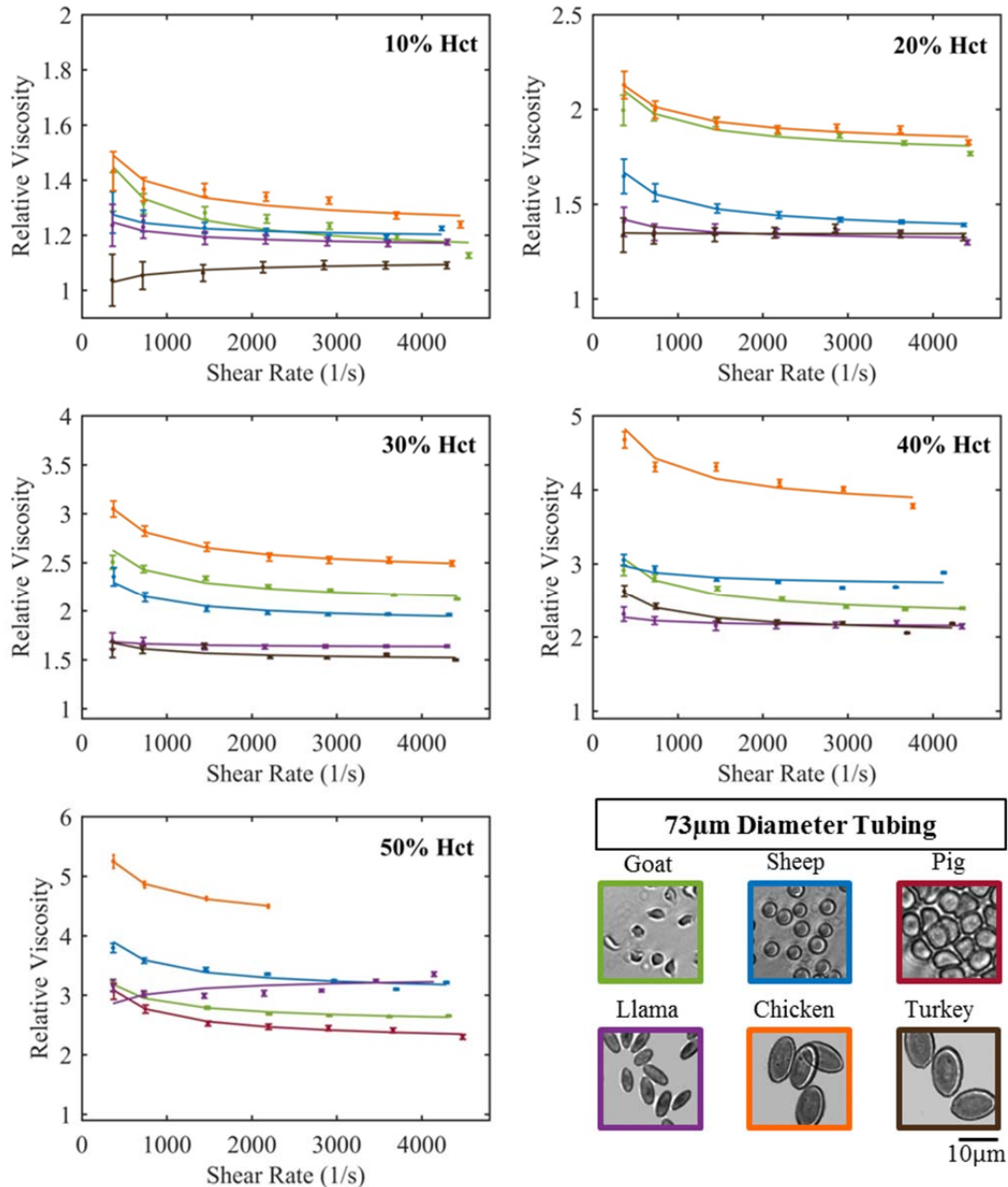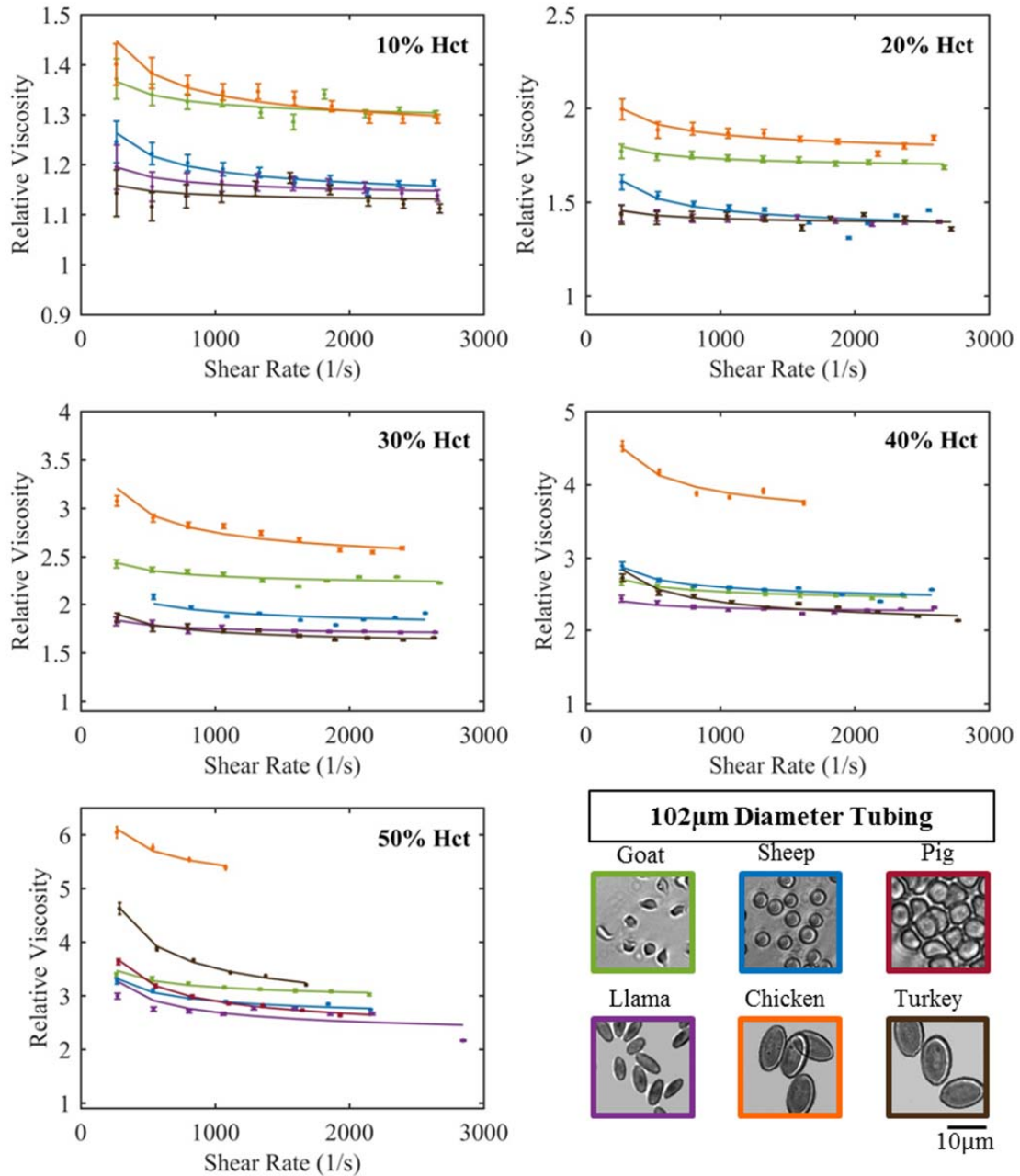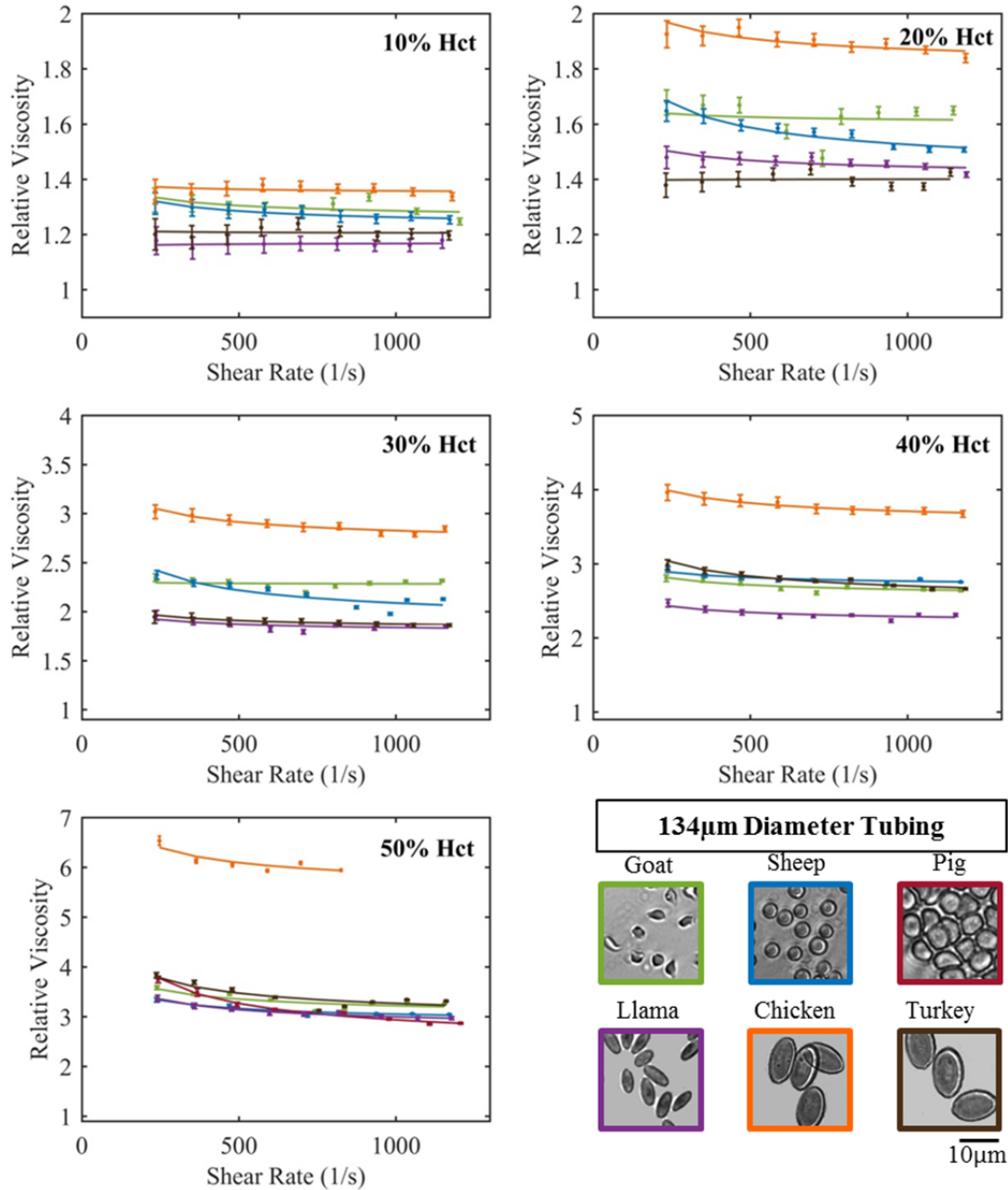
Figure 14. Relative viscosity data (points with error bars) and Casson model (lines) in the 134μm diameter tubing for each species and hematocrit.
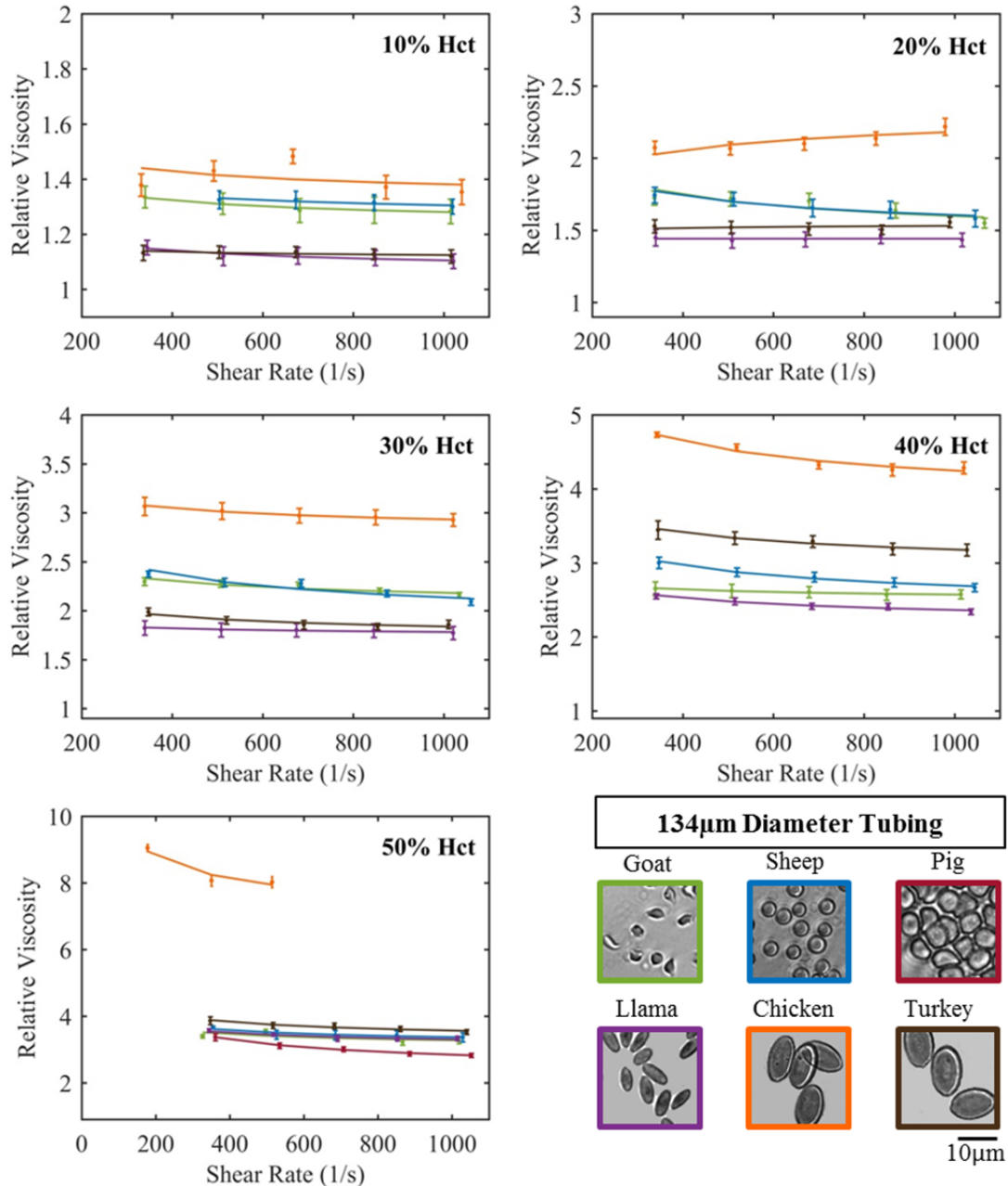
Figure 15. Relative viscosity data (points with error bars) and Casson model (lines) in the 134μm diameter tubing for each species and hematocrit.

Works Cited:

[1] X. Weng, G. Cloutier, P. Pibarot and L.-G. Durand, "Comparison and simulation of different levels of erythrocyte aggregation with pig, horse, sheep, calf and normal human blood," *Biorheology,* vol. 33, no. 4, pp. 365-377, 1996.

[2] A. V. Cardoso and A. O. Camargos, "Geometrical Aspects During Formation of Compact Aggregates of Red Blood Cells," *Materials Research,* vol. 5, no. 3, pp. 263-268, 2002.

[3] T. L. Fabry, "Mechanism of Erythrocyte Aggregation and Sedimentation," *Blood,* vol. 70, pp. 1572-1576, 1987.

[4] H. O. Stone, H. K. Thompson, Jr. and K. Schmidt-Nielsen, "Influence of erythrocytes on blood viscosity," *American Journal of Physiology,* vol. 214, no. 4, pp. 913-918, 1968.

[5] F. J. Walburn and D. J. Schneck, "A constitutive equation for whole human blood," *Biorheology,* vol. 13, pp. 201-210, 1976.

[6] J. -B. Zhang and Z. -B. Kurang, "Study on blood constitutive parameters in different blood constitutive equations," *Journal of Biomechanics,* vol. 33, pp. 355-360, 2000.

[7] W. Chang, D. Trebotich, L. P. Lee and D. Liepmann, "Blood flow in simple microchannels," in *1st Annual International IEEE-EMBS Special Topic Conference on Microtechnologies in Medicine & Biology*, Lyon, France, 2000.

[8] S. Al-Roubaie, E. D. Jahnsen, M. Mohammed, C. Henderson-Toth and E. A. Jones, "Rheology of embryonic avian blood," *American Journal of Physiology,* vol. 301, no. 6, pp. H2473-H2481, 2011.

[9] G. R. Cokelet, "The Rheology of Human Blood (Thesis)," Massachusetts Institute of Technology, 1963.

[10] N. Casson, "A flow equation for pigment-oil suspensions of the printing ink type," Pergamon press, 1959.

[11] U. Windberger, A. Bartholovitsch, R. Plasenzotti, K. J. Korak and G. Heinze, "Whole blood viscosity, plasma viscosity and erythrocyte aggregatoin in nine mammalian species: reference values and comparison of data," *Experimental Physiology,* vol. 88, no. 3, pp. 431-440, 2003.

[12] G. Késmárky, P. Kenyeres, M. Rábai and K. Tóth , "Plasma viscosity: a forgotten variable," *Clinical Hemorheology and Microcirculation,* vol. 39, no. 1-4, pp. 243-246, 2008.

[13] J. E. Smith, N. Mohandas and S. B. Shohet, "Variability in erythrocyte deformability among various mammals," *American Journal of Physiology,* vol. 236, no. 5, pp. H725-H730, 1979.

Chapter 6
Data Analysis

Basic quantitative comparison of the experimental data makes it clear that the viscosity of whole blood flowing in small tubes varies with blood type and other flow characteristics. This chapter further investigates these differences through examination of the four primary variables in the composition of whole blood: hematocrit, red blood cell size, red blood cell shape, and red blood cell deformability.

6.1   Role of Hematocrit

It is generally understandable that for a given flow, adding insoluble particles to the flow with a higher viscosity than that of the carrier liquid will increase the overall viscosity of the suspension. In simpler terms, having more blood cells suspended in a given volume of plasma will increase the viscosity of whole blood.

6.1.1 Variation of relative viscosity with hematocrit

This subject has been experimentally demonstrated and analyzed in a number of studies, both at the macroscale in viscometers and in a similar manner as Fåhraeus and Lindqvist in microscale tubing. In 1992, Pries et al [1] compared 21 existing data sets, as well as their own experimental data, and developed an equation describing relative viscosity (μ_{rel}) as a function of hematocrit at a specific diameter (Hct):

$$\mu_{rel} = 1 + B * [(1 - Hct)^C - 1] \qquad (6.1)$$

Fitting parameter B relates to the steepness of the viscosity-hematocrit relationship, and curvature is defined by the fitting parameter C, where C=1 is a linear relationship, and C<1 defines an upward sloping curve. The authors compared the correlation coefficients (r^2) from this fitting equation to those obtained by a purely linear relationship. The correlation coefficients for the smallest diameters included in the study – 3.3-6μm – had no statistically significant difference between equation 6.1 and a linear fit. Experimental data from tube diameters greater than this range (9 μm - 930μm) showed a good fit to equation 6.1, with correlation coefficients ranging from 0.926 to 1.000.

The shape of this curve (Figure 1) for tubing diameters >6μm is a good match for the typical behavior of particle-laden flows. Rutgers [2, 3] and Thomas [4] describe three regimes identified in existing particle research which can be qualitatively identified in these Figure 1 curves. First is the dilute regime, for volume fractions (ϕ) of ϕ≤0.01-0.02, where the relationship between relative
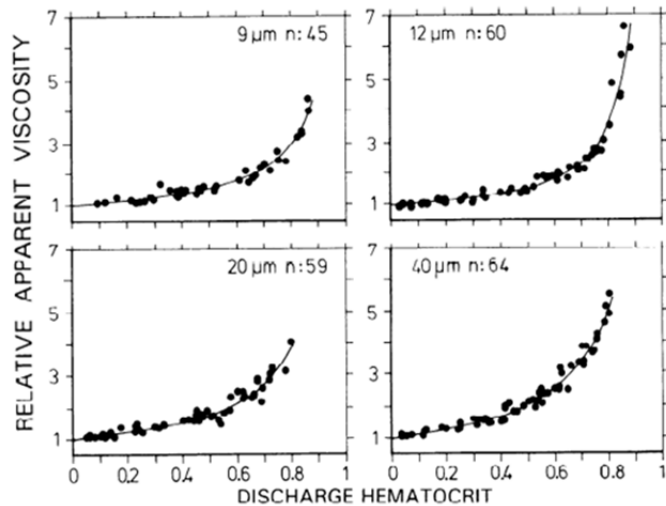

Figure 1. Relative viscosity versus hematocrit for *n* datapoints in 9μm, 12μm, 20μm and 40μm diameter tubing. Lines were generated by equation 6.1. From Pries et al [1].

viscosity and volume fraction is linear with Newtonian flow characteristics. The semi-dilute regime extends from this dilute regime up to $\phi \leq 0.25$, where the relationship is still roughly Newtonian, but develops a higher order dependence on volume fraction. The concentrated regime begins around $\phi = 0.25$ as relative viscosity begins to increase even more with volume fraction and non-Newtonian behavior such as shear thinning begins to significantly impact flow behavior.

Various relationships have been developed to describe these regimes. In-depth discussion of these regimes and associated fitting equations is available in [5]. They are presented here briefly to provide context for the form of equation 6.1.

The first and perhaps most well-known equation for dilute suspensions of spheres was developed by Einstein:

$$\mu_{rel} = 1 + B\phi \tag{6.2}$$

Equations in the semi-dilute regime expand on equation 6.2 with higher order terms:

$$\mu_{rel} = 1 + B\phi + B_1\phi^2 + \ldots \tag{6.3}$$

In the concentrated regime, the polynomials from equation 6.3 begin to under-predict relative viscosity. Fit continues to worsen as volume fraction increases, partially because equation 6.2 and 6.3 assume that viscosity as $\phi \to 1$ will be a real value (i.e. flow is possible). In reality, the densest packing fraction at which flow is possible for monodisperse spheres is $\phi \approx 0.74$. A theoretical illustration of an ideal maximum packing fraction (ϕ_m) is shown in **Error! Reference source not found.**. This concept will be further addressed in Section 6.3.
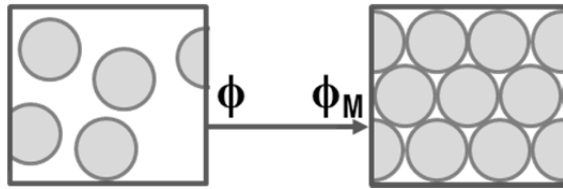
Figure 2. Illustration of volume fraction ϕ for monodisperse, rigid spheres, and the associated maximum packing fraction ϕ_M

Thus, equations describing the concentrated flow regime take into account the maximum packing fraction ϕ_m:

$$\mu_{rel} = \left(1 - \frac{\phi}{\phi_m}\right)^{-B\phi_m} \tag{6.4}$$

where ϕ_m is also considered a fitting parameter. This equation and the potential implications of cell shape in regards to maximum packing fraction will be discussed in section 6.3.1.

Comparison of the equations spanning the dilute (6.2), semi-dilute (6.3) and concentrated (6.4) regimes with the blood viscosity fitting equation (6.1) provides rational for the form of the Pries equation, which spans the full hematocrit range for blood in a single tubing diameter.

6.1.2 Fitting data to Pries equation

Fitting parameters B and C for equation 6.1 were determined for each type of blood and tubing diameter using Matlab's fit capabilities. The fits were performed for relative viscosity at a single shear rate ($1000s^{-1}$), which was calculated from the Casson model (Section 5.3.1). The Casson fit was used rather than the experimental data in order to calculate relative viscosity from a single shear rate; the experimental data represented a range of true shear rates for each given flow rate. Refer to Chapter 5 for further information on this process.

67

The upper[1] and lower bounds for the fitting parameters were selected based on the maximum and minimums found in Pries [1],with the range doubled to allow for the potential differences resulting from use of nonhuman erythrocytes. The fit for each blood type is shown in Figure 3, along with the relative viscosity values calculated from the Casson model (Section 5.3.1).
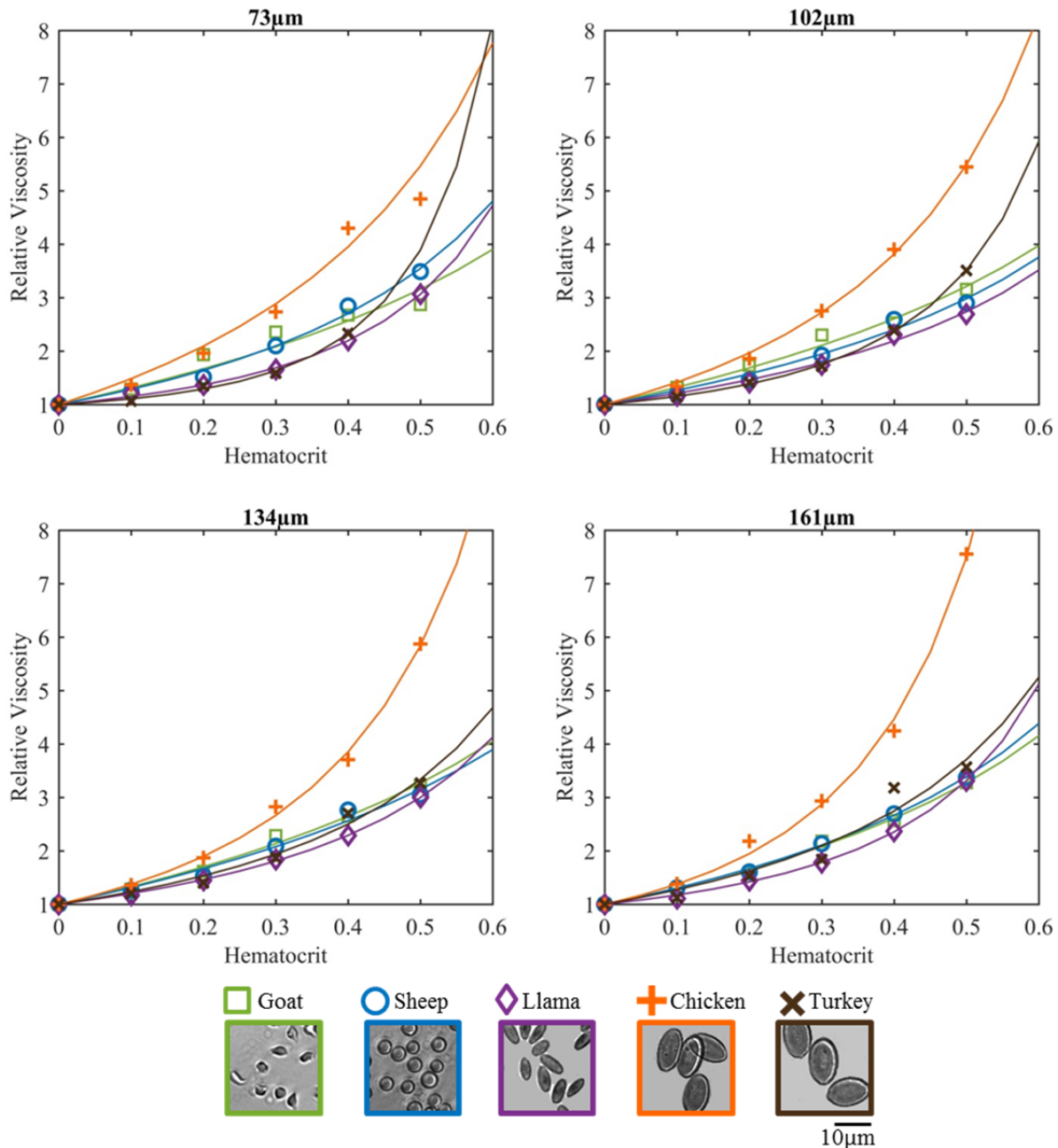
Figure 3. Relative viscosity values calculated from Casson model at $\dot{\gamma}_R = 1000$ s^{-1} (markers) and the corresponding fit line based on equation 6.1 (solid lines).

---

[1] B-values for goat blood, particularly in the smallest tubing diameter, were consistently at upper parameter bound, even for larger and smaller parameter ranges. A purely linear fit yielded slightly better correlation coefficients for the smallest tubing diameter, and comparable or worse values for the other three diameters; comparison of the residuals for each case showed no meaningful difference. Because the linear fit is less likely to be accurate when extrapolated to hematocrit values above the experimental range, the upper parameter range from Pries data was still used for the goat blood.

68

Three primary trends stand out on from this data. First, the chicken blood has the highest relative viscosity at every hematocrit regardless of tubing diameter. Secondly, the goat and sheep blood display very similar trends and the lowest degree of curvature as hematocrit increases. Finally, the turkey and llama blood generally begin with the lowest relative viscosity, but have a noticeable deflection point around 30% hematocrit that typically leads to higher relative viscosity compared to the sheep and goat blood. The fitting parameters for turkey blood in the 73μm tubing predict that its relative viscosity will surpass that of chicken blood between 50% and 60% hematocrit. This data set extended only to 40% hematocrit, because the 50% hematocrit turkey blood experienced continual clogging and never reached a steady state in the 73μm diameter tubing. Therefore, although this range may be less reliable, the qualitative results from the experiment do lend some credence to a strong inflection point in this hematocrit range.

A hematocrit-only analysis provides no insight into how cell characteristics are contributing to observed trends. However, the impact of hematocrit is worth an additional note in the context of benchtop microfluidic experiments. It is relatively common for early proof-of-concept experiments with lab-on-a-chip devices to use dilute suspensions of blood, often in the 1% - 10% hematocrit range [6, 7, 8, 9, 10, 11, 12, 13]. There are a number of reasons for this choice, including the basic fact that blood at physiologically-relevant hematocrits is more difficult to work with, with a higher rate of clogs and interference with some visualization techniques. However, when working within this hematocrit range, researchers should keep two thoughts in mind. First, at 1-10% hematocrit, (Figure 4a), the viscosity of the blood suspension is essentially the same as the suspending fluid itself – plasma, saline, etc. If the future applications of the microfluidic device will use whole blood (Figure 4b), compensations should be made for at least a 2-4 fold increase in viscosity – even more if the initial test fluid is a non-physiological fluid such as PBS [10, 11, 14, 15]. Next, the choice of blood at the low hematocrit range may not have a significant impact on flow characteristics – i.e. utilizing sheep blood or even chicken blood in lieu of human blood is likely to have a minimal impact on the flow profile (Figure 4a). On the other hand, if devices are being tested at higher hematocrit, the choice of blood will have an immediate impact on the flow characteristics, beginning with the fluid viscosity (Figure 4b). It is therefore important to choose fluids at for benchtop testing and device optimization within the context of the composition of the final intended sample fluid.
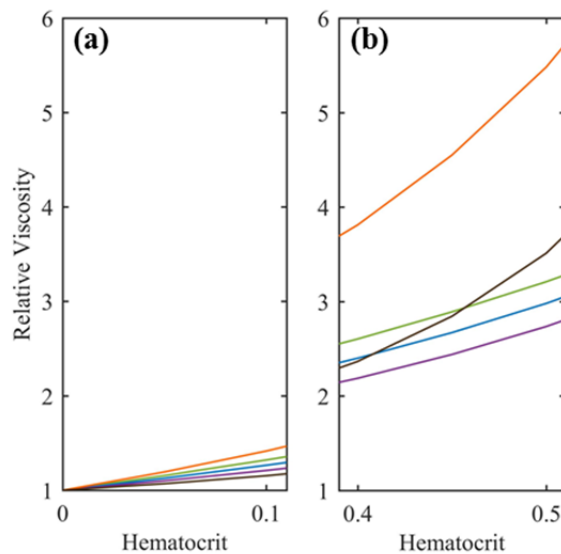

Figure 4. Relative viscosity versus hematocrit trends at (a) 1-10% hematocrit and (b) 40-50% hematocrit for chicken (orange), turkey (brown), goat (green), sheep (blue) and llama (purple) blood in 102μm diameter tubing

6.2   Role of Cell Size & Shape

The next variable to be considered is the size of the individual erythrocytes for each species. Erythrocyte sizes for the selected blood vary over a full order of magnitude. The mean cell volumes (MCV) and major cell axis lengths are listed in Table 1, as well as the fitting parameters B and C for each blood type and tubing diameter.

Table 1. Geometry and fitting parameters by blood type. Geometrical parameters compiled from [16, 17, 18, 19, 20]

Animal	MCV (fL)	Major Cell Axis (μm)	B, C (73 μm)	B, C (102 μm)	B, C (134 μm)	B, C (161 μm)
Goat	18 ± 1.2	3.3 ± 0.3	18.65, -0.16	18.65, -0.16	18.65, -0.17	6.79, -0.42
Sheep	34 ± 1.3	4.4 ± 0.4	2.64, -0.97	5.64, -0.43	18.65, -0.16	4.85, -0.58
Pig	63 ± 2.1	6.0 ± 0.9	-	-	-	-
Llama	25.5 ± 2.8	7.8 ± 0.2	0.58, -2.19	2.53, -0.75	1.39, -1.29	0.70, -2.10
Chicken	115 ± 12	12.1 ± 0.5	4.02, -1.08	2.37, -1.53	1.55, -2.04	1.09, -2.79
Turkey	136 ± 10	14.0 ± 1.0	0.21, -3.87	0.48, -2.65	1.54, -1.33	1.84, -1.30

Cell size can be described by cell volume or diameter. For spherical cells, these values are interchangeable. However, for non-spherical red blood cells, volume and diameter offer slightly different perspectives in the context of flow through a small tube. Cell volume is an important parameter in small tubes because the volume fraction of even a single cell in a given portion of the tube can be significant. In Figure 5a, the values of fitting parameter C are averaged across all tubing diameters and plotted versus the mean cell volume of each blood type. The small goat and sheep blood cells have the largest average C values, and the large turkey and chicken cell have much smaller C values. A smaller (more negative) C-value indicates a higher degree of curvature (more rapidly increasing relative viscosity) as hematocrit increases. If only these four blood types are considered, a generalized trend that larger cells have a greater impact on relative viscosity with increasing hematocrit. However, categorizing the small but ellipsoidal llama red blood cells is more challenging. The llama red blood cells have a similar mean cell
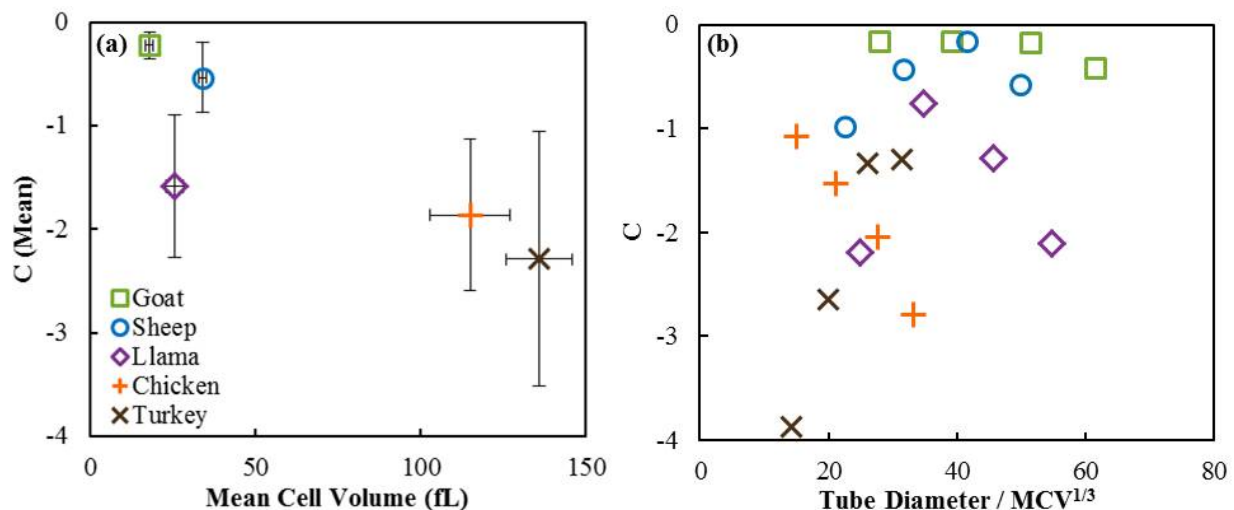

Figure 5. (a) Average values of fitting parameter C versus mean cell volume for each blood type, with error bars indicating standard deviation for C (vertical bars) and mean cell volume (horizontal bars). (b) Values of fitting parameter C for all blood types in each tubing diameter versus the ratio of tubing diameter to the cube root of mean cell volume.

70

volume as the other denucleated mammalian erythrocytes, but a range of C-values much more similar to the larger, ellipsoidal avian erythrocytes. This suggests that mean cell volume alone is not an adequate predictor of the relationship between relative viscosity and hematocrit.

One issue with considering only mean cell volume (Figure 5a) is that it fails to account for the physical flow environment, i.e. the tubing diameter. A common way to consider cell volume in the context of vessel diameter is to normalize the latter by the cube root of mean cell volume, producing a nondimensional ratio. All C-values from all tubing diameters are plotted against this in Figure 5b. However, it is immediately apparent that this particular nondimensionalization produces no meaningful trends. The notes on llama blood from Figure 5a provide a clue as to why normalization by cube root of cell volume may not be particularly meaningful in the context of erythrocytes. Specifically, the cube root describes the geometry of the cell if it were a perfect sphere. For all erythrocytes, and particularly the elongated ellipsoids of llama, chicken and turkey blood, the cube root underestimates the largest diameter of the red blood cells.

Therefore, it may be more valuable to consider the largest axis of the red blood cells. Figure 6a duplicates the plot of Figure 5a but with cell major axis rather than mean cell volume. The trends are the same for the smallest (goat/sheep) and largest (chicken/turkey) cells. Now, however, the data point for llama blood has shifted significantly along the x-axis, as its major axis is much larger than the cube root of its mean cell volume. A roughly linear relationship between curvature (C) and cell major axis can be observed; the corresponding equation for a linear fit is shown on the plot. This is provided only for observation rather than a physiologically meaningful fit, but overall the results indicate that the geometrical parameters of the cell are important in the relationship between hematocrit and relative viscosity.

The nondimensionalization of tubing diameter and cell geometry from Figure 5b is repeated in Figure 6b with the major cell axis. There is a collapse in data compared to the Figure 5b plot. Based on the comparison between Figure 5 and Figure 6, major cell axis is more closely linked to the relationship between hematocrit and relative viscosity than cell volume.
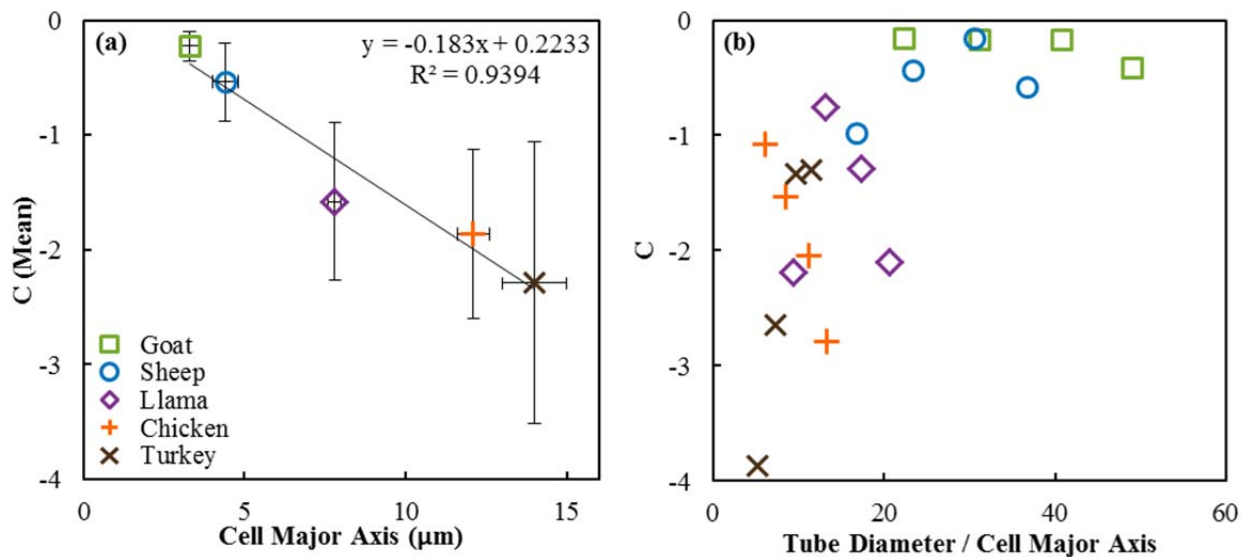

Figure 6. (a) Average values of fitting parameter C versus major axis of the cell for each blood type, with error bars indicating standard deviation of C (vertical bars) and major axis (horizontal bars). A linear fit and corresponding equation is provided. (b) Values of fitting parameter C for all blood types in each tubing diameter versus the ratio of tubing diameter to cell major axis.

71

To reiterate a key point, the difference in comparisons against mean cell volume and major cell axis is the result of the nonspherical nature of both mammalian and avian erythrocytes; for spherical particles, these two measurements would produce identical results. Therefore, the next worthwhile step is an examination of red blood cell shape and its particular effects on flow behavior.

6.2.1 Oblate and prolate particles in flow

Ellipsoid particles are characterized by the ratio of their major and minor rotational axes, defined as their particle aspect ratio (r_p):

$$r_p = \frac{l_a}{l_b} \tag{6.5}$$

As shown in Figure 7, the major rotation axis (l_a) is the axis of rotational symmetry, and l_b is the maximum orthogonal diameter. Perfect spheres have a particle aspect ratio of 1, as all axes are equivalent in length. Spheroids with a particle aspect ratio of less than 1 are defined as oblate. Prolate spheroids have a particle aspect ratio of greater than 1.
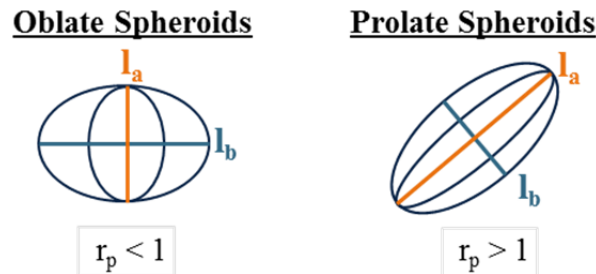
Figure 7. Comparison of axis of rotational symmetry (l_a), orthogonal diameter (l_b) and particle aspect ratio (r_p) for oblate (left) and prolate spheroids (right).

Based on these definitions, the red blood cells in this study can be divided into two general categories: oblate and prolate cells. This is a reasonably accurate description of sheep and goat red blood cells; their erythrocytes are substantially smaller than human red blood cells, and have a more round, less biconcave shape than human RBCs. Describing camelid and avian red blood cells as prolate is a grosser approximation, as all three are flattened in one dimension orthogonal to the major axis, rather than presenting a consistent orthogonal diameter. However, from a purely qualitative perspective, the similarities between suspension flow properties of prolate particles and these ellipsoid blood cells warrant discussion.

The relative viscosity versus hematocrit fitted results for the 73μm and 134μm diameter tubing are shown in Figure 8. In Figure 8a, the fits corresponding to the oblate sheep and goat cells are highlighted, and the ellipsoid llama, chicken and turkey cells are highlighted in the corresponding Figure 8b. This side-by-side comparison provides a visual aid to compare the two types of curves. As is the case with theoretical oblate particles, the relative viscosity of blood containing sheep or goat erythrocytes does display a positive correlation with hematocrit. However, the degree of curvature, or the overall strength of the viscosity-hematocrit relationship, is much less than that observed in the ellipsoidal or prolate cells (Figure 8b). These two trends are still noticeable when the tubing diameter is doubled (Figure 8c,d), but to a lesser extent.

This provides further support for the idea that overall blood viscosity is related to both cell shape and size. However, there is still an obvious outlier – chicken and turkey red blood cells are similar in size and shape, and yet the chicken blood was consistently far more viscous than the turkey blood. If size and shape were the only important parameters, the turkey and chicken blood would be expected to behave similarly. As this is not the case, there is clearly at least one additional critical parameter. The next variable to be addressed is that of red blood cell deformability.

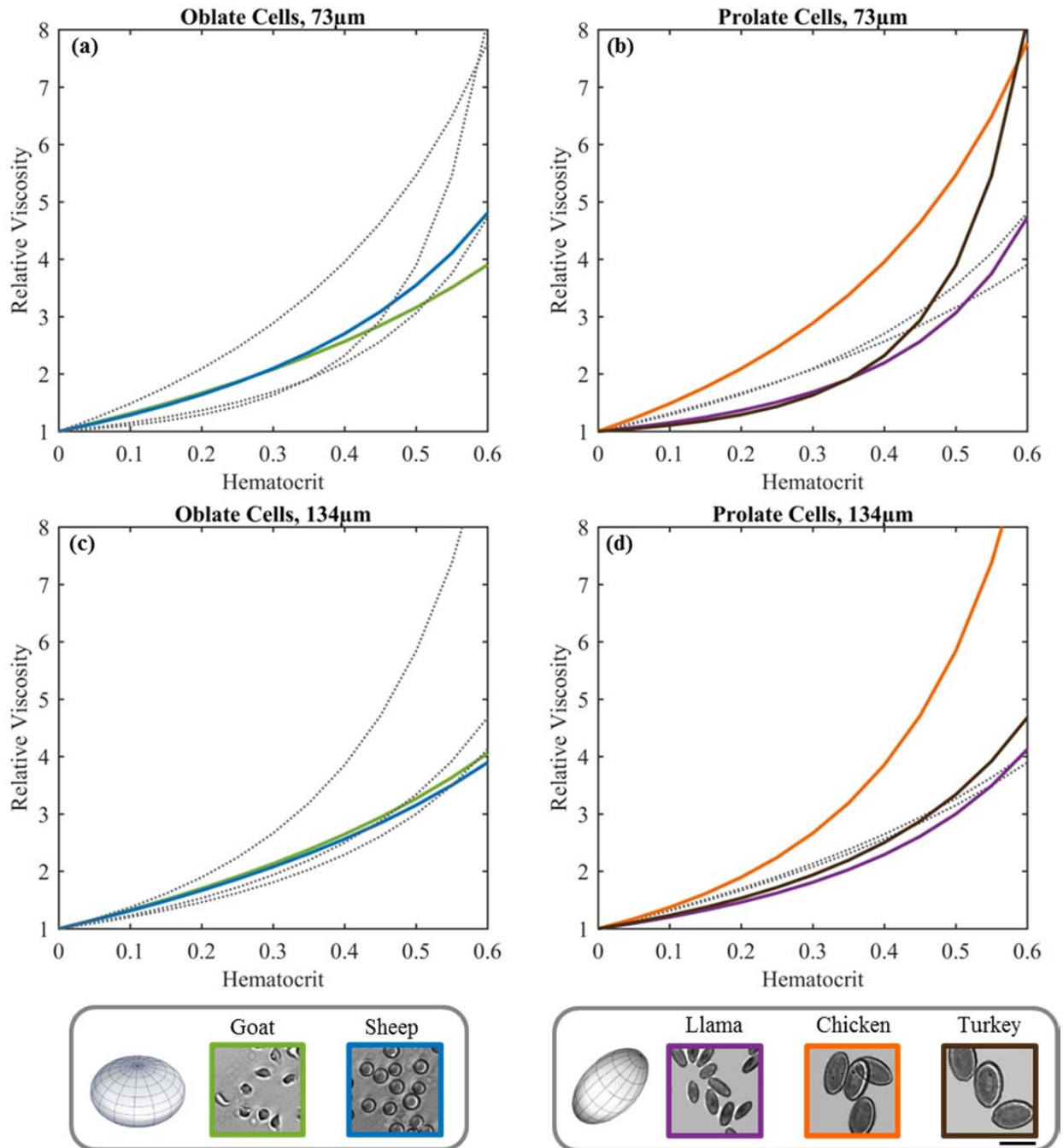Figure 8. Plots of relative viscosity versus hematocrit in (a,b) 73μm diameter tubing and (c,d) 134μm diameter tubing. In both cases, the right and left graphs have identical data, but with the oblate (a,c) and prolate (b,d) data highlighted for discussion purposes.

73

6.3 Role of Cell Deformability

The deformability of red blood cells is a topic of great interest to both the biology and physics communities. Erythrocyte deformation is considered crucial for physiologically-important activities such as oxygen transport to capillary beds and the removal of aged or infected blood cells from circulation by the spleen. Decreased erythrocyte deformability is also associated with increased whole blood viscosity [21]. This section and the subsequent chapter will explore this variable in further detail.

6.3.1 Comparison with theoretical rigid particles

The initial step in investigating the potential role of red blood cell deformability in the relative viscosity of these blood types is an extension of the previous analyses to compare theoretical results from rigid particles to the experimental data.

Equation 6.4 from section 6.1.1 is a functional equation describing the relationship of relative viscosity and volume fraction based on the fitting parameters of maximum packing fraction (ϕ_m) and B, a constant which in the case of spherical particles is the Einstein coefficient. A similar form of the equation was derived by Maron and Pierce [22] in which $B\phi_m = 2$; this version is equally applicable to a wide range of particle aspect ratios, and is a popular choice for analysis of experimental data. Mueller et al [5] used these relationships to derive an empirical fit for data from oblate, spherical and prolate particles and subsequently an equation to calculate the theoretical maximum packing fraction for a particle with a known aspect ratio, applicable for rigid spheroids:

$$\phi_m = \frac{2}{0.321r_p + 3.02} \tag{6.6}$$

The theoretical maximum packing fractions for rigid particles analogous to goat, sheep, pig, llama, chicken and turkey red blood cells were calculated using equation 6.6. These values were then used to generate theoretical relative viscosity versus volume fraction curves using Maron and Pierce's version of equation 6.4. This was repeated for the upper and lower bounds of each red blood cell's dimensions, and the results are plotted in Figure 9 as dotted (average values) and dashed (upper and lower bounds) lines. The corresponding experimental data fits for each tubing diameter were also plotted for comparison. Although the experimental issues with lower hematocrit pig blood prevented the derivation of fitting curves, the 50% hematocrit values were considered valid. The experimental data points at this hematocrit for all flow rates and tubing diameters of pig blood are included for reference in Figure 9c.

The predicted maximum packing fractions for the rigid particles range from $\phi_m \approx 0.52$ (chicken, upper bound) to $\phi_m \approx 0.65$ (pig, lower bound). This is comparable to the literature values found both experimentally and numerically for monodisperse spheres [23, 2]. Pig and sheep blood cells are known to be the most deformable among this set of blood types [20, 24]. The actual pig blood at 50% hematocrit is only 20-30% as viscous as the predicted values for rigid particles (Figure 9c), for which the viscosity is increasing exponentially. The degree of difference is even better illustrated by comparison of the trends for actual sheep blood and rigid particles (Figure 9b). Extrapolation of the data fit from equation 6.1 indicates the possibility of flow up to and past 80% hematocrit before viscosity begins to increase exponentially. This is in good agreement with existing literature regarding the ability of human blood continuing to behave as a fluid at 80% hematocrit [25, 26]. The trends presented here have also been observed for sheep and goat blood in viscometers [27].

74

The ellipsoidal cells reach the point of exponential viscosity increase at lower hematocrit values than the prolate cells. This is true both for the predictions for rigid spheres and the experimental data extrapolated to high hematocrit. However, as with the deformable sheep blood cells, all three elliptical cell types are much less viscous than the rigid approximations. No deformation of llama and other camelid erythrocytes has been observed for typical flow conditions in viscometers. Instead, these erythrocytes align with their major axis parallel to the
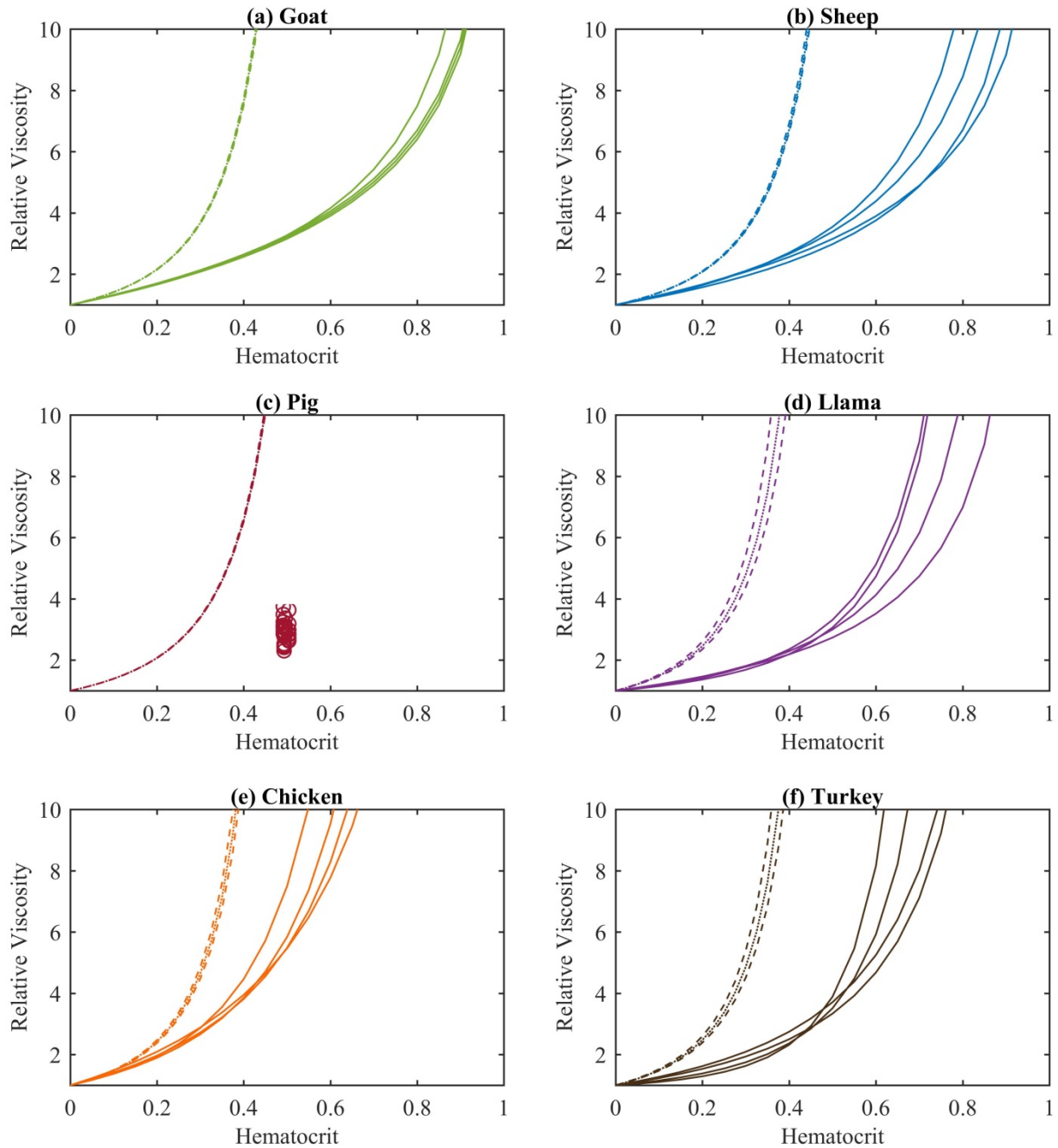

Figure 9. Relative viscosity versus hematocrit by blood type for all tubing diameters (solid lines) in addition to values for analogous rigid particles plotted. Dashed lines represent upper and lower bounds based on the cell maximum and minimum dimensions, and dotted lines are the average values for cell dimensions.

direction of flow [27, 20]. However, the authors of that study noted that the llama and camel erythrocytes were not entirely rigid, as chemical hardening of the cells eliminated their ability to orient parallel to the direction of flow; thus in the small diameter tubing with higher shear rates present in this experiment, the deformability of the llama red blood cells would certainly be an important factor. Turkey red blood cells have the highest degree of observed deformability among the three ellipsoidal cells, with the ability to pass through 2.5-3μm diameter pores [28] and exhibit higher viscosity when chemically hardened [29]. The deformability of chicken red blood cells has been found to vary with specific breed and health status; experiments in polycarbonate sieves with 5μm diameter pores resulted in a range of filtration indices based on these factors [30]. Further comparison of this data with the passage of turkey red blood cells through pores of similar and smaller sizes [29] indicates a greater degree of deformability for the turkey erythrocytes. This can also be observed in comparison of Figure 9e and Figure 9f. Both avian species have a lower viscosity than comparable rigid particles, but the chicken blood is much more similar to its rigid analog, likely indicating a lower degree of deformability.

This comparison shows that all species exhibit some degree of erythrocyte deformability, and that this is, as expected, an important additional contributor to the whole blood viscosity of each species. Unlike cell shape and size, the methods of erythrocyte deformability vary significantly and a direct comparison for all blood types from literature review alone is not possible. Further experiments in this area and additional discussion of measurement and comparison of erythrocyte deformability are presented in Chapter 7.

Works Cited:

[1] A. R. Pries, D. Neuhaus and P. Gaehtgens, "Blood viscosity in tube flow: dependence on diameter and hematocrit," *American Journal of Physiology,* vol. 263, pp. 1770-1778, 1992.

[2] I. R. Rutgers, "Relative viscosity of suspensions of rigid spheres in Newtonian liquids," *Rheologica Acta,* vol. 2, pp. 202-210, 1962a.

[3] I. R. Rutgers, "Relative viscosity and concentration," *Rheologica Acta,* vol. 2, pp. 305-348, 1962b.

[4] D. G. Thomas, "Transport characteristics of suspensions: 8. A note on the viscosity of Newtonian suspensions of uniform spherical particles," *Journal of Colloid Science,* vol. 20, pp. 267-277, 1965.

[5] S. Mueller, E. W. Llewellin and H. M. Mader, "The rheology of suspensions of solid particles," *Proceedings of the Royal Society A,* vol. 466, pp. 1201-1228, 2010.

[6] J. Dupire, M. Socol and A. Viallat, "Full dynamics of a red blood cell in shear flow," *Proceedings of the National Academy of Sciences,* vol. 109, no. 51, pp. 20808-20813, 2012.

[7] R. D. Jäggi, R. Sandoz and C. S. Effenhauser, "Microfluidic depletion of red blood cells from whole blood in high-aspect-ratio microchannels," *Microfluidics and Nanofluidics,* vol. 3, pp. 47-53, 2007.

[8] H. M. Ji, V. Samper, Y. Chen, C. K. Heng, T. M. Lim and L. Yobas, "Silicon-based microfilters for whole blood cell separation," *Biomedical Microdevices,* vol. 10, pp. 251-257, 2008.

[9] A. J. Mach, J. H. Kim, A. Arshi, S. C. Hur and D. Di Carlo, "Automated cellular sample preparation using a Centrifuge-on-a-Chip," *Lab on a Chip,* vol. 11, pp. 2827-2834, 2011.

[10] Y. Nakashima, S. Hata and T. Yasuda, "Blood plasma separation and extraction from a minute amount of blood using dielectrophoretic and capillary forces," *Sensors and Actuators B: Chemical,* vol. 145, pp. 561-569, 2010.

[11] E. Sollier, M. Cubizolles, Y. Fouillet and J.-L. Achard, "Fast and continuous plasma extraction from whole human blood based on expanding cell-free layer devices," *Biomedical Microdevices,* vol. 12, pp. 485-497, 2010.

[12] S. Thorslund, O. Klett, F. Nikolajeff, K. Markides and J. Bergquist, "A hybrid poly(dimethylsiloxane) microsystem for on-chip whole blood filtration optimized for steroid screening," *Biomedical Microdevices,* vol. 8, pp. 73-79, 2006.

[13] X. Tong and K. D. Caldwell, "Separation and characterization of red blood cells with different membrane deformability using steric field-flow fractionation," *Journal of Chromatography B,* vol. 674, pp. 39-47, 1995.

[14] S. Tripathi, A. Prabhakar, N. Kumar, S. G. Singh and A. Agrawal, "Blood plasma separation in elevated dimension T-shaped microchannel," *Biomedical Microdevices,* vol. 15, no. 3, pp. 415-425, 2013.

[15] V. VanDelinder and A. Groisman, "Separation of Plasma from Whole Human Blood in a Continuous Cross-Flow in a Molded Microfluidic Device," *Analytical Chemistry,* vol. 78, pp. 3765-3771, 2006.

[16] W. O. Reece, Dukes' Physiology of Domestic Animals, 13th Ed., Wiley-Blackwell, 2015.

[17] S. M. Azwai, O. E. Abdouslam, S. Al-Bassam, A. M. Al Dawek and S. A. L. Al-Izzi, "Morphological characteristics of blood cells in clinically normal adult llamas (Lama glama)," *Veterinarski Arhiv,* vol. 77, no. 1, pp. 69-79, 2007.

[18] K. Yamaguchi, K. D. Jürgens, H. Bartels and J. Piiper, "Oxygen transfer properties and dimensions of red blood cells in high-altitude camelids, dromedary camel and goat," *Journal of Comparative Physiology B,* vol. 157, pp. 1-9, 1987.

[19] O. K. Baskurt, "Deformability of red blood cells from different species studied by resistive pulse analysis technique," *Biorheology,* vol. 33, no. 2, pp. 169-179, 1996.

[20] J. E. Smith, N. Mohandas and S. B. Shohet, "Variability in erythrocyte deformability among various mammals," *American Journal of Physiology,* vol. 236, no. 5, pp. H725-H730, 1979.

[21] S. Chien, S. Usami, R. J. Delleback and M. I. Gregersen, "Blood viscosity: influence of erythrocyte deformation," *Science,* vol. 157, pp. 827-829, 1967.

[22] S. H. Maron and P. E. Pierce, "Application of Ree-Eyring generalized flow theory to suspensions of spherical particles," *Journal of Colloid Science,* vol. 11, pp. 80-95, 1956.

[23] M. D. Rintoul and S. Torquato, "Computer simulations of dense hard-sphere systems," *Journal of Chemical Physics,* vol. 105, pp. 9258-9265, 1996.

[24] T. M. Amin and J. A. Sirs, "The Blood Rheology of Man and Various Animal Species," *Quarterly Journal fo Experimental Physiology,* vol. 70, pp. 37-49, 1985.

[25] Y. Fung, Biomechanics - Mechanical Properties of Living Tissues, New York: Springer-Verlag, 1993.

[26] H. Goldsmith and V. Turitto, "Rheological aspects of thrombosis and haemostasis: basic principles and applications," *Thrombosis and Haemostasis,* vol. 55, no. 3, pp. 415-435, 1986.

[27] H. O. Stone, H. K. Thompson, Jr. and K. Schmidt-Nielsen, "Influence of erythrocytes on

blood viscosity," *American Journal of Physiology,* vol. 214, no. 4, pp. 913-918, 1968.

[28] M. I. Gregersen, C. A. Bryant, S. Chien, R. J. Dellenback, V. Magazinovic and S. Usami, "Species Differences in the Flexibility and Deformation of Erythrocytes (RBC)," in *5th European Conference on Microcirculation*, Gothenburg, 1968.

[29] S. Usami, V. Magazinovic, S. Chien and M. I. Gregersen, "Viscosity of Turkey Blood: Rheology of Nucleated Erythrocytes," *Microvascular Research,* vol. 2, pp. 489-499, 1970.

[30] S. M. Mirsalimi and R. J. Julian, "Reduced Erythrocyte Deformability as a Possible Contributing Factor to Pulmonary Hypertension and Ascites in Broiler Chickens," *Avian Diseases,* vol. 35, no. 2, pp. 374-379, 1991.

Chapter 7
Cell Deformability

Cell deformability is known to be a critical factor in how particles, vesicles and cells behave in flow. The differences at a particle level have a profound impact at the control volume level, altering the overall flow characteristics of a particle-laden fluid, particularly as the particle to vessel diameter ratio drops below 1:500. One of the most interesting trends from the experimental data was the consistently high viscosity of chicken blood, regardless of hematocrit. This was particularly surprising given the similar size and shape of turkey red blood cells, which had a viscosity similar to mammalian red blood cells, particularly at lower hematocrits. Literature values suggest a higher degree of deformability for turkey red blood cells than chicken red blood cells. However, no study used both types of cells, so comparisons had to be made across studies with differing measurement techniques. Therefore, further investigation of the deformability differences between these cell types was warranted.

7.1   Cell deformability

7.1.1 Background on erythrocyte deformability

Deformability of denucleated erythrocytes depends on three factors: internal viscosity, cell geometry, and properties of the membrane [1]. Internal viscosity of denucleated cells is dominated by hemoglobin concentration [2]. Mean cell hemoglobin increases linearly with mean cell volume for mammalian, avian and reptilian cells despite the additional presence of a nucleus in the latter cell types [3]. As a result, the mean cell hemoglobin concentration for both nucleated and denucleated red blood cells is relatively constant, at around 35% [4]. Cell geometry for human erythrocytes and many other mammalian red blood cells can be defined primarily by surface area to volume ratio. This is applicable to the goat, sheep and porcine red blood cells in the present study. Avian cell geometry is further affected by cytoskeletal elements which create the characteristics ellipsoidal shape [5]. Finally membrane properties have a significant effect on deformability particularly in response to dynamic loads – for mammalian cells, membrane properties are strongly related to cell shape, so changes in cell shape as a response to outside stimuli will be impacted by the membrane elasticity [6]. The marginal and transmarginal bands in avian cells will temper this effect somewhat, but membrane properties are still critical. Nucleated and denucleated red blood cells have a similar deformation process despite these differences in cell characteristics [7].

7.1.2 Deformability measurement techniques

The combination of elastic, viscous and geometric factors makes the measurement of red blood cell deformation a complex and time-consuming process. Extensive reviews of red blood cell deformability measurements are available elsewhere [8, 9]. The most common measurements and brief discussion of their strengths and weaknesses are presented here.

Some measurement techniques use only a small portion of the erythrocyte – many such techniques focus on the cell membrane. In micropipette aspiration, a part of the red blood cell membrane is aspirated into the narrow pipette opening; specific membrane and/or cytoplasm characteristics can thus be determined by controlling or measuring variables such as pressure, degree of aspiration and membrane curvature [10]. Similarly, a portion of the membrane can be passed into a narrow filter or microfluidic channel, and deformability calculated based on the

79

applied pressure, geometry of the filter, and characteristics of the aspirated portion [11]. Atomic force microscopy [12] and optical tweezer [13] techniques provide information about localized deformation of the erythrocyte. These techniques are cost- and labor-intensive, but provide highly quantitative information about the localized deformation. However, extrapolation of this localized information to erythrocyte behavior in flow is generally not possible. This subset of techniques is not a good candidate for comparison of different blood types, as they will not take into account the effects of critical cell characteristics such as ellipsoid versus spheroid geometry and the presence of a nucleus.

These techniques can be scaled up to analyze the deformation of an entire red blood cell in response to non-fluidic physical stimuli (i.e. pipette or microchannel walls). For example, an increase in micropipette diameter permits aspiration of the entire red blood cell [14], and an entire cell, rather than a portion of the membrane, can be deformed with optical tweezers [15]. There are several techniques which make use of filters or micropores to assess red blood cell deformability, analyzing various parameters such as transit time through micropores or percent transmission of a red blood cell suspension. Comparative data can be obtained for cell deformability of different red blood cells (healthy, unhealthy, chemically hardened, etc) from the same animal. However, there has been no success in normalizing this measurement technique for difference in mean cell volume. Therefore, only generally qualitative information on cell deformability can be obtained when using red blood cells from different species [4, 16]. Many variations of microfluidic devices have been designed to measure erythrocyte deformability in this manner. Techniques include measurement of cell perfusion through a capillary-bed type network of microchannels [17], monitoring the pressures required for individual cell passage through narrow constrictions [18], visualization of individual cell deformation in a narrow channel [19]. There is some variation in cost and degree of dificulty of these techniques. Use of optical tweezers for different types of blood cells would provide better comparative data, but is cost- and labor-intensive. However, variations in cell size are the primary issue for most of these techniques – scaling of micropipette, filter, or microchannel sizes will have a significant impact on resulting data.

Finally, there are measurement techniques that focus on red blood cell deformation in response to shear flow. Ektacytometry compares laser diffraction patterns of cells in a viscometer at different shear rates to determine cell dimensions and compute a deformability index [20]. There are contradicting accounts as to whether this technique is useful for nucleated, ellipsoid cells, but some observations of denucleated ellipsoid cells are available [21]. Similarly, rheoscopes measure deformation of individual red blood cells in high shear through direct observation with a microscope [22]. Use of microfluidic devices to study individual cell deformation via high-speed camera is an area of significant recent interest [23]. These techniques provide the most relevant information across red blood cell types in the context of viscosity and pressure drop, but still require specialized equipment, and in the case of analysis of individual blood cells, are highly time-intensive.

Cell deformability is an important parameter both in hemorheology and in practical research areas, such as drug development. There are a great many possible methods to quantify cell deformability, although comparison of results across methods is challenging. Methods to measure individual cells are often the most technically sophisticated, but require repeated trials to determine the deformability of a population of red blood cells with a reasonable degree of certainty. Two experiments were performed to assess how differences in cell deformability would impact the measured viscosity of mammalian and avian blood in small tubes.

80

7.2   Pressure Drop Experiments with Chemically Treated RBCs

The first experiment to investigate the role of cell deformability in the pressure drop measurements was to compare cells with a known deformability to the previously collected data. There are numerous options to alter to the deformability of red blood cells, including heat treatment [24], creation of membrane-only "ghost cells" [25] and through chemical treatment [26, 8]. However, without the ability to quantitatively measure minor or moderate changes in deformability, the obvious choice was to impose complete rigidity on the red blood cells. This can be achieved in red blood cells through chemical treatment with glutaraldehyde, resulting in complete fixation of the cytoplasm [19, 27, 28]. The sheep blood was selected for this purpose based on its denucleated, consistent shape (oblate spheroid) and ease in acquisition and handling.

7.2.1 Protocol

Washed and pooled sheep red blood cells (#7249008, Lampire Biological Laboratories) were treated with 1% v/v glutaraldehyde (CAS 11-30-8, Sigma-Aldrich) for ten minutes with stirring [27]. The cells were washed twice with 1x phosphate buffered saline (PBS). 10%, 30% and 50% hematocrit solutions were prepared, and pressure drop of these solutions in 73μm, 102 μm and 134 μm diameter PEEK tubing was measured with the same protocol as described in Chapter 3. The results were compared to data from normal sheep erythrocytes collected previously.

Hematocrit measurement by packed cell volume is known to be accurate and consistent for red blood cells with differing characteristics at the concentrations used in this study [21, 29]. However, hematocrit measurement via centrifugation relies on close-packing of cells at the bottom of the capillary measurement tube. Rigid cells have a much lower packing rate than deformable cells of the same size and shape – for example, packing for human red cells is generally observed to be at a hematocrit of 97-98%, whereas hardening of cells decreases this value to around 60% [4]. This results in a higher level of trapped plasma, and as a result hematocrit is over-predicted; at a single packed cell volume (PCV) for cells of identical size and shape, the sample with rigid cells will have fewer overall cells per volume than the deformable cell sample, and thus a lower true hematocrit. This deviation rapidly becomes meaningful as hematocrit increases. This bias can be avoided by using a laboratory cell counter for hematocrit measurement, but this apparatus was not available for this experiment. Alternatively, a correction to the true hematocrit can be made using the ratio of the maximum packing volume of rigid versus deformable cells [30]. The maximum packing fraction for rigid sheep cells determined via the Maron-Pierce equation in 6.3.1 was 0.65, which is in good agreement with literature values for similar cell types [31]. The maximum packing fraction of deformable sheep cells is 97% [21]. The hematocrits calculated via packed cell volume were thus converted to approximate true hematocrit values (Table 1).

Table 1. Original hematocrit values calculated via packed cell volume method and converted hematocrit adjusted by maximum packing fraction of rigid sheep cells (oblate spheroids)

Hct via PCV	Calculated Hct
10%	6.6%
30%	19.8%
50%	32.9%

81

Effective viscosity was calculated using the Weissenberg-Rabinowitsch correction described previously (Chapter 5, Section 5.2.1), and the values used to determine viscosity relative to the suspending fluid (PBS).

7.2.2 Results

The 50% hematocrit solutions were problematic. In the 73μm PEEK tubing, the pressure drop for flow rates above 300μl/hr was outside the measurable range of the pressure transducer (>103.4 kPa). At lower flow rates, only clear fluid (PBS) emerged from the tubing and the measured pressure was quite high (~67 kPa at 50μl/hr), indicating that the rigid erythrocytes were being filtered out upstream of the outlet. Further examination showed jamming of the
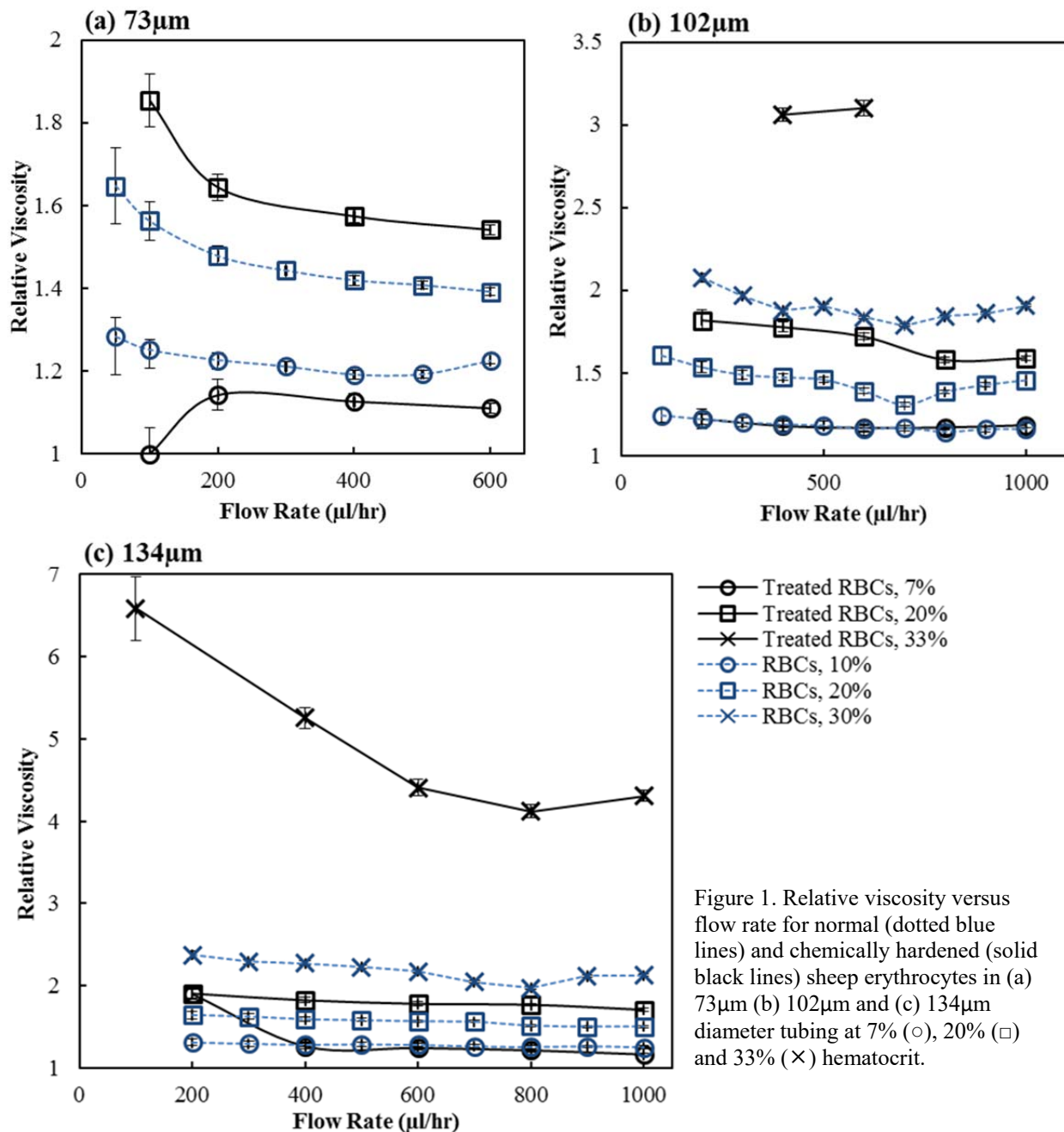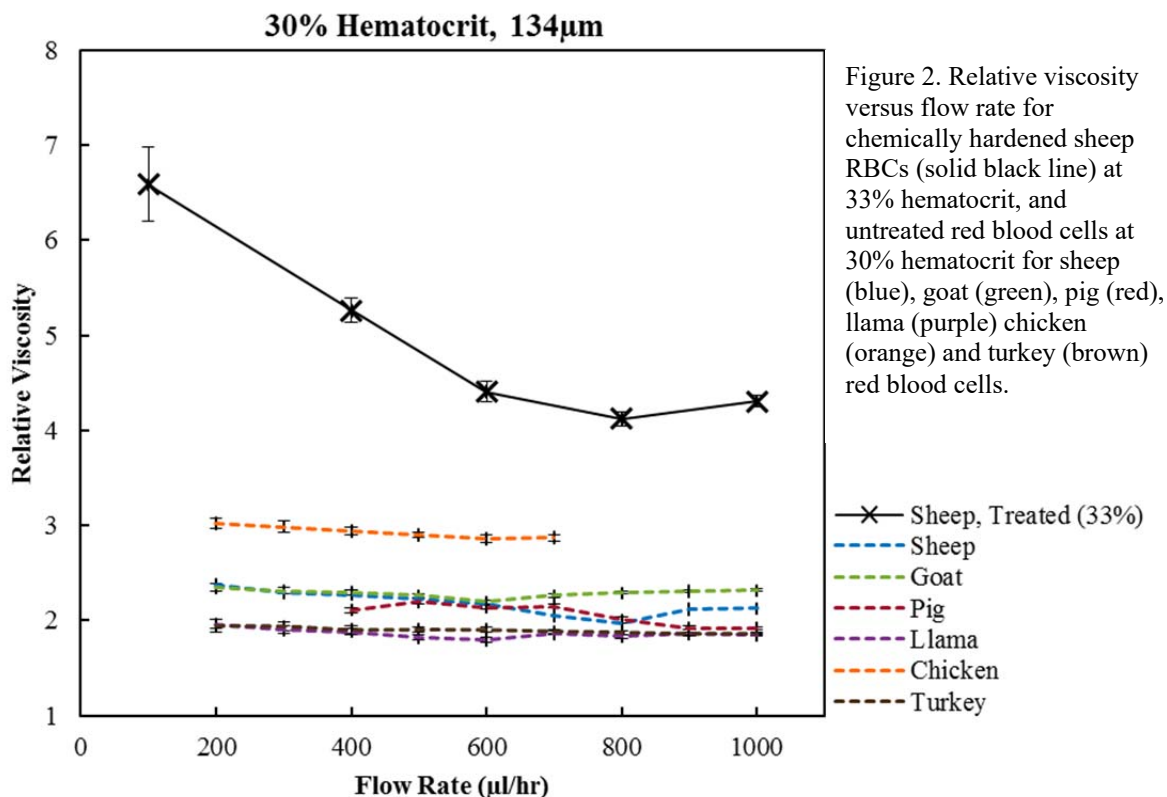

Figure 1. Relative viscosity versus flow rate for normal (dotted blue lines) and chemically hardened (solid black lines) sheep erythrocytes in (a) 73μm (b) 102μm and (c) 134μm diameter tubing at 7% (○), 20% (□) and 33% (×) hematocrit.

82

particles at the tubing inlet. This issue occurred regardless of the initial flow rate used. In the 102μm diameter PEEK tubing, blood at only two flow rates was collected (400 and 600μl/hr). Subsequent attempts at data collection resulted in clogging and wildly fluctuating pressure drop measurements. In the 134μm diameter PEEK tubing, issues with clogging, even at very low flow rates, were alleviated by decreasing the tubing length from 40cm to 10cm. Two complete sets of data were collected in this manner, with an additional 2 data points (200 and 400μl/hr) collected for a third data set before the supply of blood was exhausted. Therefore, results from the full range of hematocrits were available only for the 134μm diameter tubing (Figure 1).

At low hematocrit (7-10%), the relative viscosities of treated and untreated cells are nearly identical (Figure 1). In the smallest tubing diameter (73μm), the plotted sheep blood data has a higher relative viscosity than the treated blood, but the relative difference is quite small and attributable to the difference in hematocrit (6.6% versus 10%). This outcome is in agreement with the observations about all six blood types at very low hematocrit (Chapter 6, Figure 4) – in this dilute range, the properties of the suspending fluid dominate flow behavior, and the suspended cells have little impact on viscosity regardless of their characteristics.

As hematocrit increases to 20%, the relative viscosity of the rigid cell suspensions rises compared to the original sheep blood data. The difference is small but noticeable, with the rigid cells causing a ~10% increase in relative viscosity.

Finally, at 30% hematocrit the rigid blood cells induce a significantly higher viscosity than the unaltered blood across all flow rates (Figure 1c), ranging from 1.5 to 2.5 times greater than the original sheep blood. The issues experienced when attempting to collect this in the smaller tubing diameters further supports this large increase in viscosity. This increase in hematocrit was so large that the relative viscosity for hardened sheep cells was more than 30-100% larger than any of the tested blood types (Figure 2).

Figure 2. Relative viscosity versus flow rate for chemically hardened sheep RBCs (solid black line) at 33% hematocrit, and untreated red blood cells at 30% hematocrit for sheep (blue), goat (green), pig (red), llama (purple) chicken (orange) and turkey (brown) red blood cells.

83

7.2.3 Conclusions

The "standard" deformability of sheep cells varies depending on measurement technique. Overall, they are found to be less deformable than most mammalian erythrocytes, including human and porcine red blood cells, and more deformable than goat red blood cells [4, 24, 20]. Alteration of the moderately deformable sheep erythrocytes significantly impacted the experimental results. Cell deformability plays a dominant role in blood viscosity, and its effects can be measured in this relatively simple experimental setup. These results invite further exploration of the effects of cell deformability via pressure drop measurements in narrow tubes. The potential ability to confer meaningful information about the deformability of a population of red blood cells in a straightforward and cost-effective manner has potential value in a variety of applications ranging from basic fluid dynamics research to drug screening.

The potential value of this avenue of research is a departure from the time and labor-intensive processes for existing red blood cell deformability measurement techniques. However, further research in this area would also require access to those techniques as a basis for quantitative understanding of pressure drop results. As lack of resources and access were the barrier to quantifying cell deformability in the present experiment, this interesting pursuit is best left to future researchers.

These results support the hypothesis that the significant differences in measured viscosity between chicken and turkey blood despite their similar cell geometries is a consequence of differing cell deformability. To further test this hypothesis, a method for qualitative comparison of cell deformability within the context of available lab resources was identified.

7.3   Flow through a Constriction

Flow through a microfluidic constriction was used to compare cell deformability between sheep, turkey and chicken red blood cells. First, the difference in particle migration for rigid versus deformable red blood cells was assessed through measurement of the cell-free layer downstream of a microfluidic contraction using glutaraldehyde-treated sheep red blood cells. Then, untreated turkey and chicken red blood cells were also analyzed in the microfluidic device, and the results used to draw conclusions regarding the difference in erythrocyte deformability between these blood samples.

7.3.1 Literature review

Researchers from Harvard University developed a flow focusing microfluidic device for the purposes of plasma separation from whole blood, based on the principle of cell-free layer formation by deformable particles (red blood cells) [27]. Briefly, flow in a 100μm wide microchannel is interrupted by a long, narrow constriction (Figure 3). Rigid particles proceeding through the constriction return to an identical downstream position. Conversely, deformable particles or cells will occupy a downstream position further from the wall than prior to the constriction. When multiple cells are present, the overall effect is an enhancement of the downstream cell-free layer for deformable cells.
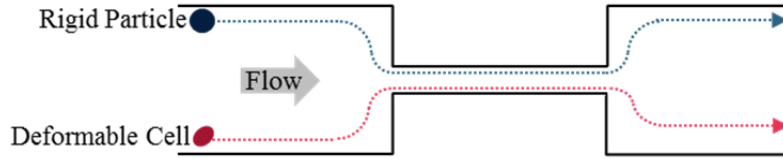
84

Figure 3. Illustration of rigid and deformable particle passage through a microfluidic constriction

The authors tested the microfluidic device with rigid particles and both normal and chemically hardened human red blood cells. They also compared the effects of geometry at the flow constriction, changes in cell volume, hematocrit, and flow rate. The cell-free layer was enhanced primarily by increased cell deformability, increased cell volume and increased hematocrit (from 0.1% to 2.6%). Increasing the length and decreasing the width of the constriction geometry also increased the relative size of the downstream cell-free layer. The constriction geometry with the maximum cell-free layer size for a 100μm wide, 75μm deep channel had a length of 300μm and width of 25μm. At this geometry, the width of the red blood cell distribution downstream (h_{out}) of the flow relative to the upstream (h_{in}[1]) distribution ranged from 0.7 to 0.8 depending on flow rate. They also found that the enhanced cell-free layer was stable for a significant distance (1 cm ≈ 100 channel widths) downstream of the constriction.

Their studies with regular and hardened red blood cells demonstrate the usefulness of this system as a way to compare cell deformability. The experimentally observed results for healthy and hardened red blood cells in a device with a 300μm long constriction are reported in Table 2. Solid beads were tested only in devices with a 200μm long constriction. The authors ultimately leveraged this device to pull plasma from the enhanced cell-free layer zones. However, for the purposes of the present thesis research, the capability of inferring differences in cell deformability from simple flow visualization without the use of specialized equipment is a worthwhile technique on its own.

Table 2. Relative width of downstream and upstream red blood cell distributions from Faivre et al [27].

Particle	h_{out}/h_{in}
Solid Beads	1.0
Healthy RBCs	0.75
Hardened RBCs	0.9

A similar study was performed using a stenosed microchannel [28] with both normal and chemically treated red blood cells at 10-20% hematocrit. The authors traced the trajectories of individual cells and tracer particles in a 50μm-wide microchannel interrupted by a single 35μm wide, 30μm long stenosis on one wall of the channel. As in the constriction study, rigid tracer particles maintained an identical distance from the wall both upstream and downstream of the stenosis. Untreated red blood cells had asymmetric streamlines corresponding to an enhanced cell-free layer after the stenosis. Chemical hardening of the red blood cells with glutaraldehyde significantly decreased this asymmetry. The authors concluded that the formation of a downstream cell-free layer was a result of cell deformability.

---

[1] The nomenclature in this thesis differs from that used in the article.

7.3.2 *Rigid particles*

Microfluidic channels were fabricated via traditional soft lithography, and PDMS devices plasma bonded to glass slides. The geometric parameters of the devices are listed in Table 3. The constriction geometry was selected based on the results from Faivre et al [27] to produce the greatest enhancement of cell-free layer.

Table 3. Geometry of flow-focusing device

Parameter	Size (μm)
Constriction Width (W1)	25
Constriction Length (L)	300
Channel Width (W2)	100
Channel Depth	55

The device was first tested with solid particles (Cat. No. 35-3 Fluorescent Polymer Microspheres, Duke Scientific Corporation) to establish a baseline for rigid spheres and compare results to the original work [27]. The microspheres were composed of polystyrene divinylbenzene with a 10μm mean diameter and 13% size uniformity. Beads were suspended in 60% w/w aqueous glycerol at a 2.6% volume fraction, with flow driven by a syringe pump at a rate of 20μl/hr. Flow was observed with an Olympus IX70 epifluorescent microscope, and 960 by 1280 pixel images were recorded by a Stingray F145 camera at 15 fps. The image processing capabilities of Matlab were used to overlay sequences of 4 to 25 images and measure the upstream and downstream cell-free layers. An example of a single particle moving through the channel is shown in Figure 4a, showing four images from a 17-image sequence. The blue arrows identify the location of the particle as it moves through the device. Figure 4b shows the full 17-image sequence post-processing. Rigid particles consistently returned to the same lateral position post-constriction, with no cell-free layer enhancement.
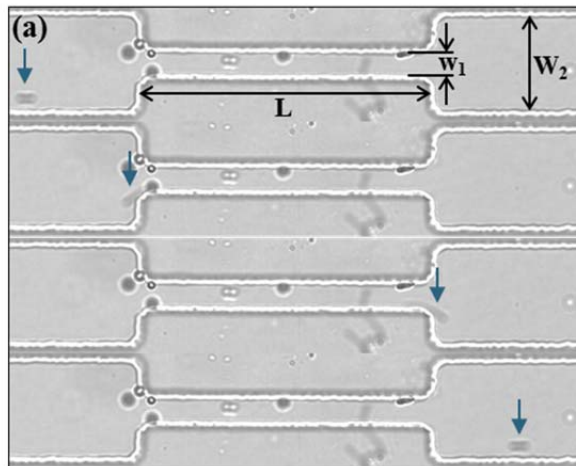
Figure 4. (a) A single 10μm sphere flows downstream from a 100μm wide channel (W2) through a 25μm (w1) constriction. Blue arrows indicate the location of the particle frame by frame. Sequence represents 4 non-contiguous frames of a 17-image sequence. (b) Post-processing overlay of the same rigid particle showing return to original position (red line) downstream of the constriction. 100μm scale bar.

المنارة للاستشارات

www.manaraa.com
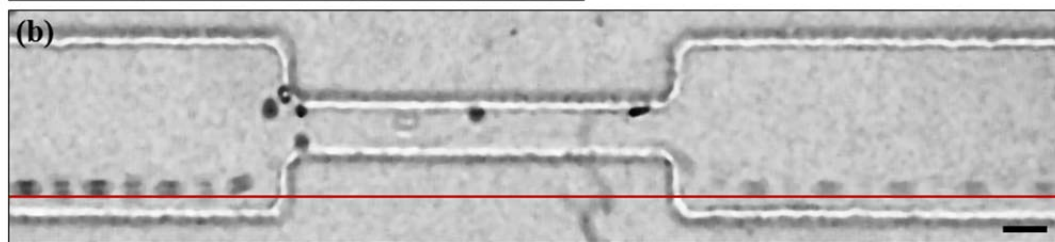
The results from the rigid particles confirm that the device is performing as expected and the available equipment is sufficient to continue the experiment with red blood cells.

7.3.3 Comparison of red blood cells

Washed, pooled sheep (#7249008, Lampire Biological Laboratories), chicken (#7241408, Lampire Biological Laboratories) and turkey red blood cells (#7249408, Lampire Biological Laboratories) suspended in Alsevers were acquired and used within 5 days of arrival. Blood was diluted to 2.6% hematocrit with 1x phosphate buffered saline, and samples examined microscopically to verify that no hypotonic or hypertonic deformation had occurred as a result of dilution. Suspensions of chemically treated red blood cells of each blood type were also prepared. Each type of blood was treated with 1% v/v glutaraldehyde (CAS 11-30-8, Sigma-Aldrich) for ten minutes with stirring [27]. The cells were washed twice with 1x phosphate buffered saline (PBS) and then diluted to 2.6% hematocrit.

Flow rates ranged from 20μl/hr to 200μl/hr. Issues with sedimentation within the syringe and tubing and clogging at the constriction inlet lead to optimization of a specific flow rate protocol. Devices were filled past the constriction at a rate of 20μl/hr. The flow was immediately increased to 100μl/hr. Images were collected for this entire process, but only images at 100μl/hr were used for analysis.

The upstream and downstream red cell distributions were measured using a similar process as described in Section 7.2.2. Briefly, 10-image sequences were combined in Matlab using the overlay difference technique to create a composite image of the flow (Figure 5). Upstream and downstream red cell distributions were measured in Photoshop. Multiple sequences were composited and measured for each blood type. Measurement uncertainty was found to be ±5 pixels.
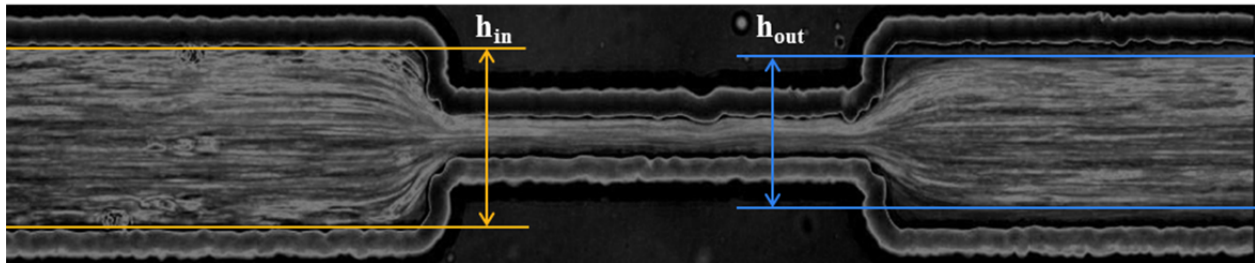
Figure 5. Example of measurement of upstream and downstream red cell distributions. The image is a composite of a sequence from the turkey blood in the constriction device.

The ratios of downstream and upstream red cell distributions are shown in Figure 6. Chemical treatment of the sheep erythrocytes resulted in only a slight increase in the cell-free layer, and this difference was negligible in some sequences. The ratio for normal chicken erythrocytes was 0.93 versus 0.99 for chemically treated cells. The untreated turkey red blood cells had the lowest ratio (0.83) of all tested cell types. This corresponds to a downstream cell-free layer of approximately 8.5μm. Treated turkey erythrocytes had the same ratio as the treated sheep and chicken erythrocytes.

Figure 6. Ratio of outlet cell distributions to inlet cell distributions (h_{out}/h_{in}) for normal (dotted) and chemically hardened (solid) sheep, chicken and turkey red blood cells. Left: Full scale plot. Right: Enhanced view of region of interest.
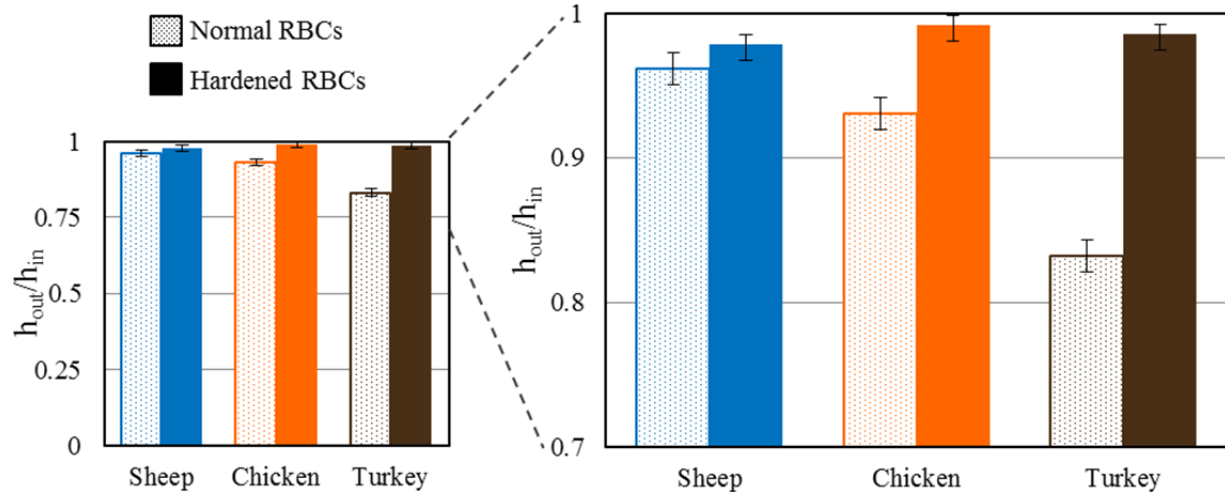
These results compare favorably with the values from the original experiment [27], listed in Table 2. The h_{out}/h_{in} ratio for healthy human red blood cells was 0.75, much lower than the results for healthy sheep, chicken and turkey red blood cells. The differences in both cell size and deformability make it difficult to draw quantitative conclusions about deformability alone across the three species, but it is possible to provide general context for the results. The sheep cells are smaller and less deformable than human cells; as discussed in Chapter 2.2.1, both of these characteristics will cause sheep cells to experience a lesser migration force than a human cell at the same distance from the channel wall. Likewise, although the chicken and turkey erythrocytes are much larger than human cells, they are less deformable.

The comparison of chicken and turkey data is much more interesting, and indeed the point of carrying out this subset of experiments. The two are similar in size and shape, with turkey cells being slightly larger in major axis length and mean cell volume. The large difference in the resulting cell-free layer for the healthy cells compared to the nearly identical and minimal cell-free layer enhancement for hardened cells suggests that the chicken red blood cells are less deformable than turkey erythrocytes. This data, when combined with literature resources on the deformability of the two types of red blood cells, suggests that the high viscosity of the chicken blood (Chapter 5 & 6) relative to the turkey blood can be attributed to differences in deformability.

7.4 Conclusions

Erythrocyte deformability is known to be a key factor in blood viscosity. Measurement of red blood cell deformability is generally complex and time-intensive, and it is problematic to directly compare the results of different measurement types. This is due in part to the fact that several different factors – internal viscosity, cell shape, membrane deformability – contribute to the overall cell deformability, and measurement techniques have a bias towards some subset of these factors. There were still unexplained variations in blood viscosity from the experimental data after accounting for differences in cell size and shape, and cell deformability was the most important factor yet to be addressed. Direct measurement of the cell deformability for each blood type was not a possibility due to the aforementioned issues with existing measurement techniques in conjunction with lack of available resources to perform such measurements.

88

Therefore, two sets of experiments were performed to investigate how deformability influenced the pressure drop data and compare the deformability of chicken and turkey red blood cells. The results indicate that the high viscosity of chicken blood may be partially influenced by low cell deformability.

Works Cited:

[1] S. M. Mirsalimi and R. J. Julian, "Reduced Erythrocyte Deformability as a Possible Contributing Factor to Pulmonary Hypertension and Ascites in Broiler Chickens," *Avian Diseases,* vol. 35, no. 2, pp. 374-379, 1991.

[2] A. R. Williams and D. R. Morris, "The Internal Viscosity of the Human Erythrocyte May Determine Its Lifespan in Vivo," *Scandinavian Journal of Haematology,* vol. 24, pp. 57-62, 1980.

[3] C. M. Hawkey, P. M. Bennett, S. C. Gascoyne, M. G. Hart and J. K. Kirkwood, "Erythrocyte size, number and haemoglobin content in vertebrates," *British Journal of Haematology,* vol. 77, no. 3, pp. 392-397, 1991.

[4] M. I. Gregersen, C. A. Bryant, S. Chien, R. J. Dellenback, V. Magazinovic and S. Usami, "Species Differences in the Flexibility and Deformation of Erythrocytes (RBC)," in *5th European Conference on Microcirculation*, Gothenburg, 1968.

[5] P. Agre and J. C. Parker, Red Blood Cell Membranes: Structure, Function, Clinical Implications, CRC Press, 1989.

[6] R. M. Hochmuth and R. E. Waugh, "Erythrocyte membrane elasticity and viscosity," *Annual Review of Physiology,* vol. 49, pp. 209-19, 1987.

[7] P. Gaehtgens, G. Will and F. Schmidt, "Comparative Rheology of Nucleated and Non-Nucleated Red Blood Cells," *Pflügers Archiv,* vol. 390, pp. 283-287, 1981.

[8] S. Chien, "Red cell deformability and its relevance to blood flow," *Annual Review of Physical Chemistry,* vol. 49, pp. 177-192, 1987.

[9] M. Musielak, "Red blood cell-deformability measurement: review of techniques," *Clinical Hemorheology and Microcirculation,* vol. 42, no. 1, pp. 47-64, 2009.

[10] E. A. Evans and P. L. La Celle, "Intrinsic material properties of the erythrocyte membrane indicated by mechanical analysis of deformation," *Blood,* vol. 45, no. 1, pp. 29-43, 1975.

[11] R. F. Baker, "Membrane deformability of metabolically depleted human red cells," *Blood Cells,* vol. 7, pp. 551-558, 1981.

[12] M. Fornal, M. Lekka, G. Pyka-Fościak, K. Lebed, T. Grodzicki, B. Wizner and J. Styczeń, "Erythrocyte stiffness in diabetes mellitus studied with atomic force microscope," *Clinical Hemorheology and Microcirculation,* vol. 7, no. 12, pp. 273-276, 2006.

[13] S. Hénon, G. Lenormand, A. Richert and F. Gallet, "A new determination of the shear modulus of the human erythrocyte membrane using optical tweezers," *Biophysical Journal,* vol. 76, no. 2, pp. 1145-1151, 1999.

[14] P. L. LaCelle and B. D. Smith, "Biochemical factors influencing erythrocyte deformability and capillary entrance phenomena," *Scandinavian Journal of Clinical and Laboratory Investigation,* vol. 156, pp. 145-149, 1981.

[15] J. Guck, R. Ananthakrishnan, H. Mahmood, T. J. Moon, C. C. Cunningham and J. Käs, "The optical stretcher: a novel laser tool to micromanipulate cells," *Biophysical Journal,*

vol. 81, no. 2, pp. 767-784, 2001.

[16] O. K. Baskurt, "Deformability of red blood cells from different species studied by resistive pulse analysis technique," *Biorheology,* vol. 33, no. 2, pp. 169-179, 1996.

[17] S. S. Shevkoplyas, T. Yoshida, S. C. Gifford and M. W. Bitensky, "Direct measurement of the impact of impaired erythrocyte deformability on microvascular network perfusion in a microfluidic device," *Lab on a Chip,* vol. 6, pp. 914-920, 2006.

[18] Q. Guo, S. J. Reiling, P. Rohrbach and H. Ma, "Microfluidic biomechanical assay for red blood cells parasitized by Plasmodium falciparum," *Lab on a Chip,* vol. 12, pp. 1143-1150, 2012.

[19] J. C. A. Cluitmans, V. Chokkalingam, A. M. Janseen, R. Brock, W. T. S. Huck and G. J. C. G. M. Bosman, "Alterations in Red Blood Cell Deformability during Storage: A Microfluidic Approach," *BioMed Research International,* vol. 2014, pp. 1-9, 2014.

[20] J. E. Smith, N. Mohandas and S. B. Shohet, "Variability in erythrocyte deformability among various mammals," *American Journal of Physiology,* vol. 236, no. 5, pp. H725-H730, 1979.

[21] H. O. Stone, H. K. Thompson, Jr. and K. Schmidt-Nielsen, "Influence of erythrocytes on blood viscosity," *American Journal of Physiology,* vol. 214, no. 4, pp. 913-918, 1968.

[22] H. Schmid-Schönbein, P. Gaehtgens, T. Fischer and M. Stöhr-Liesen, "Biology of red cells: non-nucleated erythrocytes as fluid drop-like cell fragments," *International Journal of Microcirculation: Clinical & Experimental,* vol. 3, no. 2, pp. 161-196, 1984.

[23] J. Dupire, M. Socol and A. Viallat, "Full dynamics of a red blood cell in shear flow," *Proceedings of the National Academy of Sciences,* vol. 109, no. 51, pp. 20808-20813, 2012.

[24] T. M. Amin and J. A. Sirs, "The Blood Rheology of Man and Various Animal Species," *Quarterly Journal fo Experimental Physiology,* vol. 70, pp. 37-49, 1985.

[25] P. A. Aarts, S. A. van den Broek, G. W. Prins, G. D. Kuiken, J. J. Sixma and R. M. Heethaar, "Blood platelets are concentrated near the wall and red blood cells in the center in flowing blood," *Arteriosclerosis, Thrombosis and Vascular Biology,* vol. 8, pp. 819-824, 1988.

[26] S. Chien, S. Usami, R. J. Delleback and M. I. Gregersen, "Blood viscosity: influence of erythrocyte deformation," *Science,* vol. 157, pp. 827-829, 1967.

[27] M. Faivre, M. Abkarian, K. Bickraj and H. A. Stone, "Geometrical focusing of cells in a microfluidic device: An aproach to separate blood plasma," *Biorheology,* vol. 43, pp. 147-159, 2006.

[28] H. Fujiwara, T. Ishikawa, R. Lima, N. Matsuki, Y. Imai, H. Kaji, M. Nishizawa and T. Yamaguchi, "Red blood cell motions in high-hematocrit blood flowing through a stenosed microchannel," *Journal of Biomechanics,* vol. 42, no. 7, pp. 838-843, 2009.

[29] B. S. Bull and K. L. Hay, "Is the Packed Cell Volume (PCV) Reliable?," *Laboratory Hematology,* vol. 7, pp. 191-196, 2001.

[30] O. K. Baskurt, M. R. Hardeman and M. W. Rampling, Handbook of Hemorheology and Hemodynamics, IOS Press, 2007.

[31] S. Mueller, E. W. Llewellin and H. M. Mader, "The rheology of suspensions of solid particles," *Proceedings of the Royal Society A,* vol. 466, pp. 1201-1228, 2010.

90

Chapter 8
Conclusions

8.1   Summary

The viscosity of whole blood in microscale vessels (73-161μm diameter) has been investigated, with a focus on how differing red blood cell characteristics impact the overall flow behavior. This is the first known study to assess viscosity of different vertebrate blood types in arteriole-sized tubing (30-300μm range). Data was collected for whole blood from four mammals (goat, sheep, pig, llama) and two birds (chicken, turkey) at 0% (homologous plasma) to 50% hematocrit. Blood cell sizes ranged from 3.3μm diameter discocytes (goat) to 12 x 8μm elliptical turkey cells. The aggregation of the pig blood made collection of reliable data highly challenging, and ultimately only the plasma viscosity and 50% hematocrit data were considered useable.

An increase in hematocrit resulted in an increase in relative blood viscosity for all species. The chicken blood had the highest relative viscosity at all hematocrits in all tubing diameters. The elliptical llama and turkey red blood cells had the lowest relative viscosities at low hematocrit, but had a higher rate of increase than either the sheep or goat blood. These trends are similar to those observed for oblate and prolate particles at differing volume fractions. There was a correlation between cell geometry and the dependence of relative viscosity on hematocrit. The major cell axis length was a better indicator of hematocrit-dependence than cell volume, with relative viscosity increasing more quickly with increasing cell axis.

The significant difference in relative viscosity between chicken and turkey blood, despite similar geometric characteristics, required additional research. Existing research suggests that chicken erythrocytes are less deformable than turkey erythrocytes, but the data come from studies with slightly different measurement techniques. Two additional experiments were performed. The first was to assess the sensitivity of the measurement system to major changes in cell deformability. The second was to qualitatively compare the deformability of turkey and chicken red blood cells using flow visualization in a microfluidic constriction.

Pressure drop data were collected for glutaraldehyde-treated sheep red blood cells at 10%, 30% and 50% hematocrit (6%, 19% and 33% when scaled by maximum packing for rigid cells) in three tubing diameters. The relative viscosity of the hardened cell suspensions was larger than that of the normal sheep red blood cells, particularly at the largest measured hematocrit. At 33% hematocrit, the relative viscosity of the rigid sheep cells was 130-200% that of any other untreated blood type (sheep, goat, pig, llama, chicken, turkey). This indicates that the system is sensitive to large increases in cell deformability, and that this effect could potentially be responsible for the high relative viscosity of the chicken blood.

Qualitative comparison of chicken and turkey red blood cell deformability was performed via flow through a microfluidic constriction. The cell-free layer is known to increase downstream of the constriction for deformable particles, an effect which increases with increasing deformability. The results align with literature values to indicate that turkey red blood cells are more deformable than chicken red blood cells. This result, in conjunction with the preceding experiment, strongly suggests that the difference in viscosity between chicken and turkey blood is due to a difference in deformability.

These results were similar to previous research measuring the viscosities of different vertebrate blood types in larger tubing and viscometers. Viscosity of sheep and goat blood had

91

the lowest hematocrit-dependence for the range of hematocrits measured, as in [1]. Llama had a very low relative viscosity at low hematocrit, but relative viscosity increased more rapidly with hematocrit than for goat and sheep blood, as in [2]. The data suggest that chicken erythrocytes are less deformable than turkey erythrocytes ([3] and [4]).

Blood viscosity is influenced by a combination of cell characteristics, as well as other factors such as aggregation not studied here. The differences in blood viscosity across vertebrate types are worth additional consideration in the context of the large number of hemorheological studies focusing only on human blood. Researchers selecting animal models for trials of implantable microdevices or using non-human blood for benchtop studies should consider how the selected blood differs from human blood. This may include referencing existing studies, including this one. The described experimental apparatus requires only off-the-shelf components available from common laboratory suppliers (DigiKey, Cole-Parmer, etc), is easily customizable based on desired channel and flow characteristics, and is time-effective when only a few variables are to be studied. It is therefore a useful, inexpensive tool to analyze how selection of a specific blood type and hematocrit will impact fluid behaviors in microchannels of known size.

8.2 Future Directions

The study of blood flow is an extensive field, even when focusing solely on human blood. This is a single foray into how different vertebrate blood behaves in microscale channels. There is, therefore, a wide range of possibilities for future research. Study in smaller channels (12-73µm) would be particularly interesting as the ratio of cell and channel size begins to approach 1. Based on experiments in 25µm diameter tubes, modifications to the experimental setup would be necessary to improve the transition between the pressure transducer and small tubing entrance. Similar modifications would also be useful to more extensively study the role of aggregation among different animal cells at this size range. Analysis of a wider range of cell characteristics through the use of different blood types (reptilian, etc.) would also be of value.

However, the most practical and interesting future direction is continuing study on how deformability impacts pressure drop in this regime. Initially this would require access or collaboration to directly measure erythrocyte deformability and compare with pressure drop. The initial tests in sheep blood are promising, however, and this may eventually be a viable methodology to assess deformability of a population of red blood cells in a timely, cost-effective manner.

Works Cited:

[1] S. Usami, S. Chien and M. I. Gregersen, "Viscometric characteristics of blood of the elephant, man, dog, sheep and goat," *American Journal of Physiology,* vol. 217, no. 3, pp. 884-890, 1969.

[2] H. O. Stone, H. K. Thompson, Jr. and K. Schmidt-Nielsen, "Influence of erythrocytes on blood viscosity," *American Journal of Physiology,* vol. 214, no. 4, pp. 913-918, 1968.

[3] M. I. Gregersen, C. A. Bryant, S. Chien, R. J. Dellenback, V. Magazinovic and S. Usami, "Species Differences in the Flexibility and Deformation of Erythrocytes (RBC)," in *5th European Conference on Microcirculation*, Gothenburg, 1968.

[4] S. M. Mirsalimi and R. J. Julian, "Reduced Erythrocyte Deformability as a Possible Contributing Factor to Pulmonary Hypertension and Ascites in Broiler Chickens," *Avian Diseases,* vol. 35, no. 2, pp. 374-379, 1991.

Appendix A

## OM2-161 & OM2-8608 Calibration Procedure

Signal Amplification and Conditioning with OM2-161 Strain Gage Signal Conditioners on OM2-8608 Backplane

| Terminal Block (8608) Pin	Edge Connector Pin (OM2-161 Pin)	Description	Jumper Wire via Dip Switch on 8608 Backplane
1	C & 3	- 15 V	
2	D	+ Remote Sense	Dip Switch 1 ON will short D & 4
3	4	+ Bridge Output	
4	E & 5	Key	
5	F & 6	--	
6	H	Calibration Switch	Dip Switch 2 ON will short H & 7
7	7	Calibration Resistor	
8	J & 8	6.8 VDC Reference	
9	K	Output Offset	Dip Switch 3 ON will short K & 9
10	B & 2 = Common	Common (Ground)	
11	B & 2 = Common	Common (Ground)	
12	9	- Remote Sense	Dip Switch 3 ON will short K & 9
13	L & 10	- INPUT	
14	M & 11	+ INPUT	
15	N & 12	Filtered Output	
16	P & 13	Amplified Output	
17	R	½ Bridge Completion	Dip Switch 4 ON will short R & 4
18	14	Bridge Balance	
19	S	¼ Bridge Completion	Dip Switch 5 ON will short S & 15
20	15	¼ Bridge Completion	

Pin N (Terminal Block Pin 15) is the standard output for most strain gage and instrumentation applications.

General Calibration Procedure:

1. Connect "+ Sense" (Terminal Block Pin 2) to "Bridge Supply" (TB Pin 3). Connect each of the following to "Common" (TB Pin 10 or 11): Output Offset (TB Pin 9), "- Sense" (TB Pin 12), "- Input" (TB Pin 13), "+ Input" (TB Pin 14).

2. Measuring between "Filtered Output" (TB Pin 15) and "Common" (TB Pin 10 or 11), set input offset (RP3) for 0 V.
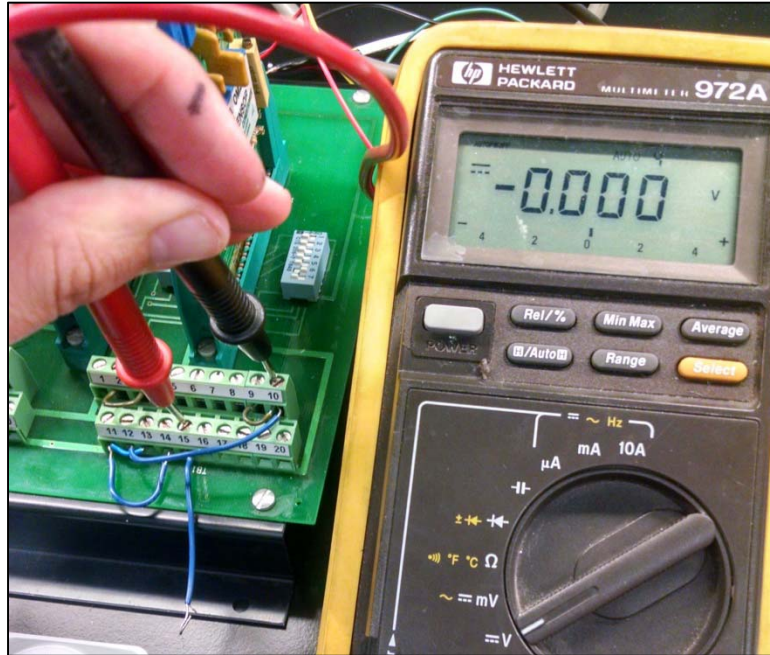
3. Measuring between "B+ output" (TB Pin 3) and common (TB Pin 10 or 11), adjust the bridge output trimpot (RP2) to the desired excitation voltage (4-10 VDC) with OM2-161 Dip Switch 1 off. Alternatively, set OM2-161 Dip Switch 1 on for an excitation voltage of ~10.2 V.

94
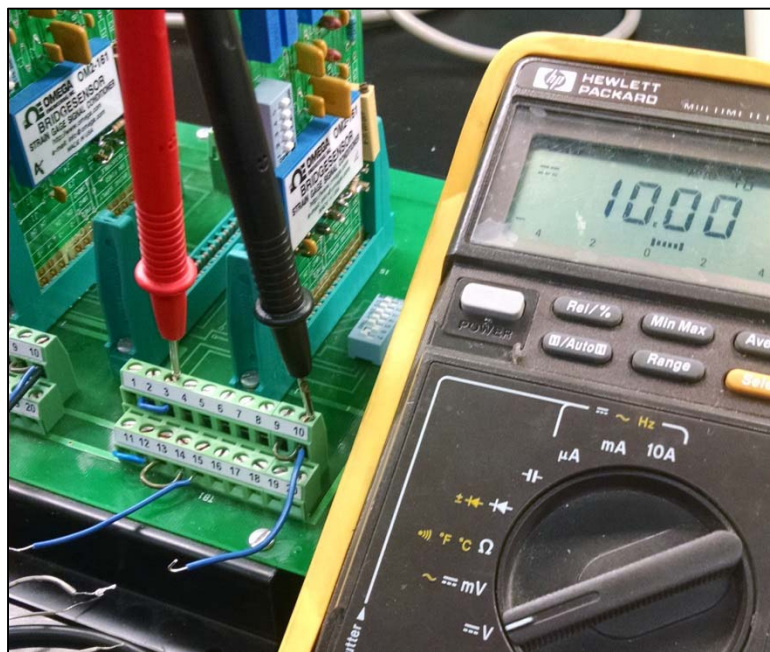
4. Remove jumpers from step 2 and connect the bridge.
5. With the bridge in zero condition, adjust output (TB Pin 15 or 16) for 0V using the bridge balance trimpot (RP6) or output offset trimpot (RP1). Connecting "Output Offset" (TB Pin 9) to "Common" (TB Pin 10 or 11) disables the output offset feature and RP1.
6. Apply a load to the bridge (or simulate the bridge with a millivolt source) and adjust the output (TB Pin 15 or 16) to the desired value using coarse gain trimpot (RP5) and fine gain trimpot (RP4). *** If Resistor R6 has been removed from OM2-161, RP4 and RP5 are disabled, and gain is instead adjusted using the trimpot installed across RG.

*** Resistor R6 has been removed from this amplifier, disabling RP4 and RP5. Gain is instead adjusted using this trimpot, installed across RG.

Gain set to 100 for amplifier mounted on TP1. ~1 psi load applied to pressure transducer 26PC6CF6G via vertical tube of water. (10/2014)

Gain set to 200 for amplifier mounted on TP2. ~1 psi load applied to pressure transducer 26PC6BF2G via vertical tube of water. (10/2014)

Active Filter Settings:

The amplifier output is connected to a 2 pole, inverting gain (-2V/V) active filter, which has an adjustable cutoff frequency of 10, 100 and 1kHz.   The cutoff frequency is adjusted via the dip switches on OM2-161:

Cutoff Frequency	SW2	SW3	SW4	SW5
10 Hz	ON	ON		
100 Hz			ON	ON
1000 Hz or User Select	All Off			

The output offset may be adjusted with the output offset trimpot (RP1). If the output offset feature is not desired, connect "External Output Offset" (Terminal Block Pin 9) to Common (Terminal Block Pin 10 or 11) directly at the mounting kit.

Remote Sensing:

Remote sensing of excitation voltage prevents leadwire resistance changes as a result of distance or temperature from affecting the transducer span. The remote sense wires are connected between the excitation terminals on the transducer (26PC Pins 1 and 3) and the remote sense terminals on the amplifier (Terminal Block Pins 2 and 12). The remote sensing circuit continuously monitors the excitation voltage at the transducer, and will compensate for any line drops that might be present. If remote sensing is not required, connect "+ Sense" (Terminal Block Pin 2) to "+ Bridge Output" (Terminal Block Pin 3) and connect "- Sense" (Terminal Block Pin 12) to Common (Terminal Block Pin 10 or 11).

Connection Diagram for use of 26PC Pressure Transducers: